ELSEVIER

Physics Reports 257 (1995) 1–83

PHYSICS REPORTS

# Hyperspherical coordinate approach to atomic and other Coulombic three-body systems

C.D. Lin

*Department of Physics, Kansas State University, Manhattan, KS 66506, USA*

Received October 1994; editor: J. Eichler

**Contents:**




*SSDI* 0370-1573(94)00094-8

**Abstract**

Developments in the application of hyperspherical coordinates in a unified treatment of bound states and resonances of two-electron atomic systems and other general Coulomb three-body systems are reviewed. It is shown that the nature of the internal normal modes of such three-body systems can be examined within the adiabatic approximation where the hyperradius is treated as an adiabatic parameter. From the nodal lines in the internal coordinates, it is shown how a set of new quantum numbers can be assigned. The most recent progress in the application of hyperspherical close coupling method to the photoabsorption of two-electron atoms and to rearrangement collisions is also addressed.

## 1. Introduction

The basic idea of the hyperspherical approach to three-body systems is very simple. The two relative coordinates are rewritten into a single six-dimensional vector and the nonrelativistic Schrödinger equation in the six-dimensional space is to be solved without reference to the "wave function" associated with individual particles. The condition of particle exchange symmetry becomes the boundary conditions of the wave function on the hypersurface.

The hyperspherical approach has been applied to solve bound states and scattering problems in many different fields of physics and chemistry. Many of the earlier works dealt with the basic structure of the mathematical functions encountered in hyperspherical coordinates. For example, a monograph by Avery [1] treats in great depth the properties of hyperspherical harmonics. In recent years, computational techniques have been developed to perform accurate calculations in hyperspherical coordinates, and the hyperspherical approach provides a direct and conceptually elegant method for treating problems in few-body systems. In particular, the hyperspherical method has been very successfully used in treating reactive scattering in atom-diatom collisions and in problems in atomic physics.

This review focuses mostly on the progress made in the use of hyperspherical coordinates to problems in atomic physics, particularly the atomic three-body systems. In fact, one of the most important features of the hyperspherical approach is that it can be applied to any three-body systems, irrespective of the masses of the particles. Thus, methods developed for treating the helium atom can be generalized directly to treating problems in $H_2^+$ or the scattering of a positron by a hydrogen atom.

The earlier development of the hyperspherical approach to two-electron atoms has been reviewed by a number of authors [2–4]. These earlier reviews dealt only with the conceptual and qualitative results. In the last few years, great strides have been made, particularly in the application of the hyperspherical approach to obtain accurate quantitative results. In addition, the hyperspherical approach has been extended to apply to general three-body systems where the masses of the particles are not restricted. This article reports progress made since the review by Fano in 1983 [2].

### *1.1. Hyperspherical approach to three-body problems*

#### *1.1.1. Atomic physics*

Hyperspherical coordinates were first introduced into atomic physics by Gronwall in 1937 [5] to study the analytic structure of the Schrödinger equation for the ground state of helium atom. It was found by Barlett [6] and later independently by Fock [7], that the ground state wave function of helium does not exist in the form of the Hylleraas type [8]

$$\Psi(r_1, r_2, r_{12}) = \sum_{lmn} A_{lmn}\, r_1^l r_2^m r_{12}^n, \tag{1.1}$$

where $r_1$ and $r_2$ are the distances of the two electrons from the nucleus, and $r_{12}$ is the distance between the two electrons; instead, it exists only in the "Fock expansion" type,

$$\Psi(r_1, r_2, r_{12}) = \sum_k C_k(r_1, r_2, r_{12})(\ln R)^k, \tag{1.2}$$

where $R = (r_1^2 + r_2^2)^{1/2}$ is the hyperradius originally introduced by Gronwall and $C_k$ is a polynomial. The Hylleraas-type wave function accounts for the singularity of two electrons coming close to each other, but only the Fock expansion accounts for the singularity when *both* electrons are close to the nucleus. It has been found that variational calculations of the ground state energy of helium using the Fock expansion (1.2) converge much faster than the Hylleraas expansion (1.1). For example, a 101-term Fock expansion can give a better ground-state energy of helium than a 1078-term standard [i.e., $l$, $m$ and $n$ in (1.1) are restricted to integers] Hylleraas-type expansion [9]. Of course, calculations based on Fock expansion are much more complicated.

Hyperspherical coordinates have also been employed in the direct numerical solution of the Schrödinger equation for two-electron systems since the 70's. Because the hyperspherical harmonics [see (2.1.1)] form a complete set, it is possible to expand the wave function in the form

$$\Psi(R, \Omega) = \sum_{[k]} F_{[k]}(R)\, u_{[k]}(\Omega) \tag{1.3}$$

where $[k]$ denotes the set of quantum numbers that are to label the hyperspherical harmonics and $\Omega$ denotes collectively the five angles. Substituting (1.3) into the two-electron Schrödinger equation results in a set of coupled differential equations for $F_{[k]}(R)$. Attempts were made in the 70's to solve the resulting coupled equations, but the convergence of the expansion was found to be extremely slow [10,11]. This is not surprising since hyperspherical harmonics are not suitable for describing the limit where one electron is far away from the other.

The resurgence of using hyperspherical coordinates in atomic physics in the last two decades owes much to its applications to the study of doubly excited states of helium and $H^-$. It was introduced by Fano and first applied by Macek [12] where the wave function is expanded as

$$\Psi(R, \Omega) = \sum_{\mu} F_\mu(R)\, \Phi_\mu(R; \Omega). \tag{1.4}$$

Eq. (1.4) takes the form of the Born–Oppenheimer expansion where the adiabatic wave functions $\Phi_\mu(R; \Omega)$ are obtained by solving the Schrödinger equation at a fixed value of $R$,

$$H|_{R=\text{const}}\, \Phi_\mu(R; \Omega) = U_\mu(R)\Phi_\mu(R; \Omega). \tag{1.5}$$

The basic idea of the adiabatic expansion (1.4) is that $\Phi_\mu(R; \Omega)$ varies smoothly with $R$ except in localized regions of avoided crossings and the "channel index" $\mu$ serves to identify a new set of approximate quantum numbers in designating doubly excited states. The new understanding of doubly excited states of two-electron atoms and ions obtained using the hyperspherical approach is based on this approximation, and they will be discussed fully in Section 4.

### *1.1.2. Molecular physics*

Hyperspherical coordinates were first adopted in molecular collisions by Smith [13]. Kuppermann [14] published his strategy of implementing hyperspherical coordinates for exact quantum evaluations of chemical reactions in 1975. At present, there are several groups developing computer packages for calculating state-selective reactive scattering cross sections [15–20] using hyperspherical approach. For example, the collisions $H+H_2$ $(v = 0, j = 0) \rightarrow H_2$ $(v', \text{odd } j')$ + H in the energy range $E_{\text{tot}}$ of a few eV's have been calculated using hyperspherical methods [21] and compared to those obtained using methods based on the Kohn variational principle [22]. It has been established that these

different theoretical approaches reach essentially identical results, and discrepancies have been found with the existing experiment[23]. It is further established that the hyperspherical approach in general takes less computing time, and calculations including a few hundred channels have been carried out for collisions between $F+H_2$ where data from molecular beam experiments are available [24]for comparison. Reactive scattering has been studied using the hyperspherical methods for the following systems: $H+H_2$ [21], $F+H_2$ [16], $Cl+H_2$ [25] and $He+H_2^+$ [26,27]. This subject has been reviewed recently by Launay [28]and a more restricted application of the hyperspherical approach has also been reviewed by Ohsaki and Nakamura [29]. At present, the practitioners in chemical physics probably have the most sophisticated applications of hyperspherical coordinates in scattering calculations. In these applications, the potential surface among the three atoms has to be determined either from ab initio calculations or by semi-empirical fitting. Because of the small level spacings among the rotational and vibrational excited states, the number of channels included in the calculation is usually quite large even for the "small" collision energy of the order of 1 eV. In these collisions, it is also essential to include many partial waves to achieve converged results. Because of these complications in chemical reactive scattering, the power and the underlying simplicity of the hyperspherical methods is often overlooked.

The hyperspherical approach has also been applied to study the vibrational energy levels of triatomic molecules, such as in $H_2O$, in $CO_2$ [30], in trimers such as $Ar_3$ [31] and in the photodissociation of triatomic molecules [32,33].

### *1.1.3. Nuclear physics*

The application of hyperspherical formalism to nuclear three-body problems has a rich history. Delves [34] introduced the hyperspherical harmonics expansion to describe three-body channels in nuclear reactions. Danville [35] solved the trinucleon bound states using hyperspherical harmonics. Three-body hypernucleon problems such as ${}^{3}_{\Lambda}H$, ${}^{6}_{\Lambda,\Lambda}He$, ${}^{9}_{\Lambda}Be$ have been studied since the early work of Dalitz and Rajasekaran [36]. A number of less stable nuclei have been treated as three-body systems. For example, $^{10}He$ has been treated as $n+n+{}^{8}He$ [37], and $^{6}He$ is treated as a three-body system with a $^{4}He$ core. For the bound states of $^{6}He$ and $^{11}Li$, a recent review is given by Zhukov et al. [38].

Most of the nuclear three-body problems have been examined so far using hyperspherical harmonics. The convergence of such an expansion, as has been found in atomic and molecular physics, is known to be extremely slow. Convergence can be improved by selecting optimal subsets, and such methods have been applied to three-nucleon systems. The application of the hyperspherical methods to nuclear physics can be found in Ballot and Fabre de le Ripelle [39]. For other examples of recent studies of nuclear three-body problems, see references [40,41]. We mention that in most of nuclear three-body systems, the spin-orbit and spin-spin interactions are more important and in general should be included in the Hamiltonian.

### *1.1.4. Elementary particle physics*

The nonrelativistic aspect of the three-body problem for baryons has been reviewed recently [42]. The early picture of the baryon spectrum was based on the unitary symmetry from which the $\Omega^-$ particle was predicted. The excitation patterns of the baryons, on the other hand, were described in terms of the harmonic oscillator model. In recent years, one of the major experimental activities

concerns baryons with heavy flavors, including Qqq, Qqs or Qss, where q stands for a u or d quark, s for an s quark and Q for heavy quarks such as c or b. These states have a helium-like structure. In the future, baryons such as QQq can be studied as well. In the nonrelativistic model of baryons, the two-body short-range potential is derived from the QCD and the challenge is to solve the resulting three-body problem.

The baryon spectrum so far has been investigated mostly based on the harmonic-oscillator model. Improved methods that involve treating the anharmonicity by using first order perturbation theory or by using harmonic oscillator basis functions for the expansion of wave functions have been used as well. These approaches, similar to those used in atomic and molecular physics, do not easily provide a classification of the baryon spectrum. The hyperspherical expansion has been discussed, but few calculations have actually been carried out. Hyperspherical approach as a general method for treating three-body problems for baryons has just begun. Attempts have been made to describe the hadron mass spectrum using a nonrelativistic quark model [43] to obtain the masses of nonstrange hadrons belonging to the meson octet and the baryon decuplet, and relativistic corrections have also been discussed [44]. Despite its simplicity, an attempt has even been made to derive the quark-quark potentials from the inversion of the baryon spectra [45].

### *1.2. Coulombic three-body systems with two identical particles*

This section provides an overview of the spectroscopy of bound states formed by three charged particles. We first consider ABA systems where two of the charged particles are identical. Each charged particle carries one unit of charge and the masses are $m_A$ and $m_B$ for particle A and particle B respectively. This class of ABA systems ranges from $H^-$, to $e^-\mu^+e^-$, $Ps^-(=e^-e^+e^-)$, $d^+\mu^-d^+$ and $H_2^+$. Except for an overall scaling, these systems are distinguished by the parameter $\lambda = m_A/m_B$, which is defined to be the mass of each of the identical particles with respect to the mass of the third particle. Thus $\lambda$ ranges from about $10^{-3}$ in $H^-$ to 1 in $Ps^-$ to about $10^3$ for $H_2^+$.

#### *1.2.1. Two-body Coulomb problems*

The nonrelativistic two-body Coulomb problem is well studied in elementary quantum mechanics. The energy levels for the system AB is given by the Bohr formula. Using atomic units, the binding energy for an excited state with principal quantum number $N$ is given by

$$E_N = -\mu/(2N^2) \tag{1.6}$$

where $\mu = m_A m_B/(m_A + m_B)$ is the reduced mass, and the eigenfunctions are given by the well-known hydrogenic wave functions. The two-body energies (1.6) are the asymptotic energies of the ABA system when it dissociates into $A + (AB)_N$ where the subscript $N$ indicates that (AB) is in the excited state.

#### *1.2.2. Atomic models versus molecular models*

In standard textbooks, adding another charged particle A to the well-known AB system is treated theoretically in very different ways depending on whether A is much heavier or much lighter than B. If $m_A \ll m_B$, as in the case of $H^-$ or He, the basic physical picture is that the electron is moving very fast around the nucleus and thus each electron can be treated more or less independently. This is the basic picture behind the shell model of atoms where each electron is moving in its "own"

Table 1.1
Scaling of the ground-state binding energy $E_s$ of Coulomb three-body systems AAB with respect to the reduced mass $\mu$ of particles A and B. The last column gives the ratio of $E_s/\mu$ of each system normalized to that for $H^-$. The column is ordered according to increasing values of $\lambda = m_A/m_B$.

| System | $E_s$ (a.u.) | $\mu$ | $\lambda$ | Norm |
|---|---|---|---|---|
| $H_\infty^-$ | 0.52775 | 1.0 | $5.446\times10^{-4}$ | 1.000 |
| e$\mu$e | 0.525054 | 0.9952 | 0.0048 | 0.9997 |
| $\pi\pi$K | 111.3879 | 212.932 | 0.2827 | 0.9912 |
| e(3e)e | 0.39214 | 0.75 | 0.3333 | 0.9907 |
| e(2e)e | 0.34837 | 0.6667 | 0.5 | 0.9902 |
| pKK | 330.8119 | 633.051 | 0.5262 | 0.9902 |
| eee | 0.262005 | 0.5 | 1.0 | 0.9929 |
| ppK | 334.5864 | 633.051 | 1.9004 | 1.0015 |
| $\pi$KK | 114.10743 | 212.932 | 3.5373 | 1.0154 |
| pp$\pi$ | 129.71588 | 237.760 | 6.7227 | 1.0338 |
| pp$\mu$ | 102.22985 | 185.78 | 8.8887 | 1.0427 |
| dd$\mu$ | 109.8237 | 195.68 | 17.762 | 1.0635 |
| tt$\mu$ | 112.9799 | 199.21 | 26.596 | 1.0746 |
| $H_2^+$ | 0.59201 | 1.0 | 1836.2 | 1.1218 |

central potential. On the other hand, if $m_A \gg m_B$, as in $H_2^+$, the motion of the electron is much faster and the two protons perform slower vibrations and rotations. This physical model is expressed in mathematical form as the Born–Oppenheimer approximation where the electronic motion is calculated by treating the two nuclei to be at rest, similar to Eq. (1.5), and the two nuclei perform rotations and vibrations in the effective potential field of the fast electron.

These two distinct models are based on the "obvious" physical picture, and their popularity and success in everyday usage demonstrate their soundness as far as providing descriptions of most of the observable properties of each system. However, the sharp contrast between the two models presents an unnecessary conceptual division which prevents us from taking a unifying viewpoint of the Coulombic ABA systems. In the next two subsections we provide evidence to illustrate why the traditional division of atomic and molecular systems is unnecessary.

### *1.2.3. Ground-state energies of ABA systems*

All Coulombic three-body systems ABA consisting of two identical particles have at least one stable bound state against dissociation [46]. Using Hylleraas-type basis functions, Frolov [47] has calculated the total binding energies of a number of Coulombic ABA systems. It was demonstrated by Chen and Lin [48] that the total binding energy of an ABA system nearly scales linearly with the reduced mass $\mu = m_A m_B/(m_A + m_B)$. This is illustrated in Table 1.1 where the calculated total binding energies of a number of ABA systems are tabulated in accordance with increasing values of $\lambda = m_A/m_B$. Thus, for $\lambda \to 0$ we have the typical "atomic" limit consisting of two light identical particles and a heavy one, to $\lambda \to \infty$, which is the molecular limit consisting of two identical heavy particles and a light one. By normalizing the energy for $\lambda = 0$ to unity, in Table 1.1 we notice that the scaled binding energies for the ABA systems deviate no more than a few percent from unity except for large $\lambda$. Even for $H_2^+$, where $\lambda = 1836$, the deviation is only about 12%. This small range of the

scaled energies is most surprising in view of the drastic difference in our physical models of atoms such as $H^-$ and molecules such as $H_2^+$.

To understand the simple scaling, let $\boldsymbol{r}_1$ and $\boldsymbol{r}_2$ be the two vectors from B to each of the particles A. The Hamiltonian can be expressed as[48]

$$H = \mu\left(-\frac{1}{2}\nabla_1^2 - \frac{1}{2}\nabla_2^2 - \frac{1}{r_1} - \frac{1}{r_2} + \frac{1}{r_{12}}\right) - \frac{\mu^2}{m_B}\nabla_1 \cdot \nabla_2 = \mu\left[H_\infty + (\mu/m_B)\boldsymbol{p}_1 \cdot \boldsymbol{p}_2\right] \tag{1.7}$$

where the last term on the right is the mass polarization term due to the motion of the two identical particles with respect to the center of mass of the ABA system. In (1.7), $H_\infty$ is the Hamiltonian when $m_B$ is set to infinity. This equation shows that if the mass polarization term is small, then the binding energy of the ABA system will scale with the reduced mass of the two-body system AB and the last column of Table 1.1 would all be equal to 1.00.

The mass polarization is a measure of the momentum correlation of the two identical particles with respect to the third particle. If this correlation is small, then the energy of an ABA system will scale with $\mu$. If $m_A \gg m_B$, as in the case of molecules such as $H_2^+$ and $d^+\mu^- d^+$, the light particle B tends to stay in the middle of the two heavy particles to achieve bonding. This configuration implies a negative $\langle \boldsymbol{p}_1 \cdot \boldsymbol{p}_2 \rangle$, and thus a more tightly bound state. For $m_A \ll m_B$, each light particle A is less localized and thus the momentum correlation (or mass polarization) is smaller. Thus the normalized binding energy is closer to $-1.0$, as seen in Table 1.1 for the case of small $\lambda$.

### *1.2.4. Rovibrational spectrum of doubly excited states of atoms*

Theoretical studies of doubly excited states of atoms such as helium and $H^-$ over the last two decades have established that their energy levels exhibit patterns similar to the rovibrations of a molecule [49–51,4]. In Fig. 1.1 we display the calculated energies of doubly excited states of $H^-$ that lie below the $N = 5$ excited states of H. These energies were obtained by Ho and Callaway [52] using Hylleraas type variational functions and the results are ordered in terms of $K$ and $T$ quantum numbers. It is not essential for the present purpose to know the precise definition of $K$ and $T$ except to note that $K$ is related to some vibrational quantum number $v$, and $T$ is the projection of the total orbital angular momentum along the interelectronic axis. Along each column, the $K$ and $T$ quantum numbers are fixed and the energies are ordered with increasing total orbital angular momentum $L$. Obviously along each column the level orderings are similar to the rotational levels of a molecule. Along the horizontal axis, the states have different vibrational quantum numbers. If $T \neq 0$, we note the near degeneracy of a pair of states for each $L$, similar to the $\Lambda$-doubling of a molecule. The energy level patterns shown in Fig. 1.1 are very different from those expected from the shell model of atoms, but very close to the rovibrational multiplet structure of a linear triatomic molecule [53,50].

### *1.2.5. The need of a unified approach*

The brief summary of known results about Coulombic ABA systems in the last two subsections clearly indicates that the traditional division of atomic systems vs molecular systems is rather arbitrary. While the shell model attributes each electron to a certain orbital, the electron-electron interaction and the Pauli exclusion principle as exhibited by the symmetry of the total wave function tend to smear out this distinction. This is particularly acute for doubly excited states where the concept of orbitals for individual electrons is no longer meaningful, and the rovibrational energy level patterns

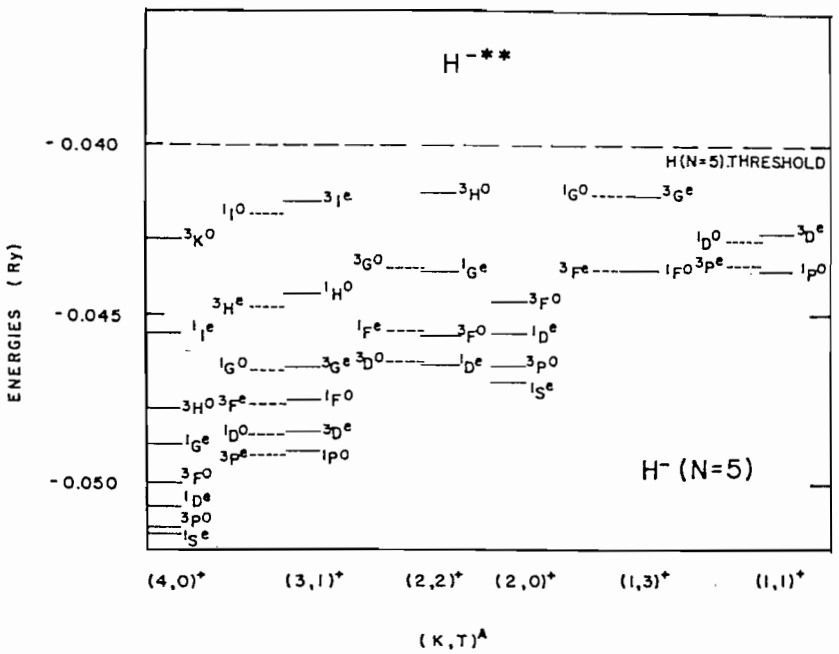


Fig. 1.1. Energy levels of $H^-$ resonances lying below the $H(N = 5)$ threshold grouped according to the $(K,T)^A$ quantum numbers. Note that along each column the energy levels resemble a rotor series.

as displayed in Fig. 1.1 clearly show the need of a picture where the motion of the two electrons be treated together.

For molecules such as $H_2^+$, the conventional Born–Oppenheimer approximation is known to have many undesirable features, especially that it does not describe the dissociation limit correctly. In view of the many common features of the Coulombic three-body systems, it is desirable to develop a theoretical scheme which is applicable to any three-body systems to cover the "atomic" regime where $\lambda \to 0$ and the "molecular" regime where $\lambda \to \infty$, as well as the region in between for systems such as $e^-e^+e^-$. In Section 2.2, we will show that generalized hyperspherical coordinates are suitable for describing these problems.

### *1.3. Coulombic three-body systems of three distinguishable particles*

#### *1.3.1. Existence of bound states*

When all of the three particles are different, it is known that only certain combinations of masses in the $A^+B^+C^-$ systems can have stable bound states [54]. To describe such systems, it is always possible to set the mass of one of the three particles to be unity, leaving two relative mass parameters to map the possible combinations. From the known results that $HD^+$ (or $d^+p^+e^-$) is stable but $p^+e^+e^-$ is not, it was speculated that $m_A \cong m_B$ may be the condition for the existence of bound states. However, this rule does not apply to the well-known stable systems such as $HD^+$ and $HT^+$ where the condition $m_A \cong m_B$ is not satisfied. It was found recently by Martin et al. [55] that a better representation of the "region of stability" is to use the parameters $\alpha_i$'s where

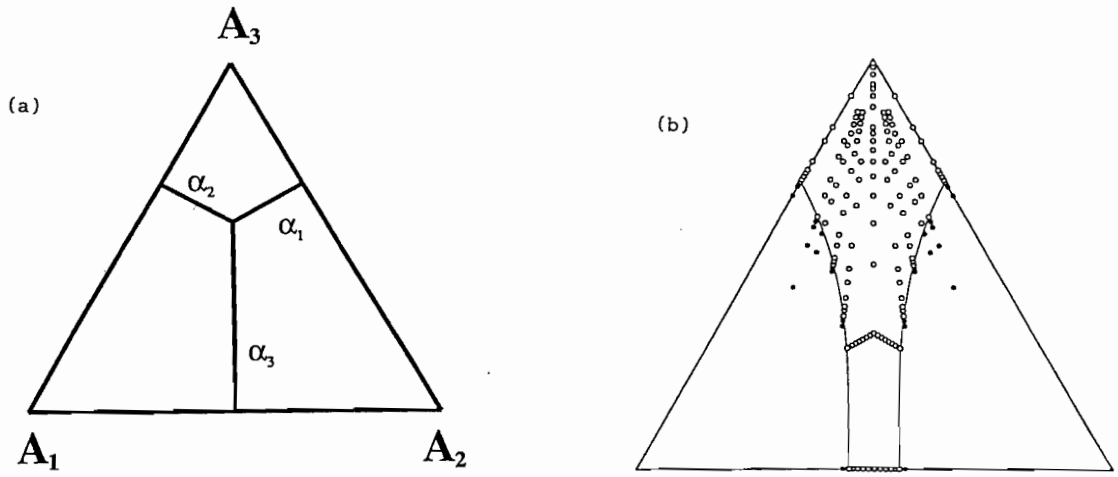


Fig. 1.2. "Island of stability" for the existence of stable ground state for general Coulomb three-body systems. Each system is represented by a point inside the triangle where $\alpha_1 + \alpha_2 + \alpha_3 = 1$, with $\alpha_i$ defined by Eq.(1.8), see (a). In (b), the circles represent systems where calculations have shown the existence of bound states, and the solid circles represent calculations showing no bound states. The solid line represents an interpolation which separates regions of no bound states from the inner region where bound states exist (courtesy of Brett Esry, data from Frolov [47]).

$$\alpha_i = \frac{1/m_i}{1/m_1 + 1/m_2 + 1/m_3}. \tag{1.8}$$

Obviously, $\alpha_1 + \alpha_2 + \alpha_3 = 1$. The three parameters $\alpha_1$, $\alpha_2$ and $\alpha_3$ can be represented as a point in an equilateral triangle of length $2/\sqrt{3}$ if the $\alpha_i$ is measured from the point to each of the three sides of the triangle, as shown in Fig. 1.2a.

In this representation, all the mass combinations of the three particles fall within this triangle. Since a symmetric $A^+A^+B^-$ system always contains at least one stable bound state [46], and these systems lie along the diagonal line originating from point $A_3$, the region of stability is estimated to be confined near this line, with the condition that $|\alpha_1 - \alpha_2|$ be small. The width of $|\alpha_1 - \alpha_2|$ would depend on $\alpha_3$. For large $\alpha_3$, the three-body system is closer to a "molecular" system, and we expect that the width to be broader. For smaller $\alpha_3$, the system is closer to the "atomic" system such as $H^-$ where the width is expected to be smaller.

The binding energies of the ground state of $A^+B^+C^-$ systems have been calculated by Frolov and coworkers [56,57,47] for a large number of systems using variational methods where the trial functions are taken to be of the form

$$\Psi = \sum_{k=1}^{M} C_k \exp(-\alpha_k r_{12} - \beta_k r_{23} - \gamma_k r_{31}) \tag{1.9}$$

where $r_{ij}$ is the distance between the two particles $i$ and $j$, and the nonlinear parameters are chosen by some pseudorandom algorithm. The number of terms in (1.9) is of the order of a few hundreds and the well converged energies have been obtained for many systems. If we plot their results in the triangle of Fig. 1.2a, we obtain results shown in Fig. 1.2b where the stable states are indicated by open circles and states which are not bound are shown as solid circles. The boundary of stability is

indicated approximately by the two solid lines. The total angular momentum for each of the states considered is $L = J = 0$.

*1.3.2. Reactive and rearrangement collisions*

Our interest in Coulombic three-body systems is not limited to the search for bound states only. In fact, most of the interesting problems are related to scattering. For example, typical collisions are the excitation processes

$$A^+ + (B^+C^-)_i \rightarrow A^+ + (B^+C^-)_f \tag{1.10}$$

or the rearrangement processes

$$A^+ + (B^+C^-)_i \rightarrow (A^+C^-)_f + B^+ \tag{1.11}$$

where the two-body systems ($A^+C^-$) or ($B^+C^-$) can be in any excited state. Experimentally, the most interesting elementary rearrangement collisions include positronium formation in $e^+ + H \rightarrow (e^+e^-) + H^+$ or muon transfer in $t^+ + (d^+\mu^-) \rightarrow (t^+\mu^-) + d^+$ reactions. These are, of course, special examples of reactive scattering similar to those treated by quantum chemists, except that the interaction potentials in the present systems are well known. Note that the cross sections for these reactions at low energies are often influenced by the existence of resonances of the compound system $A^+B^+C^-$. Both subjects will be further discussed in Section 6.

## 2. The hyperspherical coordinate approach

In this section we discuss the different forms of the Schrödinger equation for three-body Coulombic systems in hyperspherical coordinates. We started with the simpler two-electron atomic systems, then the general three-body systems where the masses of the particles are arbitrary. In Section 2.3 we discuss the Schrödinger equation expressed in the body frame of reference, and a brief discussion of the generalization to many-electron systems is given in Section 2.4.

*2.1. Hyperspherical coordinates for two-electron atomic systems*

We first introduce hyperspherical coordinates for two-electron atomic systems such as helium and $H^-$ where the mass of the nucleus is treated as infinite. There are many ways to define hyperspherical coordinates. The essential requirement is that there is only one hyperradius which measures the size of the system and the rest are angles. For two-electron atoms, starting with $\boldsymbol{r}_1$ and $\boldsymbol{r}_2$, the positions of the two electrons measured from the nucleus, the simplest hyperspherical coordinates are obtained by replacing $r_1$ and $r_2$ by

$$R = (r_1^2 + r_2^2)^{1/2}, \qquad \alpha = \tan^{-1}(r_2/r_1) \tag{2.1}$$

where $R$ is the hyperradius and $\alpha$ is the hyperangle. Thus the two vectors $\boldsymbol{r}_1$ and $\boldsymbol{r}_2$ are replaced by six coordinates $(R, \Omega)$, where $\Omega = (\alpha, \theta_1, \phi_1, \theta_2, \phi_2)$ denotes collectively the five angles, with $\theta_i, \phi_i$ being the spherical angles of electron $i$. In this particular set of hyperspherical coordinates, the angles are defined with respect to a laboratory fixed frame. There are other choices of angles

in hyperspherical coordinates, but we will not discuss them here since they have not been used extensively in actual applications. Furthermore, the present choice of hyperangles can be easily generalized to many-particle systems, as discussed in Section 2.4.

*2.1.1. Kinetic energy operator and hyperspherical harmonics*

The goal of hyperspherical approach to two-electron problems is to solve the two-electron Schrödinger equation

$$\left(-\frac{1}{2}\nabla_1^2-\frac{1}{2}\nabla_2^2-\frac{Z}{r_1}-\frac{Z}{r_2}+\frac{1}{r_{12}}-E\right)\underline{\Psi}(\boldsymbol{r}_1,\boldsymbol{r}_2)=0 \tag{2.2}$$

in hyperspherical coordinates approximately.

Atomic units are used throughout this review unless otherwise noted. In hyperspherical coordinates, the volume element is $d\boldsymbol{r}_1\,d\boldsymbol{r}_2=R^5(\sin\alpha\,\cos\alpha)^2 dR\,d\hat{r}_1\,d\hat{r}_2$. One can eliminate the first-order derivatives in the differential operators by expressing

$$\underline{\Psi}(\boldsymbol{r}_1,\boldsymbol{r}_2)=\Psi(R,\Omega)/(R^{5/2}\sin\alpha\cos\alpha) \tag{2.3}$$

where $\Psi(R,\Omega)$ satisfies

$$\left(-\frac{d^2}{dR^2}+\frac{\Lambda^2}{R^2}+\frac{2C}{R}+2E\right)\Psi(R,\Omega)=0 \tag{2.4}$$

and

$$\Lambda^2=\left(-\frac{d^2}{d\alpha^2}+\frac{\boldsymbol{l}_1^2}{\cos^2\alpha}+\frac{\boldsymbol{l}_2^2}{\sin^2\alpha}\right)-\frac{1}{4} \tag{2.5}$$

is the grand angular momentum operator where $\boldsymbol{l}_i$ is the angular momentum operator for electron $i$ and $C/R$ is the total Coulomb interaction potential among the three charged particles, with $C$ given by

$$C(\alpha,\theta_{12})=-\frac{Z}{\cos\alpha}-\frac{Z}{\sin\alpha}+\frac{1}{\sqrt{1-\sin 2\alpha\cos\theta_{12}}}. \tag{2.6}$$

In (2.4), $E$ is the total energy of the system given in atomic units, $Z$ in (2.6) is the charge of the nucleus, and $\theta_{12}$ is the angle between the two electrons with respect to the nucleus.

The first term in (2.4) is the kinetic energy operator associated with the hyperradial motion, and the second term $\Lambda^2/R^2$ is the grand "centrifugal" potential energy operator, including the well-known single particle centrifugal energy from each electron, and a term proportional to $-(R^{-2}d^2/d\alpha^2)$, which is a measure of the "difficulty" of having two electrons close to the nucleus simultaneously. The eigenfunctions of the $\Lambda^2$ operator satisfy[58]

$$\left(-\frac{d^2}{d\alpha^2}+\frac{\boldsymbol{l}_1^2}{\cos^2\alpha}+\frac{\boldsymbol{l}_2^2}{\sin^2\alpha}-(\nu+2)^2\right)u_{[k]}(\Omega)=0 \tag{2.7}$$

where $[k]$ denotes the set of quantum numbers, $[k]=(l_1,l_2,m)$, with $m$ related to the polynomial functions in angle $\alpha$, and $\nu=l_1+l_2+2m$. The eigenfunctions are

$$u_{[k]}(\Omega)=f_{l_1l_2m}(\alpha)\,y_{l_1l_2LM}(\hat{r}_1,\hat{r}_2) \tag{2.8}$$

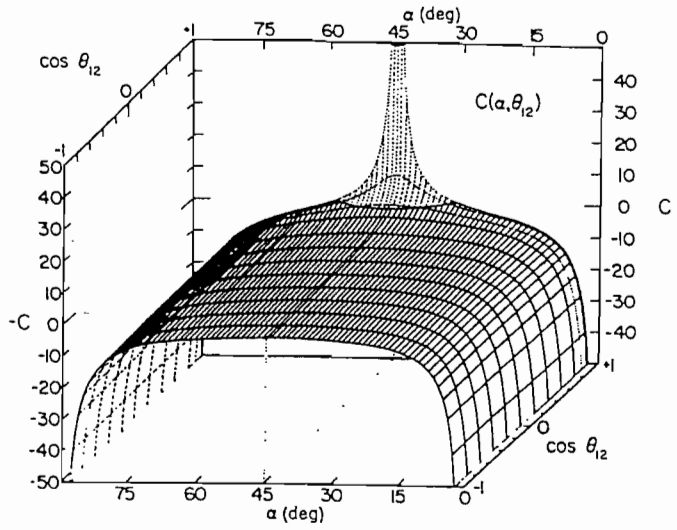


Fig. 2.1. Potential surface $C(\alpha, \theta_{12})$ in Rydberg units for a pair of electrons in the field of a proton. From Lin [80].

where the coupled angular momentum function is

$$y_{l_1 l_2 LM}(\hat{r}_1, \hat{r}_2) = \sum_{m_1 m_2} \langle l_1 m_1 l_2 m_2 | LM \rangle Y_{l_1 m_1}(\hat{r}_1) Y_{l_2 m_2}(\hat{r}_2) \tag{2.9}$$

with $Y_{lm}(\hat{r})$ being the usual spherical harmonics and $\langle l_1 m_1 l_2 m_2 | LM \rangle$ the Clebsch–Gordan coefficients. The $L$ and $M$ are the total orbital angular momentum and its projection along a laboratory fixed axis, respectively. The eigenfunctions in $\alpha$ have the explicit form

$$f_{l_1 l_2 m}(\alpha) = N_{l_1 l_2 m} (\cos\alpha)^{l_1+1} (\sin\alpha)^{l_2+1} F(-m, m + l_1 + l_2 + 2, l_2 + 3/2, \sin^2\alpha) \tag{2.10}$$

where $N$ is a normalization constant and $F$ is proportional to a Jacobi polynomial [58].

The total eigenfunctions $u_{[k]}(\Omega)$ are called hyperspherical harmonics. They are the harmonic functions on the hyperspherical surface of a six-dimensional space and are simultaneous eigenfunctions of $\Lambda^2$, $l_1^2$, $l_2^2$, $L^2$ and $L_z$. The set of hyperspherical harmonics satisfies the orthogonality condition

$$\int u_{[k']}(\Omega) u_{[k]}(\Omega) d\Omega = \delta_{[k][k']} \tag{2.11}$$

and forms a complete set.

### 2.1.2. *Potential surfaces*

The nonseparability of the Schrödinger equation (2.4) is due to the potential energy term. For the two-electron atomic systems, the potential energy scales with $1/R$, where the effective charge $C$ depends only on angles $\alpha$ and $\theta_{12}$. In Fig. 2.1, we show this potential surface on the $(\alpha, \theta_{12})$ plane for $Z = 1$. The major features of this potential surface are:

(i) The deep potential valleys near $\alpha \to 0$ and $\alpha \to \pi/2$, corresponding to the strong Coulomb attraction when either electron is very close to the nucleus.

(ii) The steep spike at $\alpha = \pi/4$ and $\theta_{12} = 0$, corresponding to the strong Coulomb repulsion when the two electrons are on top of each other.

(iii) The saddle point at $\alpha = \pi/4$ and $\theta_{12} = \pi$. At this point, the potential drops for $\alpha$ away from $\pi/4$, but it increases for $\theta_{12}$ away from $\pi$. This saddle point in the potential surface plays a major role in determining the quasi-stability of doubly excited states of atoms.

## 2.2. *Coulombic three-body systems of arbitrary masses*

### 2.2.1. *Jacobi coordinates and mass-weighted hyperspherical coordinates*

Consider a Coulombic three-body system. The Schrödinger equation in the laboratory frame can be written as

$$\left(-\frac{1}{2m_A}\nabla_A^2 - \frac{1}{2m_B}\nabla_B^2 - \frac{1}{2m_C}\nabla_C^2 + \frac{Z_A Z_B}{r_{AB}} + \frac{Z_A Z_C}{r_{AC}} + \frac{Z_B Z_C}{r_{BC}} - E\right)\underline{\psi} = 0 \tag{2.12}$$

where $m_i$ is the mass of particle $i$ which has charge $Z_i$, and $r_{ij}$ is the distance between particles $i$ and $j$. To maintain that the kinetic energy operator is diagonal, we introduce Jacobi coordinates to describe the relative motion. We can choose $\boldsymbol{\rho}_1 = \boldsymbol{r}_{AB}$, the vector from A to B, and $\boldsymbol{\rho}_2 = \boldsymbol{r}_{AB,C}$, the vector from the center of mass of A and B to particle C. In this coordinate system, the Schrödinger equation in the center-of-mass frame takes the form

$$\left(-\frac{1}{2\mu_1}\nabla_{\rho_1}^2 - \frac{1}{2\mu_2}\nabla_{\rho_2}^2 + \frac{Z_A Z_B}{r_{AB}} + \frac{Z_A Z_C}{r_{AC}} + \frac{Z_B Z_C}{r_{BC}} - E\right)\underline{\Psi}(\boldsymbol{\rho}_1, \boldsymbol{\rho}_2) = 0 \tag{2.13}$$

where $\mu_1 = \mu_{AB} = m_A m_B/(m_A + m_B)$ and $\mu_2 = \mu_{AB,C} = (m_A + m_B)m_C/(m_A + m_B + m_C)$ are the reduced masses of the pair A and B and of the pair AB and C, respectively.

For future reference, we designate the three-body systems as $A^+B^+C^-$ if all the three particles are different, and as $A^+B^-A^+$ if two of the three particles are identical. (Obviously, the charged conjugated system $A^-B^-C^+$ has exactly the same properties as the $A^+B^+C^-$ system within our model.) Thus the Jacobi coordinates introduced in the previous paragraph resemble those used for describing diatomic molecules where $\boldsymbol{\rho}_1$ is along the internuclear axis and $\boldsymbol{\rho}_2$ are the electronic coordinates with respect to the center of mass of the two nuclei. This particular set of Jacobi coordinates will be referred to as the $\alpha$-set and sometimes as the "molecular" frame. There are two other possible Jacobi coordinates: the $\beta$-set where $\boldsymbol{\rho}_1^{(\beta)}$ is the vector from B to C and $\boldsymbol{\rho}_2^{(\beta)}$ is from the center of mass of BC to A; and the $\gamma$-set where $\boldsymbol{\rho}_1^{(\gamma)}$ is the vector from C to A and $\boldsymbol{\rho}_2^{(\gamma)}$ is from the center of mass of CA to B. These vectors are depicted in Fig. 2.2. The $\beta$- and $\gamma$-set are similar to those used to describe atoms such as He or $H^-$. The two vectors in the different sets are related by simple geometric relations known as kinematic rotations [13]. For systems consisting of two identical particles, the $\beta$-set and the $\gamma$-set are equivalent and the wave function should be properly symmetrized. We will come back to this point in Section 3.3.2.

We also notice that the Schrödinger equation (2.13) can be written in terms of $\beta$-set or $\gamma$-set Jacobi coordinates as well, with the corresponding reduced masses $\mu_1$ and $\mu_2$. The superscripts in the coordinates and the reduced masses will not be specified unless such a distinction is needed in the discussion.

One can introduce mass-weighted hyperspherical coordinates by defining

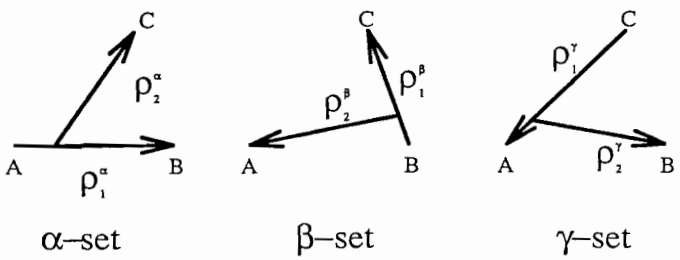


Fig. 2.2. Three sets of Jacobi coordinates for systems of three charged particles. The signs of charges for particles A and B are identical.

$$\xi_1 = \sqrt{\mu_1/\mu}\,\rho_1, \qquad \xi_2 = \sqrt{\mu_2/\mu}\,\rho_2 \tag{2.14}$$

where $\mu$ is arbitrary (taken to be unity in general). In terms of $\xi$'s, the Schrödinger equation (2.13) now takes the form

$$\left(-\frac{1}{2\mu}\nabla^2_{\xi_1} - \frac{1}{2\mu}\nabla^2_{\xi_2} + \frac{Z_A Z_B}{r_{AB}} + \frac{Z_A Z_C}{r_{AC}} + \frac{Z_B Z_C}{r_{BC}} - E\right)\underline{\Psi}(\boldsymbol{\xi}_1, \boldsymbol{\xi}_2) = 0 \tag{2.15}$$

such that the kinetic energy operators associated with the two "particles" are identical, and all the mass dependence of the three particles is cast in the rescaling of the distances.

From $\xi$'s, it is straightforward to introduce the hyperspherical coordinates as before,

$$R = \sqrt{\xi_1^2 + \xi_2^2}, \qquad \tan\phi = \xi_2/\xi_1 \tag{2.16}$$

where $\phi = \phi^{(i)}\,(i = \alpha, \beta, \gamma)$. We note that the hyperradius $R$ is independent of which set of Jacobi coordinates is used.

The mass-weighted hyperspherical coordinates have been applied to specific systems by a number of authors [59–63]. Many of the results obtained are qualitative or only semiquantitative in nature due to the limitation of numerical accuracy.

### 2.2.2. *The potential surfaces*

Using these mass-weighted hyperspherical coordinates, the Schrödinger equation has the form of (2.4), except that the effective charge $C$ is scaled with the masses of the system,

$$C(\phi, \theta) = \sqrt{\frac{\mu_1^\alpha}{\mu}}\frac{Z_A Z_B}{\cos\phi^\alpha} + \sqrt{\frac{\mu_1^\beta}{\mu}}\frac{Z_B Z_C}{\cos\phi^\beta} + \sqrt{\frac{\mu_1^\gamma}{\mu}}\frac{Z_C Z_A}{\cos\phi^\gamma}. \tag{2.17}$$

Thus, different three-body systems are characterized by their different potential surfaces. In (2.17), we express the potential surface explicitly in angles $\phi$ and $\theta$, where the latter is the angle between the two vectors $\boldsymbol{\rho}_1$ and $\boldsymbol{\rho}_2$. The potential surface for each system also depends on the specific Jacobi coordinates adopted. In Fig. 2.3 we show the potential surface of $H^-$ in $\alpha$-set and in $\beta$-set coordinates [64]. Note that the potential surface in the $\beta$-set is essentially identical to the one shown in Fig. 2.1. The potential surface in the $\alpha$-set coordinates is distinctly different. The two singularities due to the Coulomb attraction between each of the two electrons and the proton are now located at $(\phi, \theta) = (44.95°, 0)$ and $(44.95°, \pi)$ ($\phi = 45°$ if the mass of the proton is taken to be infinity),

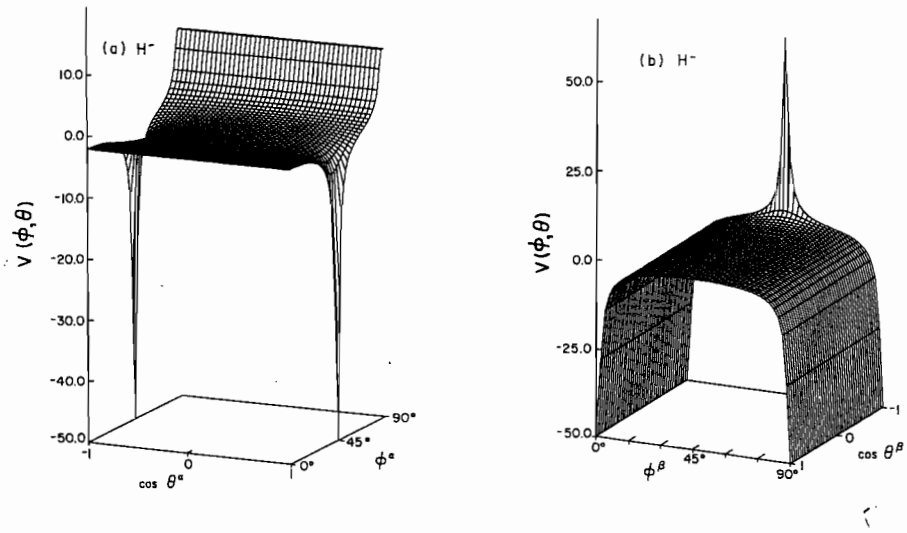


Fig. 2.3. The potential surface for $H^-$ ions at $R = 1$ plotted against hyperspherical angles in $\alpha$-set and in $\beta$-set coordinates. From Lin and Liu [64].

while the singular Coulomb repulsion between the two electrons is represented by a steep repulsive "wall" at $\theta = 90°$. Note that in the $\beta$-set the two attractive singularities become steep potential valleys, while the singular Coulomb repulsion becomes a sharp repulsive spike.

In order to understand the systematic trends of Coulomb three-body problems, we compare the potential surfaces of other systems which differ from $H^-$ only in the relative mass $\lambda$. In Fig. 2.4 we show the potential surfaces for $e^-e^+e^-$ and $d^+\mu^-d^+$ in the $\alpha$ and the $\beta$ set coordinates. Clearly, the potential surfaces in the $\beta$-set coordinates for the three systems are quite different, but the surfaces in the $\alpha$-set coordinates are much more similar. Recall that in the mass-weighted hyperspherical coordinates, the kinetic energy operators for all three-body systems are identical except for an overall mass scaling factor. The fact that the potential surfaces in $\alpha$-set coordinates are similar for different systems immediately implies possible underlying similarities among these three-body Coulomb systems.

### 2.2.3. *Transformation brackets*

The three sets of Jacobi coordinates can be used to define three sets of hyperangles $\Omega^i \equiv (\phi^i, \hat{\xi}_1^i, \hat{\xi}_2^i)$ $(i = \alpha, \beta, \gamma)$. For each set of hyperangles, there exists a complete set of hyperspherical harmonics which are the solutions of

$$\left(-\frac{d^2}{d\phi^2} + \frac{l_1^2(\hat{\xi}_1)}{\cos^2\phi} + \frac{l_2^2(\hat{\xi}_2)}{\sin^2\phi} - (\lambda_{[k]}+2)^2\right) u_{[k]}(\Omega) = 0 \tag{2.18}$$

where $\lambda_{[k]} = l_1 + l_2 + 2m$ and all the indices and $\Omega$ depend on $i$. Each set of hyperspherical harmonics is similar to those given in (2.8)–(2.10), and satisfies the orthogonality condition similar to Eq. (2.11) within the given set.

The grand angular momentum operator does not depend on the Jacobi coordinates

$$\Lambda^2(\Omega^\alpha) = \Lambda^2(\Omega^\beta) = \Lambda^2(\Omega^\gamma), \tag{2.19}$$

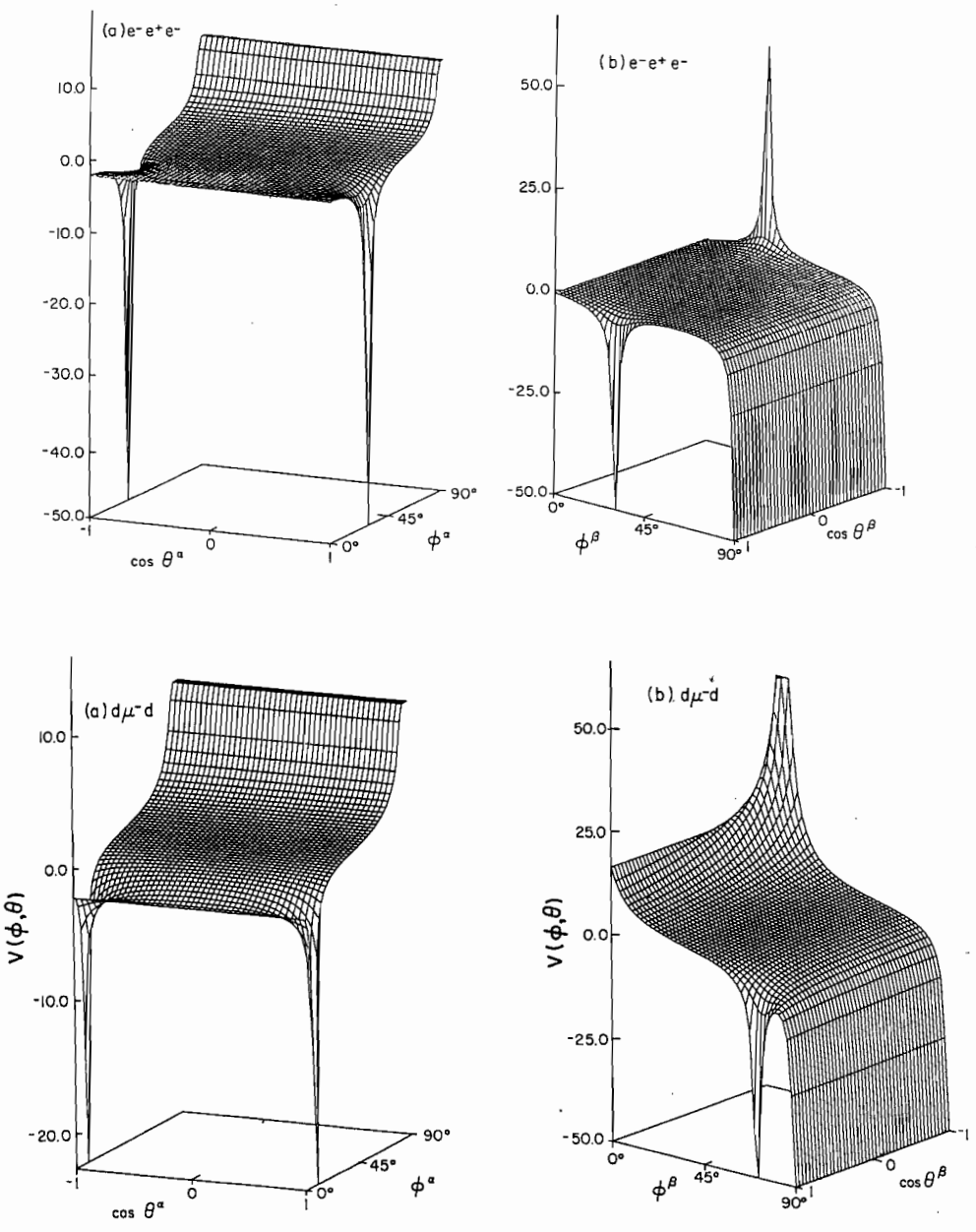


Fig. 2.4. (a) The potential surface for $e^-e^+e^-$ ions at $R = 1$ plotted against hyperspherical angles in $\alpha$-set and in $\beta$-set coordinates. (b) Similar potential surfaces for the $d^+\mu^-d^+$ system.

therefore, the hyperspherical harmonics in different sets of hyperangles are simply the different representations. The eigenfunctions in one set can be expanded in terms of eigenfunctions of the other set with $\lambda_{[k]} = \lambda_{[k']}$,

$$u_{[k]}(\Omega^i) = \sum_{[k']} A^{[i,k]}_{[j,k']}(\eta) u_{[k']}(\Omega^j) \tag{2.20}$$

where $\eta$ depends on the mass ratio of the system, and the expansion coefficients can be evaluated from

$$A^{[i,k]}_{[j,k']}(\eta) = \int d\Omega^j \, u^*_{[k]}(\Omega^i) u_{[k']}(\Omega^j). \tag{2.21}$$

These coefficients are called the transformation bracket and a program for their evaluation has been published [65]. These transformation brackets are useful when evaluating integrals involving functions of different sets of Jacobi coordinates.

### 2.3. Separation of wave functions in the body frame

#### 2.3.1. The body frame axes

The wave functions discussed so far refer to a space fixed reference frame. One can replace the five angles in hyperspherical coordinates by three Euler angles $\omega = (\omega_1, \omega_2, \omega_3)$ which describe the rotation of the whole system, and two other internal angles $\phi$ and $\theta$, as defined earlier, which describe the internal motion of the particles.

There are different possibilities for choosing the quantization axis of the body-frame for a three-body system. In chemical physics, it is common to choose one of the principal axes as the quantization axis. [20,18] For Coulomb three-body systems where two of the particles are identical, it has been found [66,67] that the axis connecting the two identical particles is an good approximate quantization axis (we remind the reader that this is the molecular axis if the mass of the two identical particles is much larger than the other one). This quantization axis is extended to systems where all three particles are different where the axis is along the line connecting the two particles of same sign of charges. The Coulomb repulsion between these two particles tends to push one away from the other and thus may serve as a better quantization axis. We mention that the "exact" solutions should not depend on how this body-frame quantization axis is defined.

Let the body-frame $z'$-axis to be along $\boldsymbol{\xi}_1^{\alpha}$. The $y'$-axis is defined to be along a direction perpendicular to the plane of the three particles,

$$\hat{t} = \frac{\boldsymbol{\xi}_1 \times \boldsymbol{\xi}_2}{|\boldsymbol{\xi}_1 \times \boldsymbol{\xi}_2|} \tag{2.22}$$

and the $x'$-axis is given by $\hat{t} \times \hat{\xi}_1$ such that the body-frame $(x', y', z')$ axes are the three triads $(\hat{t} \times \hat{\xi}_1, \hat{t}$ and $\hat{\xi}_1)$ and the Euler angles of the body-frame are $\omega = (\omega_1, \omega_2, \omega_3)$, with $\omega_2 = \theta_1$, $\omega_1 = \phi_1$ where $(\theta_1, \phi_1)$ are the spherical angles of $\hat{\xi}_1$. By expressing the angular momentum operators $l_1^2$ and $l_2^2$ in terms of the angular momentum operators with respect to the body-frame axes and the angle $\theta$, the grand angular momentum operator can be decomposed as

$$\Lambda^2 = T_0 + T_1 + T_2 - 1/4 \tag{2.23}$$

where the explicit expressions for the three operators $T_i$ $(i = 0, 1, 2)$ are

$$T_0 = \frac{\partial^2}{\partial \phi^2} - \frac{1}{\sin^2\phi \cos^2\phi} \frac{1}{\sin\theta} \frac{\partial}{\partial\theta} \left( \sin\theta \frac{\partial}{\partial\theta} \right)$$

$$T_1 = \frac{1}{\sin^2\phi\cos^2\phi}\frac{1}{\sin^2\theta}\hat{l}_{z'}^2 - \frac{1}{\cos^2\phi}(2\hat{l}_{z'}^2 - J^2)$$
$$T_2 = \frac{1}{\cos^2\phi}\left(2i\hat{l}_{y'}\frac{\partial}{\partial\theta_{12}} + 2\cot\theta\,\hat{l}_{x'}\hat{l}_{z'}\right), \tag{2.24}$$

where in terms of Euler angles,

$$\hat{l}_{x'} = -i\left(\sin\omega_3\frac{\partial}{\partial\omega_2} - \frac{\cos\omega_3}{\sin\omega_2}\frac{\partial}{\partial\omega_1} + \cot\omega_2\cos\omega_3\frac{\partial}{\partial\omega_3}\right)$$
$$\hat{l}_{y'} = -i\left(\cos\omega_3\frac{\partial}{\partial\omega_2} + \frac{\sin\omega_3}{\sin\omega_2}\frac{\partial}{\partial\omega_1} - \cot\omega_2\sin\omega_3\frac{\partial}{\partial\omega_3}\right)$$
$$\hat{l}_{z'} = -i\partial/\partial\omega_3 \tag{2.25}$$

and

$$J^2 = -\left[\frac{1}{\sin^2\omega_2}\frac{\partial^2}{\partial\omega_1^2} - \frac{2\cos\omega_2}{\sin^2\omega_2}\frac{\partial^2}{\partial\omega_1\partial\omega_3} + \frac{1}{\sin^2\omega_2}\frac{\partial^2}{\partial\omega_3^2} + \frac{1}{\sin\omega_2}\frac{\partial}{\partial\omega_2}\left(\sin\omega_2\frac{\partial}{\partial\omega_2}\right)\right]. \tag{2.26}$$

Notice that both $T_0$ and $T_1$ are diagonal with respect to the z′ axis of the body frame; only the $T_2$ operator mixes the different $m'$ components. It is obvious that the Schrödinger equation becomes much more complicated in the body-frame of reference, but it has the advantage that the internal motion is only coupled to the external rotation by the off-diagonal term in $T_2$ and that the rotational part of the wave function can be separated out.

### 2.3.2. *Decomposition of wave functions in the body-frame*

The channel function $\Phi_\mu(R;\Omega)$ can be expanded as

$$\Phi_\mu(R;\Omega) = \sum_{I=(1-\sigma)/2}^{J} \bar{D}^{JP}_{IM}(\omega)\psi^{\sigma}_{I\mu}(R;\theta,\phi) \tag{2.27}$$

where $J$ is the total orbital angular momentum and $I$ and $M$ are its projection along the body-fixed and laboratory-fixed $z'$ and $z$ axes, respectively. The parity $\sigma = \pm 1$ gives the reflection symmetry with respect to the plane of the three particles (the $x'z'$ plane) and the total parity of the system is $P = \sigma(-1)^J$. The symmetrized and normalized $\bar{D}$ functions in (2.27) are defined explicitly as

$$\bar{D}^{JP}_{IM}(\omega) = \frac{1}{4\pi}\sqrt{2J+1}\,\left[D^J_{IM}(\omega) + (-1)^{I+J}\,P\,D^J_{-IM}(\omega)\right]. \tag{2.28}$$

Substituting expansion (2.27) into (2.12) and averaging over the rotational functions, a system of $J+1$ equations for the functions $\psi$ for $\sigma = +1$, or a system of $J$ equations for $\sigma = -1$, is obtained. The nature of the resulting body-frame wave functions will be examined in Section 3.5.

## 2.4. *N-electron systems*

The hyperspherical method has been generalized, at least formally, to $N$-electron systems. We introduce the hyperspherical angles and hyperradius in a systematic way by defining

$$
\begin{aligned}
r_1 &= R \sin\alpha_N \sin\alpha_{N-1} \cdots \sin\alpha_3 \sin\alpha_2 \\
r_2 &= R \sin\alpha_N \sin\alpha_{N-1} \cdots \sin\alpha_3 \cos\alpha_2 \\
r_3 &= R \sin\alpha_N \sin\alpha_{N-1} \cdots \cos\alpha_3 \\
&\cdots \\
r_{N-1} &= R \sin\alpha_N \cos\alpha_{N-1} \\
r_N &= R \cos\alpha_N,
\end{aligned} \tag{2.29}
$$

and

$$
x_i = r_i \sin\theta_i \cos\phi_i, \qquad y_i = r_i \sin\theta_i \sin\phi_i, \qquad z_i = r_i \cos\theta_i. \tag{2.30}
$$

The Schrödinger equation can then be written as

$$
\left[-\frac{1}{2}\left(\frac{\partial^2}{\partial R^2} + \frac{\delta-1}{R}\frac{\partial}{\partial R} - \frac{\Lambda^2(N)}{R^2}\right) - \frac{Z(\Omega)}{R} - E\right]\Psi = 0 \tag{2.31}
$$

where $\delta = 3N$ is the dimension of the space and a recursive relation can be derived for the grand angular momentum operator $\Lambda^2(N)$

$$
\Lambda^2(N) = -\frac{\partial^2}{\partial\alpha_N^2} - \frac{(\delta-4)\cos^2\alpha_N - 2\sin^2\alpha_N}{\sin\alpha_N\cos\alpha_N}\frac{\partial}{\partial\alpha_N} + \frac{\hat{l}_N^2}{\cos^2\alpha_N} + \frac{\Lambda^2(N-1)}{\sin^2\alpha_N}. \tag{2.32}
$$

The eigenvalues and eigenfunctions for the $\Lambda^2$ operator are known,

$$
\Lambda^2(N)u_{\lambda N\mu}(\Omega) = \lambda_N(\lambda_N + \delta - 2)u_{\lambda N\mu}(\Omega) \tag{2.33}
$$

where

$$
\lambda_N = 2n_N + l_N + \lambda_{N-1} \tag{2.34}
$$

and the eigenfunctions are

$$
u_{\lambda n\mu}(\Omega) = \Pi_{j=2}^{N}\, \omega(n_j, l_j, \lambda_{j-1}|\cos^2\alpha_j)\; Y_{l_j m_j}(\theta_j, \phi_j)\; Y_{l_1 m_1}(\theta_1\phi_1) \tag{2.35}
$$

where $\mu$ denotes the set of quantum numbers

$$
\mu \equiv \{l_N, m_N; \lambda_{N-1} l_{N-1} m_{N-1}; \cdot\lambda_2 l_2 m_2; l_1 m_1\} \tag{2.36}
$$

and the $\omega$'s are defined as

$$
\begin{aligned}
&\omega(n_j, l_j, \lambda_{j-1}|\cos^2\alpha_j) \\
&\quad = (\cos\alpha_j)^{l_j}(\sin\alpha_j)^{\lambda_{j-1}} F(-n_j, n_j + \lambda_{j-1} + \tfrac{3}{2}j + l_j - 1, l_j + \tfrac{3}{2}|\cos^2\alpha_j)
\end{aligned} \tag{2.37}
$$

where $F$ is a Jacobi polynomial. While the nature of the hyperspherical harmonics for the $N$-body systems has been examined in the literature, along with the construction of properly (anti-)symmetrized basis functions [68], actual calculations for the $N$-electron systems have not been carried out to high accuracy. Construction of $N$-electron wave functions based on hyperspherical harmonics is not expected to be accurate for quantitative purposes. The limited calculations available

so far are of exploratory prototypes [69]. To reach the higher accuracy required in atomic and molecular systems, adiabatic expansion similar to the two-electron systems would be useful and the channel functions would have to be solved accurately. Recent effort toward this direction for three electron system can be found in Bao and Lin [70].

## 3. Methods of solving three-body problems in hyperspherical coordinates

### 3.1. Expansion in terms of hyperspherical harmonics

Since the set of hyperspherical harmonics forms a complete set on each hyperspherical surface, the solution of the Schrödinger equation can be expanded as

$$\Psi = \sum_{[k]} F_{[k]}(R) u_{[k]}(\Omega). \tag{3.1}$$

By projecting out the hyperspherical harmonics, a set of coupled second-order hyperradial differential equations is obtained [71,72]

$$\left[-\frac{1}{2}\left(\frac{\partial^2}{\partial R^2} + \frac{\delta-1}{R}\frac{\partial}{\partial R} - \frac{\lambda_N(\lambda_N+\delta-2)}{R^2}\right) - E\right] F_{[k]} - \frac{1}{R}\sum_{[k']} Z_{[k][k']} F_{[k']} = 0 \tag{3.2}$$

where we have written the general equation for the case of an $N$-electron system and where

$$Z_{[k][k']} = \langle u_{[k]} | C | u_{[k']} \rangle \tag{3.3}$$

is the matrix element of the effective charge $C$ evaluated between two hyperspherical harmonics.

Eq. (3.2) can be solved to obtain the eigenvalues if convergence can be achieved by using a reasonable truncated set of hyperspherical harmonics. The method has been applied by a number of authors to $H^-$ and He systems [10,73,74], but the rate of convergence is rather slow. Table 3.1 (the last column) shows the rate of convergence for the ground state energy of helium. By increasing the number of hyperspherical harmonics in the order of increasing values of $\lambda = l_1 + l_2 + 2n$, the number of hyperradial equations $N$ in Eq. (3.2) increases rapidly for large $\lambda$. Note that even with $\lambda_m$=16, the calculated ground state energy −2.89358 a.u. [75] is still rather poor, especially if one considers that

Table 3.1
Convergence of the ground state energy of helium versus the order of the hyperspherical harmonics used in the expansion. $\lambda_m$ is the order of the hyperspherical harmonics, and $N$ is the order of the coupled equations, see (3.2). The energies under the column EHH are obtained using Eq.(3.6) (data from [75,78]). The energies under the column H.H. are obtained using Eq.(3.1). The "converged" energy eigenvalue is 2.903724377 [79].

| $\lambda_m$ | $N$ | $E$(EHH) | $E$(H.H) |
|---|---|---|---|
| 0 | 1 | 2.9767604 | 2.5000 2 |
| 8 | 9 | 2.90321786 | 2.8502 2 |
| 16 | 25 | 2.90370440 | 2.8875 4 |
| 40 | 121 | 2.903724361 | |
| 48 | 169 | 2.903724368 | |

even a three-term variational calculation using Hylleraas-type function already can achieve a value of −2.902 44 a.u. [76] which is much closer to the nonrelativistic limit of −2.903 724 377 a.u. [77]

The slow convergence of the expansion (3.1) is not unexpected. The hyperspherical harmonics are good basis functions at small $R$ where the kinetic energy term $\lambda(\lambda+\delta-2)/R^2$ is dominant. At large $R$, the potential energy term $C/R$ is dominant where the wave function is expected to be localized in the deep valleys in the potential surface of Fig. 2.1. In this region the wave functions are products of two Slater functions which cannot be easily expanded in terms of a small number of hyperspherical harmonics.

The convergence of the expansion in (3.1) can be significantly improved if we introduce an exponential damping function. Thus, we write [75]

$$\Psi = \chi\Phi \tag{3.4}$$

where $\chi$ contains the damping terms, chosen to be of the form

$$\chi = \exp\{-[a(r_1+r_2) - br_{12}]\}, \tag{3.5}$$

where $a$ and $b$ are to be obtained variationally or by some ansatz. The equation satisfied by $\Phi$ is then

$$H'\Phi = E\Phi \tag{3.6}$$

with

$$H' = -(1/2)\nabla^2 + V' \tag{3.7}$$

$$V' = (-\nabla \ln\chi)\cdot\nabla - (1/2)\,(\nabla^2\chi/\chi) - Z/r_1 - Z/r_2 + 1/r_{12} \tag{3.8}$$

where $\nabla$ denotes the gradient operator in six dimensions. This transformation essentially removes the singularity in the Coulomb potential such that V′ is smooth everywhere if a and b are chosen appropriately. It is then possible to expand $\Phi$ in terms of hyperspherical harmonics and the convergence becomes very rapid. By choosing $a = 2$ and $b = 1/4$, Haftel and Mandelzweig [75] studied the convergence of the expansion of $\Phi$ for the ground state of helium as the maximum $\lambda_m$ is increased. The results are shown in Table 3.1. For $\lambda_m = 16$, they obtained the ground state energy of helium to be −2.903 704 40 a.u. For $\lambda_m = 48$, which results in a system of 169 coupled hyperradial equation, the energy they obtained is 2.903 724 368 [78] if the mass of the helium nucleus is assumed to be infinity. This value is to be compared to the value −2.903 724 377 obtained using the variational method by expanding the trial wave function in the form of Fock expansion [77,79]. For the 1s2s $^1S^e$ state, they chose $a = 2$ and $b = 0$ and obtained a result of −2.145 968 877 a.u. for $\lambda_m = 48$, which is to be compared to the value −2.145 974 046 a.u. [79]

The expansion of the whole wave function in the form of (3.1) is not practical for dealing with a large number of higher excited states, especially doubly excited states and the continuum wave functions.

### *3.2. The adiabatic approximation*

As pointed out in the introduction, the rapid progress in the hyperspherical approach to three-body systems owes much to the introduction of the adiabatic approximation (1.4) where the hyperradius $R$

is treated as a slow-varying parameter. Using the expansion (1.4), the adiabatic function $\Phi_\mu(R;\Omega)$ satisfies the equation

$$[\Lambda^2/R^2 + C/R]\,\Phi_\mu(R;\Omega) = U_\mu(R)\Phi_\mu(R;\Omega) \tag{3.9}$$

where $\Lambda^2$ is given by Eq. (2.5) or (2.23) and $C$ is given by (2.6) or (2.17) and the hyperradial functions satisfy the coupled equations

$$\left(-\frac{d^2}{dR^2} + U_\mu(R) - 2E\right) F_\mu(R) = \sum_\nu \left(2\langle\Phi_\mu|\frac{d}{dR}|\Phi_\nu\rangle\frac{d}{dR} + \langle\Phi_\mu|\frac{d^2}{dR^2}|\Phi_\nu\rangle\right) F_\nu(R). \tag{3.10}$$

The adiabatic approximation is useful if the off-diagonal coupling terms are small. In this case, the index $\mu$ can be used to label the "channels". The hyperradial function gives the size of the state, but the internal motion, together with the overall rotation of the whole system, is contained in the channel function. One of the major goals in the study of three-body and few-body systems is to identify the different modes of the internal motion which in turn are to provide meaningful quantum numbers as represented implicitly by the channel index $\mu$.

### *3.3. Numerical methods for the solution of the channel functions: expansion of the wave function in the laboratory frame*

#### *3.3.1. Two-electron atoms*

We first consider the application of hyperspherical method to two-electron systems. The adiabatic Hamiltonian takes the form

$$H_{\rm ad} = (1/R^2)(\Lambda^2 + RC) \tag{3.11}$$

where

$$\Lambda^2 = -\frac{\partial^2}{\partial\alpha^2} + \frac{l_1^2}{\cos^2\alpha} + \frac{l_2^2}{\sin^2\alpha} - \frac{1}{4} \tag{3.12}$$

Since the nonrelativistic Hamiltonian commutes with $L$, $S$, the total orbital and spin angular momentum, respectively, and the parity $\pi$, the solution of (3.9) can be expanded as

$$\Phi_\mu(R;\Omega) = A\sum_{[l_1 l_2]} f_{l_1 l_2}(R;\alpha)\, y_{l_1 l_2 LM}(\hat{r}_1, \hat{r}_2) \tag{3.13}$$

where $A$ is the symmetrization (or antisymmetrization) operator, and the summation is over *pairs* of $l_1$ and $l_2$. In (3.13) the spin wave function is not explicitly written. Thus, if the spatial wave function (3.13) is symmetric under electron exchange, the spin wave function is antisymmetric, and vise versa. Substitution of (3.13) into (3.9) gives a set of coupled differential equations for $f_{l_1 l_2}(R;\alpha)$ that are to be solved with the boundary conditions that the wave functions vanish at $\alpha = 0$ and 90°. Note that the functions $f_{l_1 l_2}(R;\alpha)$ should approach the hyperspherical harmonics at $R = 0$ and hydrogenic functions at larger $R$.

The set of coupled equations have been solved over the years using different methods:

(a) Direct numerical integration of the coupled differential equations. This method was first adopted by Macek [12] and applied to the study of doubly excited states of He. The method suffers from numerical instability, especially in the region where the eigenvalues are nearly degenerate.

(b) Diagonalization using hyperspherical harmonics. This was used by Lin [80] but it was found that the convergence is rather slow, especially in the region of large hyperradius.

(c) Diagonalization using analytical channel functions. This method was adopted by Lin [81] where hydrogenic basis functions in the asymptotic region is generalized to the region of small $R$. Together with hyperspherical harmonics, these basis functions were used to diagonalize the adiabatic Hamiltonian to obtain potential curves and channel functions. This method is quite accurate and very stable and only a small basis set is needed to achieve good numerical accuracy. It has been used extensively in many calculations [51,4,82,83].

(d) Generalized Numerov method. This is a method adopted by Tang et al. [84] using the three-term recursion formula of the generalized Numerov method, as previously discussed by Seaton [85]. This method is accurate to the sixth power of the step size and permits the use of variable step sizes. The latter is rather important since the function $f_{l_1 l_2}(R;\alpha)$ spreads over the whole range of $\alpha$ (between 0 and $\pi/2$) at small $R$, but is confined in the region near $\alpha \to 0$ and $\alpha \to \pi/2$ at large $R$. The three-term recursion gives a generalized eigenvalue problem

$$AX = U(R)BX \tag{3.14}$$

where $A$ and $B$ are tridiagonal nonsymmetric matrices in the subspace with fixed $l_1 l_2$. Since a general method for solving nonsparse matrices is rather time consuming, it is actually easier to solve Eq. (3.14) by seeking the zeros of the determinantal equation

$$\det(A - U(R)B) = 0. \tag{3.15}$$

This equation is solved iteratively. The procedure is accelerated by the knowledge of the approximate values of $U(R)$ which are extrapolated from the values obtained at somewhat smaller $R$. The construction starts at $R = 0$ where the analytical result is

$$U(R) = (l_1 + l_2 + 2n)^2, \quad n = 0, 1, 2, \ldots \tag{3.16}$$

This method provides the highest numerical accuracy and has been applied to recent numerical calculations involving two-electron systems (see Section 6.1).

### 3.3.2. *General Coulombic three-body systems*

Using mass-weighted hyperspherical coordinates, the adiabatic equation for the general Coulombic three-body systems has the same form as that for the two-electron atom except that the Coulomb potential terms are now weighted with the masses of the system and that there are three equivalent sets of Jacobi coordinates from which the hyperspherical angles can be constructed. For an $A^+B^+C^-$ system, it is obvious that in the dissociation limit the $\beta$-set coordinates are mostly suitable for describing the $A^+ + (B^+C^-)$ states, while the $\gamma$-set is best for describing the $B^+ + (A^+C^-)$ states. In the region where all the three particles are close to each other, any of the three sets of Jacobi coordinates are acceptable. To account for the dissociation limits correctly, it is thus best to introduce basis functions which include both the $\beta$-set and the $\gamma$-set Jacobi coordinates. Thus one approach for solving the adiabatic functions is to adopt basis functions in both the $\beta$-set and $\gamma$-set coordinates. If the system consists of two identical particles , then the basis functions are

$$g_i(R;\Omega) = g_i(R;\Omega^\beta) + (-1)^{l_1^\beta + S}\, g_i(R;\Omega^\gamma) \tag{3.17}$$

where the functions on the right are identical to those employed in the two-electron problems, see Eq. (3.13), but without the antisymmetrization operator.

The use of $\beta$-set and $\gamma$-set functions allows us to calculate $U_\nu(R)$ using only a small set of $(l_1 l_2)$ pairs in the expansion since $l_1^\beta$ refers to a bound state of the (BC) system which has small $l_1^\beta$ for low-lying bound states and $l_2^\beta$ is governed by the triangular relation among $l_1^\beta$, $l_2^\beta$ and $L$. Using such a basis set from different coordinate systems, it is possible to carry out calculations for the potential curves easily. [48,86] The major task is to calculate the Hamiltonian matrix elements between basis functions from different coordinates. One method of calculating such matrix elements is to expand the basis functions in, say, the $\beta$-set, in terms of hyperspherical harmonics in the $\beta$-set. To express the wave functions in the $\gamma$-set, one then uses the transformation brackets [65] which then express all the functions in the $\gamma$-set coordinates. Thus the matrix elements can then be expressed in terms of variables in the $\gamma$-set coordinates. Another approach which is straightforward is to use the so-called kinematic rotation [13] which relates the coordinates of the different sets of Jacobi coordinates. Both approaches become less accurate at large hyperradius.

The basis functions of the form of (3.17) have been used in calculations by Chen and Lin [48], by Liu et al. [86] and by Igarashi and Toshima [87]. It works rather well if the basis set is not too large. When a large basis set is used, the linear dependence due to the nonorthogonality of basis functions from the $\beta$-set and the $\gamma$-set should be considered.

### *3.4. The hyperspherical close coupling (HSCC) method*

The expansion (1.4) of the wave function in terms of adiabatic basis functions requires the solution of the coupled second-order differential equations (3.10). The nonadiabatic coupling terms in this equation vary rapidly near the localized avoided crossings which are very difficult to evaluate numerically. Although there exist a number of calculations where Eq. (3.10) has been solved numerically, the number of channels included in these calculations is very limited [88,89] and the achieved accuracy is far from spectacular. Another well-known limitation of the adiabatic expansion (1.4) is that it has incorrect asymptotic form. At large hyperradius, the three-body system dissociates into A + (BC) or B+ (AC). To describe these asymptotic limits correctly, for example, for the A+ (BC) combination, the wave function has the form $F(\rho_1)G(\rho_2)$ where the $\rho$'s are defined with respect to the $\beta$-set Jacobi coordinates. Using the expansion (1.4) would result in nonvanishing coupling terms even in the asymptotic region. In fact, if the adiabatic basis functions are used, the nonadiabatic coupling term $\langle \Phi_\mu | d/dR | \Phi_\nu \rangle$ decreases proportionally to $1/R$ at large $R$ [90].

These difficulties associated with the adiabatic expansion can be circumvented in the so-called hyperspherical close-coupling method (HSCC). In the HSCC method, one first partitions the range of hyperradius into many small sectors. Within each sector the whole wave function is expanded in the form

$$\Psi(R, \Omega) = \sum_\mu F_\mu(R)\, \Phi_\mu(R_a; \Omega), \tag{3.18}$$

where $R_a$ is a point within the sector. The basis functions $\Phi_\mu$'s are fixed within the sector and chosen to satisfy Eq. (3.9) at $R_a$. Thus the basis functions are diabatic within the sector and the hyperradial equations within this sector satisfy

$$\left(-\frac{d^2}{dR^2} - 2E\right) F_\mu(R) + \sum_\nu V_{\mu\nu}(R) F_\nu(R) = 0. \tag{3.19}$$

where $V_{\mu\nu}(R) = \langle \Phi_\mu | H_{ad} | \Phi_\nu \rangle$. The coupling terms thus obtained are smooth functions of R within the sector. Beyond this sector, a new diabatic basis set is generated. At the boundary between the two sectors, a local frame transformation matrix

$$T_{\mu,\nu} = \langle \Phi_\mu(R_a) | \Phi_\nu(R_b) \rangle, \tag{3.20}$$

is required in propagating the logarithmic derivative. The unitarity of $T$ serves as a way to check whether the sector size is appropriate. In actual calculations, a breakdown of unitarity of the order of a few parts per $10^4$ is acceptable.

Once the solutions are propagated to the asymptotic region, they are matched to the asymptotic solutions which are expressed in separable functions in appropriate Jacobi coordinates from where the reaction matrix $K_{ij}$ is extracted.

In the discussion of the HSCC method so far, the wave functions in the inner and the asymptotic regions are all expressed in the laboratory-fixed system. In the following we address the procedure where the wave functions are expressed in the body-fixed frames.

### 3.5. *Expansion of the wave functions in the body-fixed frame*

The Schrödinger equation in the body-frame has been discussed in Section 2.3. In the diabatic-by-sector method the wave function $\Psi$ is expanded in terms of $\bar{D}$ and the diabatic-by-sector bases $\Phi_{\mu l}(R_a; \theta, \phi)$,

$$\Psi(R, \phi, \hat{\Omega}) = \sum_\mu \sum_l F_{\mu l}(R) \Phi_{\mu l}(R_a; \theta, \phi) \bar{D}^J_{lM_J}(\omega_1, \omega_2, \omega_3). \tag{3.21}$$

The diabatic basis function satisfies

$$\left(\frac{T_0 + \langle \bar{D}^J_{lM_J} | T_1 | \bar{D}^J_{lM_J} \rangle}{R_a^2} + \frac{2\mu C}{R_a}\right) \Phi_{\mu l}(R_a; \theta, \phi) = 2\mu U_{\mu l}(R_a) \Phi_{\mu l}(R_a; \theta, \phi), \tag{3.22}$$

with $0 \le \theta \le \pi$ and $0 \le \phi \le \pi/2$. Here

$$\langle \bar{D}^J_{lM_J} | T_1 | \bar{D}^J_{lM_J} \rangle = \frac{I^2}{\sin^2\phi \cos^2\phi \sin^2\theta} + \frac{J(J+1) - 2I^2}{\cos^2\phi}. \tag{3.23}$$

Within the sector, the hyperradial functions $F_{\mu l}$ then satisfy the coupled differential equations

$$\left(-\frac{\partial^2}{\partial R^2} - \frac{1}{4R^2} - 2\mu E\right) F_{\mu l}(R) + \sum_{\nu l'} V_{\mu l, \nu l'}(R) F_{\nu l'}(R) = 0, \tag{3.24}$$

where

$$V_{\mu l, \nu l'}(R) = \langle \Phi_{\mu l}(R_a; \theta, \phi) \bar{D}^J_{lM_J} | \frac{T_0 + T_1 + T_2}{R^2} + \frac{2\mu C}{R} | \Phi_{\nu l'}(R_a; \theta, \phi) \bar{D}^J_{l'M_J} \rangle. \tag{3.25}$$

The solution of the Schrödinger equation then consists of the following steps:

- (a) Within each diabatic sector,
  - 1. solve $\Phi_{\mu I}$ within each sector at $R_a$;
  - 2. calculate the matrix elements $V_{\mu I,\mu' I'}(R)$;
  - 3. integrate the coupled equations from $R_i$ to $R_{i+1}$.
- (b) Match the solutions at $R_{i+1}$ to the next sector and then repeat the procedure until a large $R_0$.
- (c) Match the solution from the interior region at $R_0$ to the asymptotic solutions expressed in terms of functions using Jacobi coordinates to obtain the $K$-matrix.

In the following, these steps are described.

*3.5.1. Finite element method of solving the 2D equations*

A major obstacle in the application of hyperspherical method to achieve high accuracy is related to the difficulty of solving the "channel functions" $\Phi_{\mu I}$ at $R_a$ accurately. In atom-diatom reactive scattering calculations, different approaches have been adopted (see [20]). For the general Coulomb three-body systems, it has been found that a higher-order finite-element method [91]can achieve the high accuracy needed for the potential curves. In fact, when it is applied to the two-electron systems, the higher order FEM results are in good agreement with the accuracy achieved using the generalized Numerov method (see Section 3.3.1). In the FEM method, the $(\theta, \phi)$ plane is divided into a number of rectangles and each is called an element $\epsilon$. The channel function $\Phi_{\mu I}$ can be expanded as

$$\Phi_{\mu I}(R_a;\theta,\phi) = \sum_{\epsilon} \sum_{j=1}^{36} \tilde{U}^{(\epsilon)}_{\mu I,j}(R_a)\ \chi^{(\epsilon)}_j(R_a;\theta,\phi) \tag{3.26}$$

where within each element $\epsilon$, the channel function is expanded in terms of local basis $\chi$ [92,91] which are products of fifth order polynomials in $\theta$ and $\phi$, and nonzero only in the element $\epsilon$. The 36 expansion coefficients are the values of $\Phi_{\mu I}$ and its derivatives $\partial\phi_{\mu I}/\partial\theta, \partial\Phi_{\mu I}/\partial\phi, \partial^2\Phi_{\mu I}/\partial\theta\partial\phi$ at the nine nodes of the element $\epsilon$. Substitution of (3.26) into the (3.22) results in a set of linear coupled equations for the expansion coefficients for the local element $\epsilon$:

$$H^{(\epsilon)}_I\ \tilde{U}^{(\epsilon)}_{\mu I}(R_a) = 2\mu\ U_{\mu I}(R_a)\ B^{(\epsilon)}\ \tilde{U}^{(\epsilon)}_{\mu I}(R_a) \tag{3.27}$$

where integration over the element $\epsilon$ has been carried out and B is the overlap matrix of the local basis. After coupling together the local equations, a global matrix equation

$$H\tilde{U}_{\mu I}(R_a) = 2\mu\, U_{\mu I}(R_a)\ B\ \tilde{U}_{\mu I}(R_a) \tag{3.28}$$

is obtained. The solution of this equation gives the eigenvalues and the eigenfunctions. In the calculation of Zhou and Lin [93] for positron scattering with atomic hydrogen, the $\alpha$-set basis is used and the $(\theta, \phi)$ plane was divided into 240 rectangular elements, 10 in $\theta$ and 24 in $\phi$.

*3.5.2. The evaluation of the coupling terms*

It is clear that the operator $T_0 + T_1$ is diagonal with respect to $I$, the projection of the total angular momentum along the body-frame quantization axis, while $T_2$ couples $I$ and $I'$ channels only where $I' = I \pm 1$. Thus $T_2$ corresponds to the rotational coupling in atomic collisions, and the off-diagonal terms of $T_0 + T_1$ between channels of identical $I$ are the "potential coupling" when diabatic basis functions are used as in the present case. Following the straightforward algebra the matrix elements are

$$\langle \Phi_{\mu I}(R_a;\theta,\phi)\bar{D}^J_{IM_J}|\frac{T_0+T_1}{R^2}+\frac{2\mu C}{R}|\Phi_{\nu I'}(R_a;\theta,\phi)\bar{D}^J_{I'M_J}\rangle$$
$$=\langle \Phi_{\mu I}(R_a;\theta,\phi)\bar{D}^J_{IM_J}|\frac{T_0+T_1}{R_a^2}\frac{R_a^2}{R^2}+\frac{2\mu C}{R}|\Phi_{\nu I'}(R_a;\theta,\phi)\bar{D}^J_{I'M_J}\rangle$$
$$=\langle \Phi_{\mu I}(R_a;\theta,\phi)\bar{D}^J_{IM_J}|2\mu(U_{I'\nu}-\frac{C}{R_a})\frac{R_a^2}{R^2}+\frac{2\mu C}{R}|\Phi_{\nu I'}(R_a;\theta,\phi)\bar{D}^J_{I'M_J}\rangle$$
$$=(2\mu/R^2)\left[R_a^2U_{I\mu}(R_a)\delta_{\mu\nu}+(R-R_a)C_{\mu\nu I}\right]\delta_{II'}, \tag{3.29}$$

and

$$\langle \Phi_{\mu I}(R_a;\theta,\phi)\bar{D}^J_{IM_J}|T_2|\Phi_{\nu I'}(R_a;\theta,\phi)\bar{D}^J_{I'M_J}\rangle$$
$$=\langle \Phi_{\mu I}(R_a;\theta,\phi)|h_{II+1}|\Phi_{\nu I+1}(R_a;\theta,\phi)\rangle\delta_{I'I+1}$$
$$+\langle \Phi_{\mu I}(R_a;\theta,\phi)|h_{II-1}|\Phi_{\nu I-1}(R_a;\theta,\phi)\rangle\delta_{I'I-1} \tag{3.30}$$

with

$$C_{\mu\nu I}=\langle \Phi_{\mu I}(R_a;\theta,\phi)|C|\Phi_{\nu I}(R_a;\theta,\phi)\rangle$$
$$h_{II\pm1}=\frac{\gamma^J_{II\pm1}}{\cos^2\phi}\left(\pm\frac{\partial}{\partial\theta}+(I\pm1)\cot\theta\right)$$
$$\gamma^J_{II+1}=-\left[1+(\sqrt{2}-1)\delta_{I0}\right]\left[(J+I+1)(J-I)\right]^{1/2}$$
$$\gamma^J_{II-1}=-\left[1+(\sqrt{2}-1)\delta_{I1}\right]\left[(J-I+1)(J+I)\right]^{1/2}. \tag{3.31}$$

Thus $V_{\mu I,\nu I'}(R)$ is given explicitly by

$$V_{\mu I,\nu I'}(R)=\frac{2\mu}{R^2}\left[R_a^2U_{I\mu}\delta_{\mu\nu}+(R-R_a)C_{\mu\nu I}\right]\delta_{II'}$$
$$+\frac{1}{R^2}\left[\langle \Phi_{\mu I}(R_a;\theta,\phi)|h_{II+1}|\Phi_{\nu I+1}(R_a;\theta,\phi)\rangle\delta_{I'I+1}\right.$$
$$\left.+\langle \Phi_{\mu I}(R_a;\theta,\phi)|h_{II-1}|\Phi_{\nu I-1}(R_a;\theta,\phi)\rangle\delta_{I'I-1}\right]. \tag{3.32}$$

These matrix elements are identical to those derived by Kadomstsev and Vinitsky [94] except that the angle $\phi$ defined by them is twice of what was used here.

*3.5.3. Propagation from one sector to the next sector*

At the boundary ($R=R_x$) of the sector $i$ and sector $i+1$, the condition of continuity of the wave function at $R_x$

$$\sum_j F^L_j(R_x)\Phi_j(R_i;\Omega)=\sum_j F^R_j(R_x)\,\Phi_j(R_{i+1};\Omega) \tag{3.33}$$

allows one to obtain the hyperradial functions $F^R_i(R_x)$ on the right sector in terms of the hyperradial functions $F^L_i(R_x)$ on the left sector,

$$F^R_k(R_s)=\sum_j T_{kj}\,F^L_j(R_x) \tag{3.34}$$

where

$$T_{kj} = \langle \Phi_k(R_{i+1}; \Omega) | \Phi_j(R_i; \Omega) \rangle \tag{3.35}$$

is the overlap matrix. In (3.33) $R_i$ and $R_{i+1}$ are within the sector $i$ and $i+1$, respectively, where the "channel" functions are calculated. In general one chooses such a point to be at the midpoint of the sector.

We note that the same transformation (3.34) applies to the derivatives of the hyperradial functions with respect to $R$.

*3.5.4. Asymptotic solutions and two-dimensional matching*

The procedure outlined above can be continued up to a large $R_0$ beyond which where one particle is far away from the other pair of particles. In this asymptotic region, the asymptotic wave function $\psi_A^{(\lambda)}$ of the dissociated system is better represented by

$$\psi_A^{(\lambda)}(\boldsymbol{\rho}_1, \boldsymbol{\rho}_2) = \sum_{i=1}^{N} \frac{\varphi_i(\rho_1^\tau)\, y_{l_1^\tau l_2^\tau JM_J}(\hat{\Omega}_1^\tau, \hat{\Omega}_2^\tau)\, [f_\lambda(\rho_2^\tau)\delta_{i\lambda} - g_i(\rho_2^\tau) K_{i\lambda}]}{\rho_1^\tau \rho_2^\tau}, \tag{3.36}$$

where $\varphi_i(\rho_1^\tau)$'s are the bound state wave functions for the $\tau$ arrangement. In the equation, $f$'s and $g$'s are velocity-normalized regular and irregular spherical Bessel functions $(1/\sqrt{v^\tau})j_{l_2^\tau}$ and $(1/\sqrt{v^\tau})n_{l_2^\tau}$, respectively, with $v^\tau$ as the relative velocity of the particle pair and the far-away particle in the $\tau$ arrangement, $K_{i\lambda}$ is the element of the $K$ matrix, and the $y$'s are the coupled angular momentum functions.

The matching of the two solutions at $R_0$ becomes

$$\frac{1}{R_0^{5/2} \sin\phi \cos\phi} \sum_{\sigma=1}^{N} H_\sigma^\lambda \Psi^{(\sigma)}(R_0, \phi, \hat{\Omega}) = \psi_A^{(\lambda)}(\boldsymbol{\rho}_1, \boldsymbol{\rho}_2)\,|_{R=R_0} \tag{3.37}$$

with $H_\sigma^\lambda$ being the expansion coefficients.

The asymptotic wave function $\psi_A^{(\lambda)}(\boldsymbol{\rho}_1, \boldsymbol{\rho}_2)$ as given in Eq. (3.36) is expressed in the laboratory fixed frame. To solve Eq. (3.37), one needs to expand it by referring to the body frame. Note that

$$y_{l_1^\tau l_2^\tau JM_J}(\hat{\Omega}_1^\tau, \hat{\Omega}_2^\tau) = \sqrt{\frac{16\pi^2}{2J+1}} \sum_{I}^{J} \frac{\bar{D}^J_{IM_J}(\omega_1, \omega_2, \omega_3)}{1 + (\sqrt{2}-1)\delta_{I0}} y_{l_1^\tau l_2^\tau JI}(\hat{\Omega}_1^{\tau(\text{body})}, \hat{\Omega}_2^{\tau(\text{body})}). \tag{3.38}$$

Here, $\hat{\Omega}_1^\tau = (\theta_1^\tau, \phi_1^\tau)$, $\hat{\Omega}_2^\tau = (\theta_2^\tau, \phi_2^\tau)$ are the orientation angles of vectors $\boldsymbol{\rho}_1$ and $\boldsymbol{\rho}_2$ for the $\tau$ arrangement. The superscript (body) indicates that these angles are measured in the body frame. By equating the coefficients of $\bar{D}^J_{IM_J}$ functions on both sides of Eq. (3.37) and then integrating over the angles $\theta, \phi$, Eq. (3.37) can be cast in the form

$$\sum_{\sigma=1}^{N} H_\sigma^\lambda F_{\mu I}^{(\sigma)}(R_0) = R_0^{1/2} \left( J_{\mu I}^\lambda - \sum_{i=1}^{N} N_{\mu I}^i K_{i\lambda} \right), \tag{3.39}$$

where $J_{\mu I}^\lambda$ and $N_{\mu I}^\lambda$ are matrix elements after Eq.(3.37) has been integrated over the hyperspherical surface at $R_0$. Eq. (3.39) can also be expressed in matrix form

$$\boldsymbol{F}\boldsymbol{H} = R_0^{1/2}[\boldsymbol{J} - \boldsymbol{N}\boldsymbol{K}]. \tag{3.40}$$

Similarly, by requiring that the derivative of the wave function with respect to $R$ be continuous at $R_0$, we obtain an equation similar to (3.40),

$$\boldsymbol{F}'\boldsymbol{H} = R_0^{1/2}[\boldsymbol{J}' - \boldsymbol{N}'\boldsymbol{K}], \tag{3.41}$$

After defining the log-derivative matrix

$$\boldsymbol{Y} = \boldsymbol{F}'\boldsymbol{F}^{-1} \tag{3.42}$$

and from Eqs. (3.40) and (3.41), we finally obtain the $K$ matrix

$$\boldsymbol{K} = [\boldsymbol{Y}\boldsymbol{N} - \boldsymbol{N}']^{-1}[\boldsymbol{Y}\boldsymbol{J} - \boldsymbol{J}']. \tag{3.43}$$

From the $K$ matrix, the partial cross section is

$$\sigma_{ij}^{(J)} = \frac{4\pi(2J+1)}{k^2}\left|\frac{K}{1-iK}\right|_{ij}^2 \tag{3.44}$$

with $k$ as the incident momentum. The procedure outlined above is called the two-dimensional matching method. If the wave function is expressed in the laboratory frame, then one does not need to rewrite the wave function in the asymptotic region in terms of $\bar{D}$ functions. Otherwise, the matching procedure is essentially identical.

## 4. Applications of hyperspherical methods to atomic systems in the adiabatic approximation

In this section, we will limit the discussion of the applications of hyperspherical coordinates to two-electron atoms. Although hyperspherical coordinates have been used to obtain accurate energy levels and wave functions for the ground state and the first few excited states by a few groups in the past (see Section 3.1), these calculations were carried out using variational methods and the nature of atoms in these states are already well understood. Major progress in the application of hyperspherical coordinates in the last two decades occurred in the study of doubly excited states where methods based on hyperspherical coordinates not only provide a convenient framework for the understanding of these states, but efficient and accurate computational methods have also been developed in the last few years. In this section we will focus on the application of hyperspherical coordinates within the adiabatic approximation. The results thus obtained provide a qualitative understanding of the properties of these states and offer a new classification scheme. Discussions of full calculations including the couplings among adiabatic channels will be postponed until Section 6.1.

### *4.1. Doubly excited states of two-electron atoms*

#### *4.1.1. A brief historical remark*

The first application of hyperspherical coordinates to doubly excited states of atoms was carried out by Macek in 1968 [12]. Using the adiabatic approximation, Macek showed that the energy levels calculated from the three $^1P^0$ curves below the $He^+(N = 2)$ threshold are very close to the energy levels of the three Rydberg series which had been calculated by other approaches and the calculated energy positions are in good agreement with experiments [95]. This calculation established the

approximate validity of treating the hyperradius as an adiabatic parameter and that one can associate a Rydberg series to an individual hyperspherical potential curve. The nature of the "channel functions" which are functions of hyperangles at a fixed hyperradius was examined by Lin [80]. The next major application of the hyperspherical method was to the $H^-$ system where electron correlation is stronger than in He. The three potential curves for the $^1P^0$ states of $H^-$ that converge to the $H(N = 2)$ limit were calculated by Lin [97]. From the calculated potential curves the existence of Feshbach and shape resonances in $H^-$ was established. These resonances were later confirmed nicely in the experiment by Bryant et al. [98]

The early applications of hyperspherical methods were often plagued by the inefficient and/or inaccurate numerical methods used. With the introduction of analytical channel functions [81] and the improving computing speeds and computer graphics, it became possible in the early 80's to examine the interrelation of the channel functions of doubly excited states of different symmetries together. Using the earlier algebraic results as guidance, [99] a complete set of approximate quantum numbers was introduced to label the hyperspherical potential curves [51] and the meanings of the quantum numbers and their relations with the correlation patterns were examined. Thus the classification of doubly excited states can be carried out within the adiabatic approximation using hyperspherical coordinates.

*4.1.2. The global features of the spectra of He and $H^-$*

We first illustrate the global features of the hyperspherical potential curves for He and $H^-$ for the $^1P^o$ symmetry [100]. Because the number of channels converging to each of the $N$th excited threshold of $He^+$ or H is $2N+1$, the number of potential curves increases very rapidly with increasing values of $N$. Furthermore, the size of the excited state for a system under the Coulomb interaction is proportional to the square of the principal quantum number, and the energy level is inversely proportional to the square of the principal quantum number. In Fig. 4.1 the adiabatic potential curves that converge to the $N = 2$ to $N = 10$ are shown, where the vertical axis is the effective principal quantum number and the horizontal axis is $\sqrt{(}ZR)$. Thus, each curve that approaches the $N$th excited state of $He^+$ or H will have $\nu_\mu$ equals to $N$.

These potential curves show the intrinsic complexities of the spectra of He and $H^-$ despite the fact that they are "simple" two-electron atoms. So far high precision experimental data for these systems can resolve well states that are below the $N = 6$ or 7 thresholds only [101,102].

A set of simpler potential curves can be obtained if one displays only the lowest two potential curves of Fig. 4.1 for each $N$ for $N > 3$. The potential curves thus obtained are redisplayed in Fig. 4.2. According to the adiabatic approximation, the energy eigenvalues from each curve can be calculated by solving the eigenvalues from each curve, and the results are shown as horizontal lines in the figure. Note that for low $N$, the minimum of the potential curve associated with the $N$th threshold never crosses below the asymptotic limit of the $(N-1)$th threshold. Thus the energy levels from each adiabatic potential curve never overlap with the levels from the higher threshold. This is not the case as $N$ becomes large. A careful examination shows that the lowest state associated with the $N = 5$ curve lies below the $N = 4$ threshold for He. The presence of this interloper state can cause interference with the Rydberg states below the $N = 4$ threshold to produce rapid local spectral variation. At even higher energies, energy levels associated with individual adiabatic hyperspherical potential curves from different thresholds will overlap, and the interaction among these adiabatic

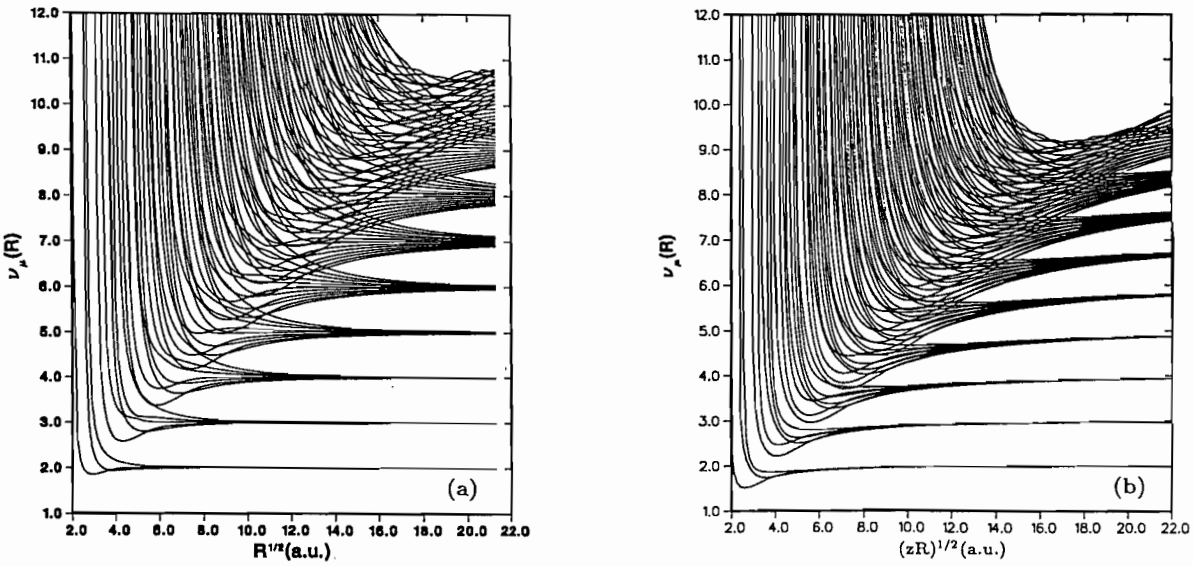


Fig. 4.1. (a) Adiabatic hyperspherical potential curves for the $^1P^o$ symmetry of $H^-$ shown as effective quantum number $\nu_\mu(R)$ versus $\sqrt{R}$. (b) The same potentials but for He (from Sadeghpour [100]).

channels would result possibly new spectral features. This is the energy region where classical chaos is expected to play an important role in the understanding of the behavior of two electrons in an atom. However, there are still no good experimental data in this energy region.

In the following sections, the global potential curves of Figs. 4.1 and 4.2 will be examined in more detail and the important results will be extracted so the results can be compared to experimental data or other calculations.

### *4.1.3. Low-lying states of $H^-$ and He within the adiabatic approximation*

*4.1.3.1. The ground state and the elastic scattering phase shift.* We first illustrate the application of the adiabatic approximation to the ground state of $H^-$ and the elastic scattering phase shift for electron-hydrogen atom collisions at low energies. These properties of $H^-$ have been extensively studied by many other approaches. In Fig. 4.3 we show the lowest adiabatic potential curve for the $^1S^e$ symmetry of $H^-$. The ground state energy calculated from the lowest curve is $-1.0547$ Ry which is to be compared with the experimental result of $-1.05546$ Ry. This result is satisfactory considering that only one channel is included. One can improve the result if the coupling with higher adiabatic channels is included. For example, the 10, 20 and 28 channel results of Tang et al. [103] are $-1.05530$, $-1.05544$ and $-1.05546$ Ry, respectively, which differ little from the variational value of $-1.0555$ Ry [104].

In calculating the potential curve in Fig. 4.3, $(l_1, l_2) = (0,0)$, (1,1) and (2,2) were included [see Eq. (3.13)]. If one assumes that the angular momentum of each electron is restricted to $l = 0$ only, then the energy calculated from the adiabatic hyperspherical potential curve is $-1.02617$ Ry. Since the Hartree–Fock calculation does not predict the existence of a bound state for $H^-$, this result indicates that more electron correlation is included in the adiabatic approximation than in the HF approximation.

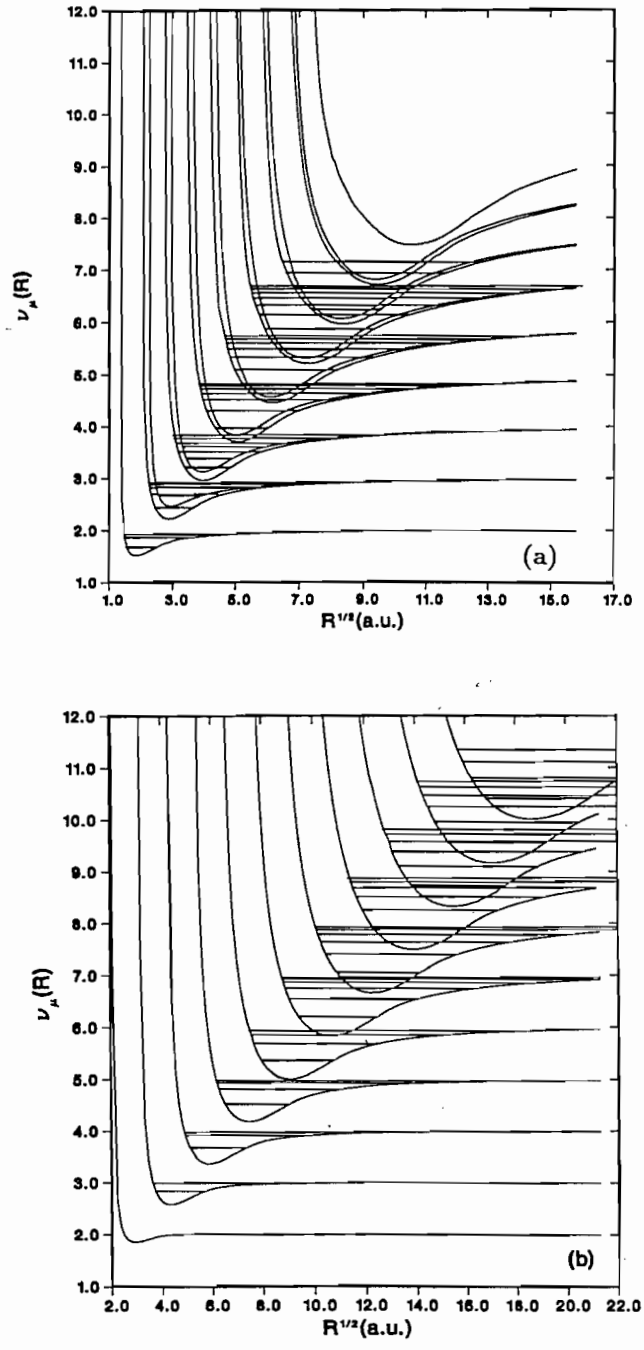


Fig. 4.2. The two lowest $A = +1$ diabatic potential curves converging to each asymptotic $N$th threshold of Fig. 4.1 are redrawn, and the calculated energy levels from the adiabatic potential curves are shown as horizontal lines. The upper graph is for $H^-$ and the lower one for He (from Sadeghpour [100]).

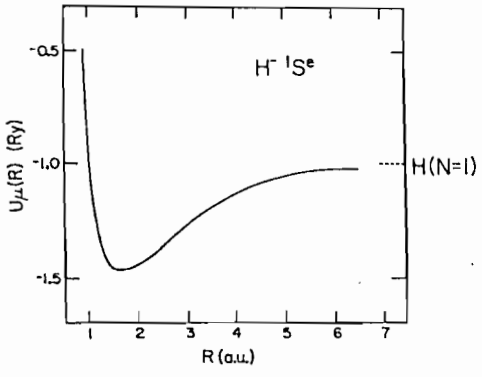


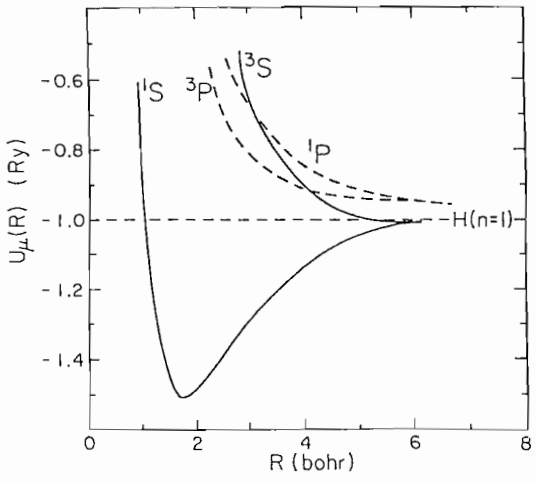


Fig. 4.3. Adiabatic hyperspherical potential curve for the ground $^1S^e$ channel of $H^-$. From Lin [96].

Fig. 4.4. The lowest adiabatic hyperspherical potential curves of different $L$, $S$ and $\pi$ of $H^-$ that converge to the ground state of the atomic hydrogen. From Lin [96].

Table 4.1
$^1S^e$ elastic phase shift for $e^- + H$ scattering. The one-channel and two-channel results are from Lin [96], the 3cc results are from the three-state close coupling calculation of Burke and Schey [106], and the variational results are from Schwartz [105]. From Lin [96].

| $k$ | 1 channel | 2 channel | 3cc | Variational |
|---|---|---|---|---|
| 0.1 | 2.513 | 2.521 | 2.491 | 2.553 |
| 0.2 | 1.983 | 2.023 | 1.974 | 2.067 |
| 0.3 | 1.568 | 1.659 | 1.596 | 1.696 |
| 0.4 | 1.242 | 1.380 | 1.302 | 1.415 |
| 0.5 | 0.989 | 1.142 | 1.092 | 1.202 |
| 0.6 | 0.784 | 0.928 | 0.93 | 1.041 |

The potential curve in Fig. 4.3 can support one bound state only. One can use this potential curve to find additional information such as the elastic scattering phase shift for $e^- + H(1s)$ collisions. These phase shifts have been calculated variationally by different methods. We compare in Table 4.1 the results from the one-channel and two-channel hyperspherical potential methods [96] with those from the variational method [105] and the close coupling method[106]. Note that at low energies the single channel hyperspherical method is actually more accurate than the results from the three-state (1s, 2s and 2p) close-coupling calculations. The fact that the phase shift approaches $\pi$ at zero energy, according to the Levinson theorem, implies that there is only one bound state supported by the potential curve of Fig. 4.3.

One advantage of calculating the ground state and the continuum states from a single hyperspherical potential curve is that the resulting wave functions are always orthogonal. The adiabatic hyperspherical wave functions thus obtained have been used to calculate the detachment cross sections in collisions

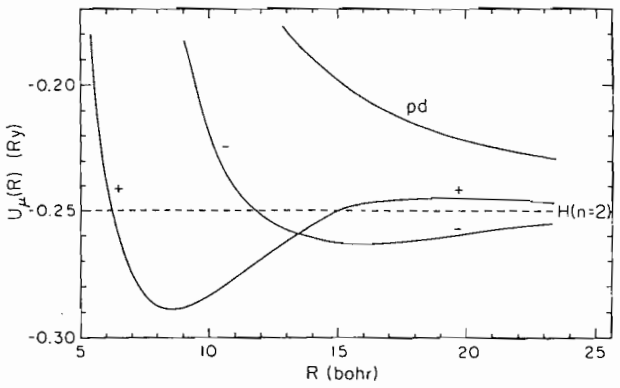


Fig. 4.5. The three $^1P^o$ potential curves of $H^-$ converging to the $N = 2$ limit of H. The + curve supports the shape resonance and the − curve supports the Feshbach resonance. From Lin [97].

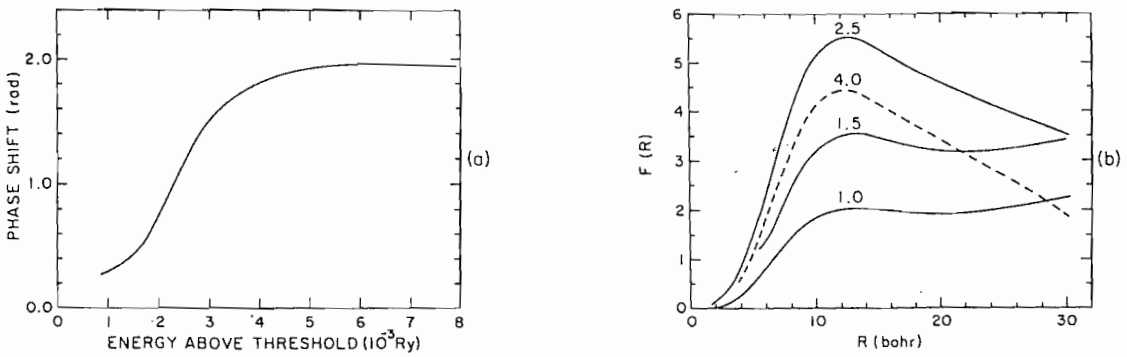


Fig. 4.6. (a) Variation of the phase shift versus electron energy above the threshold near the shape resonance. (b) Radial wave functions at energies near the resonance. The energies are given in units of $10^{-3}$ Ry. From Lin [97].

of $H^-$ with He and other rare gas atoms [107,108] within the Born approximation.

The lowest potential curves for other symmetries of the $H^-$ system are completely repulsive, as shown in Fig. 4.4. These curves are not expected to support any bound states [96].

*4.1.3.2. The low-lying doubly excited states.* We next show specific examples of the application of hyperspherical coordinates to the study of doubly excited states of $H^-$ lying near the $H(N = 2)$ limit. In Fig. 4.5 the three $^1P^o$ hyperspherical potential curves associated with the $H(N = 2)$ limit are shown[97]. The curves are labeled as +, − and pd, since the corresponding curves for the isoelectronic He system were thus named by Cooper, Fano and Pratt [109] originally.

With respect to the $H(N = 2)$ threshold, the + curve is rather attractive at small $R$, but becomes repulsive at large $R$. It turns out that this curve is not strong enough to support a bound state, but it does support a shape resonance at energies slightly above the $H(N = 2)$ threshold. The existence of such a shape resonance is conveniently illustrated in Fig. 4.6 where the upper figure shows that the calculated phase shift undergoes a rapid change with energy. In the lower figure the wave functions inside the potential barrier (which is at $R = 18$, see Fig. 4.5) are seen to change rapidly as the

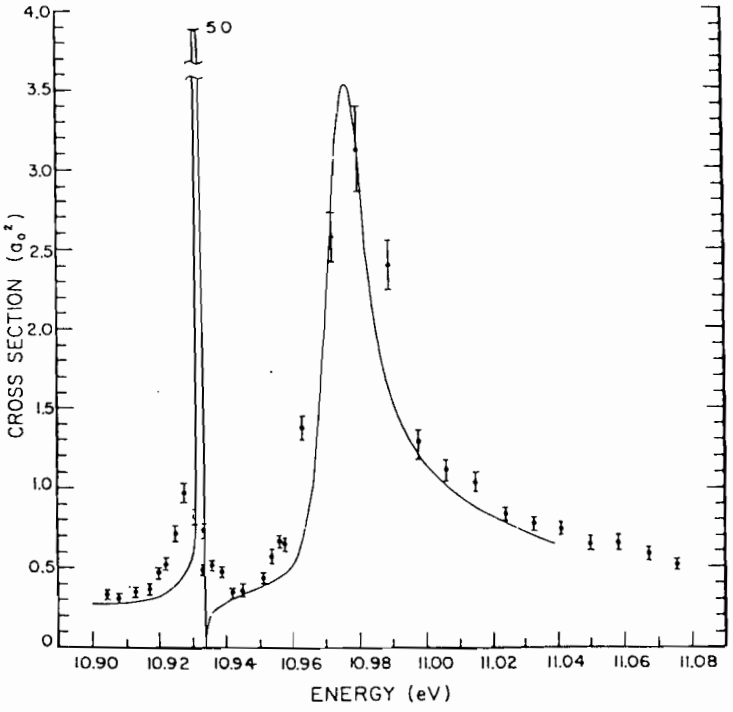


Fig. 4.7. Photodetachment cross sections of $H^-$ near the $N = 2$ threshold of H. The solid line is the result of calculations by Broad and Reinhardt [140]. From Bryant et al. [98].

total energy varies across the resonance position. The position and width of the shape resonance thus obtained are 32 meV (above the $N = 2$ threshold) and 28 meV, which are to be compared to the experimental results of 27 meV and 23 meV, respectively[98]. This again illustrates that a one-channel model within the hyperspherical approach already explains the major features of this resonance.

The $-$ potential curve in Fig. 4.5 is mostly repulsive at small $R$, but becomes attractive and behaves like $-3.77/R^2$ asymptotically. This dipole potential can support an infinite number of bound states, and the lowest one is calculated to be at 10.173 eV from the ground state of H [110] which is to be compared with the experimental result of 10.180 eV [98]. The higher states are all very close to the threshold and have not been observed experimentally. It is known that the energy levels of neighboring states in a dipole potential $V(r) = -b^2/r^2$ satisfy the relation $E_{n+1}/E_n = \exp(-2\pi/a)$ where $a^2 = b^2 - 1/4$ [58].

The potential curves in Fig. 4.5 can be used nicely to interpret the experimental results of the photodetachment of $H^-$ near the $N = 2$ threshold. In Fig. 4.7 we show the data of Bryant et al. [98] where the large shape resonance is associated with the $+$ curve and the narrow Feshbach resonance is associated with the $-$ curve of Fig. 4.5. The hyperradial wave function of the shape resonance, as seen in Fig. 4.6, has peak near $R = 12$ a.u. It would correspond to the "2s2p" configuration if the independent particle designation is used, yet its energy is higher than the Feshbach resonance which has the "2s3p–2p3s" designation. This illustrates that a state which is larger (in $R$) does not guarantee

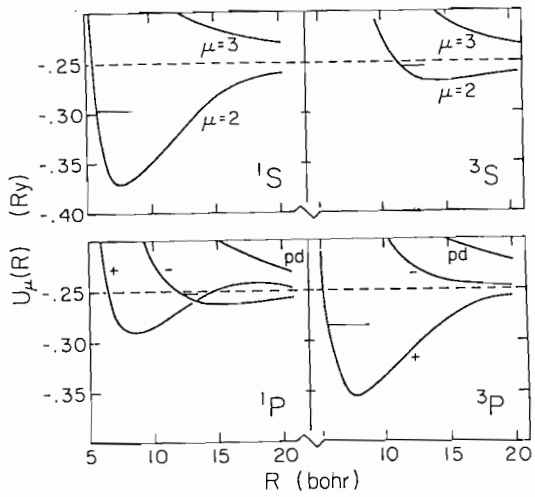


Fig. 4.8. Adiabatic hyperspherical potential energy curves of $H^-$ that converge to the $N = 2$ level of the atomic hydrogen. From Lin [110].

that it will have higher energy: electron correlation does provide a major factor in determining the energy levels too.

For comparison, we also show in Fig. 4.8 the potential curves of $H^-$ that are associated with the $H(N = 2)$ threshold for other symmetries. Only one potential curve in each symmetry has attractive well which can support bound states (they become autoionizing states when the nonadiabatic coupling with the lower curve is included).

## 4.2. *Classification of doubly excited states of atoms*

### 4.2.1. *Introduction*

The adiabatic approximation allows the separation of the hyperradial degree of freedom from other degrees of freedom. While the hyperradial wave function $F(R)$ gives the size of a particular state within a given channel $\mu$, the nature of electron correlation is implicitly contained in the channel wave function $\Phi_\mu(R;\Omega)$. One of the major challenges in the study of doubly excited states of atoms is the identification of approximate quantum numbers which are implicitly designated as $\mu$.

In Fig. 4.9 the adiabatic potential curves for doubly excited states of He lying below the $He^+(N = 3)$ limit are shown. The top row shows the curves for $^1S^e$, $^3P^o$ and $^1D^e$ and the bottom row for $^3S^e$, $^1P^o$ and $^3D^e$. Each potential curve is designated by a set of $(K,T)^A$ quantum numbers. In other words, the channel index $\mu = |(K,T)^A, N, L, S, \pi\rangle$, where $N = 3$ refers to the asymptotic limit of the $He^+$ ion, $L$ and $S$ are the usual total orbital and spin angular momentum quantum numbers, respectively, and $\pi$ is the parity.

### 4.2.2. *The K, T and A quantum numbers*

Before discussing these potential curves, it is essential to address the origin and the meaning of the $K$, $T$ and $A$ quantum numbers. They do not emerge directly from the calculations using hyperspherical coordinates and they are not needed from a purely computational point of view.

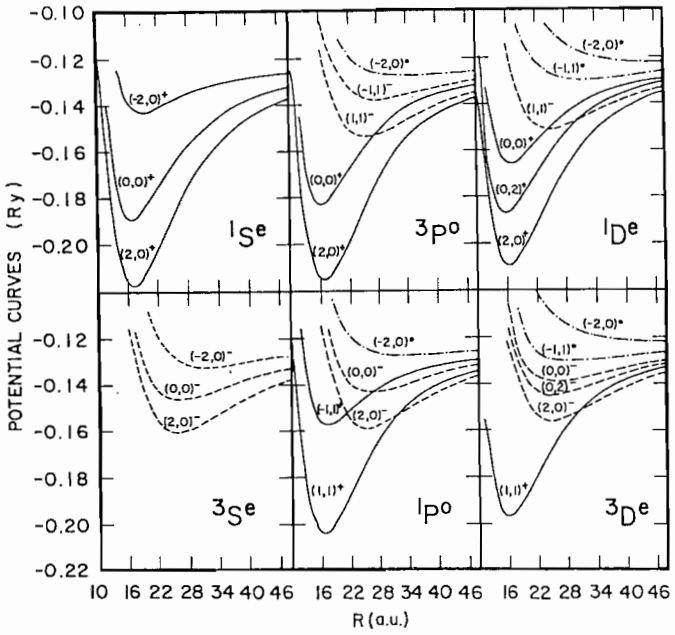


Fig. 4.9. Potential curves for all the $^{1,3}S^e$, $^{1,3}P^o$ and $^{1,3}D^e$ channels for He that converge to $He^+(N = 3)$. Curves are labeled in terms of $K$, $T$ and $A$ quantum numbers. Reduced units with $Z = 1$ are used. From Lin [51].

However, understanding the meaning of these approximate quantum numbers provides insight on the nature of electron correlation in doubly excited states.

It is obvious that at $R = 0$, the channel index $\mu$ can be identified with $l_1, l_2$ and m, the quantum numbers of the hyperspherical harmonics. However, these quantum numbers are not useful at finite R since the hyperspherical harmonics are not diagonal with respect to the Coulomb interaction. In the limit of large R where one electron is far away from the other, the system consists of an outer electron from an excited $He^+$ core in the $N$th excited state. The asymptotic potentials for each $N$ can be obtained by solving the channel equation (3.9) in the limit of $\alpha \to 0$ and $R \to \infty$. By including the diagonal $W_{\mu,\mu}$ term in the definition of the adiabatic potential, one can show [12,80] that each potential curve is given asymptotically by

$$U_\mu(R)_{R\to\infty} \to \frac{-Z^2}{2N^2} - \frac{(Z-1)}{R} + \frac{1}{2R^2}\langle\Phi_\mu|\boldsymbol{l}_2^2 + 2r_1\cos\theta_{12}|\Phi_\mu\rangle. \tag{4.1}$$

Since the zeroth-order wave function in the asymptotic region is $\phi_{Nl_1}(r_1)y_{l_1m_1l_2m_2}(\hat{r}_1, \hat{r}_2)$, where index 1 refers to the inner electron, 2 to the outer electron, and the two electrons are coupled to a total angular momentum L, the channel wave function in the asymptotic region is obtained by diagonalizing the operator $\boldsymbol{l}_2^2 + 2r_1\cos\theta_{12}$ in this basis set. The resulting asymptotic potential is

$$U_\mu(R) \to -\frac{Z^2}{2N^2} - \frac{(Z-1)}{R} + \frac{\beta}{2R^2}. \tag{4.2}$$

where $\beta$ is the permanent dipole moment. Thus the adiabatic hyperspherical approximation in the asymptotic region is identical to the dipole representation of Gailitis and Damburg [111].

The result in (4.2) does not provide a set of convenient quantum numbers to distinguish different channels that converge to the same limit. Such a set of approximate quantum numbers has been obtained by Herrick and Sinanoglu [99]. Starting with the product of hydrogenic basis functions, they constructed the doubly excited state functions (DESB) which are the irreducible representation of the SO(4) × SO(4) algebra. In this irreducible representation the DESB functions are given by

$$|Nn, KTL\pi\rangle = \sum_{ll'} |Nl, nl'; L\rangle D^{KTL\pi}_{Nl,nl'}; \tag{4.3}$$

where $|Nl, nl'; L\rangle$ is a product hydrogenic wave function coupled to total angular momentum $L$ and $D$ is proportional to a 9-$j$ symbol. It has been shown [99] that (4.3) gives a good first order approximation for intrashell doubly excited states. In essence, Eq. (4.3) shows that a doubly excited state wave function, to first order, can be represented as a linear combination of the degenerate basis functions in the $(N, n)$ manifold. By extending the principal quantum number $n$ of the outer electron to infinity, we note that (4.3) is an approximate representation of the channel function in the asymptotic region as well. Thus the quantum number $K$ and $T$ can be used to label the channel $\mu$, at least in the asymptotic region.

From the unitary transformation in (4.3) and the range of the 9-$j$ symbols in $D$, the ranges of $K$ and $T$ are determined by the following constraints:

$$T = 0, 1, 2, \ldots \min(L, N-1), \qquad K = N-1-T, N-3-T, \ldots -(N-1-T) \tag{4.4}$$

The algebraic approach gives the set of integers $K$ and $T$ for labeling doubly excited states. The physical interpretation of these quantum numbers and the validity of the DESB functions, however, do not emerge directly from this approach. Since the $K$ and $T$ quantum numbers are to describe the relative motion of the two electrons, their meanings are more conveniently extracted if the wave functions are expressed in the body-frame of the system.

### *4.2.3. Wave functions in the body-frame of reference*

Traditionally, atomic wave functions are expressed in the laboratory frame of reference. To enumerate the correlation properties of an excited atom, it is useful to disentangle the internal motion from the overall rotation of the system. To this end, one can expand the channel function $\Phi_i(R; \Omega)$ in reference to body-fixed frames. By choosing the interelectronic axis as the quantization axis, we expand

$$\Phi_\mu(R; \Omega) = \sum_{Q=0}^{L} \Phi^\mu_Q(R; \alpha, \theta_{12}) \bar{D}^L_{QM}(\omega), \tag{4.5}$$

where $\bar{D}$ is defined as in Eq.(2.30) and $\omega$ is the set of three Euler angles. For $L = 0$ , there is only one $Q = 0$ "rotational component". Under interchange of the two electrons, which corresponds to changing $\alpha$ to $\pi/2$-$\alpha$, the rotational component $\Phi_{Q=0}$ has a symmetry $(-1)^S$. Thus $\Phi_{Q=0}$ has even symmetry with respect to $\alpha = \pi/4$ for $^1S^e$ states and odd symmetry for $^3S^e$ states. For nonzero values of $L$, the summation in (4.5) is over the projection of $L$ onto the interelectronic axis. From the symmetry property of the $\bar{D}$ function, one can show that each rotational component has well-defined symmetry properties with respect to $\alpha = \pi/4$ and with respect to $\theta_{12} = \pi$ [66]

$$\Phi_Q(R;\alpha,\theta_{12}) = \pi(-1)^{S+Q}\Phi_Q(R;\pi/2-\alpha,\theta_{12}),$$
$$\Phi_Q(R;\alpha,2\pi-\theta_{12}) = (-1)^Q\Phi(R;\alpha,\theta_{12}). \tag{4.6}$$

It is clear that the present body-frame corresponds to the $\alpha$-set coordinates defined in Fig. 2.1 for the general Coulombic three-body systems. Recall that the $\alpha$-set coordinates are the molecular frame normally used to describe systems such as $H_2^+$. In the Born–Oppenheimer approximation, the projection of $L$ along the internuclear axis is chosen as a good quantum number, meaning that there is only a single $Q$ (to be called $T$) component in the summation (4.5). If this is also true for the doubly excited states of two-electron atoms, then $T$ can be used as a possible approximate quantum number. This interpretation differs from the original algebraic approach where $T$ is an exact quantum number of an approximate wave function. For doubly excited states, how purely $T$ can be treated as a good quantum number has been examined in a number of cases, as in Chen et al. [67] and Watanabe and Lin [66]. The original definition of the $K$ quantum number refers to the angle between the two electrons with respect to the nucleus. For each $N$, states with $K = N-1$ have the largest angle between the two electrons. To first order, the quantum number $K$ can be related to the bending vibrational quantum number $v = N-K-1$. This subject has been fully discussed elsewhere [4,49,53].

If $T$ is a good quantum number, then the doubly excited state wave function in the body-frame can be written as $\Phi_T(R;\alpha,\theta_{12})\ \tilde{D}^L_{TM}(\omega)$ and the internal wave function has the symmetry

$$A = \pi(-1)^{S+T} \quad \text{if} \quad K > L-N, \tag{4.7}$$

when $\alpha$ is changed to $\pi/2-\alpha$. Thus if $A=+1$, the wave function $\Phi_T(R;\alpha,\theta_{12})$ has an antinode at $\alpha=\pi/4$, and if $A=-1$, the wave function has a node at $\alpha=\pi/4$. The nodal structure of the wave function near $\alpha=\pi/4$ is crucial in determining the properties of doubly excited states. Note that the set of $K$ and $T$ depend on $N$ and $L$ [see Eq. (4.6)], but $A$ depends on $S$ for each given $K$, $T$ and $\pi$.

Not all doubly excited state wave functions can be approximated by a single $Q$ component when expanded in the body-frame. In this case, the different $Q$ components in Eq. (4.5) are of nearly equal weights and $T$ is to be treated as a label. For such states, $T$ enumerated from (4.4) is used as a label, and $A=0$ is assigned. In other words, for the $A=0$ states, the $K$ and $T$ are simply used as labels without their original meanings. The empirical rule for $A=0$ states are:

$$A = 0 \quad \text{if} \quad K \le L-N \tag{4.8}$$

*4.2.4. Potential curves*

We now return to the potential curves shown in Fig. 4.9 where each curve has been labeled by $\mu \equiv |(K,T)^A, N, L, S, \pi\rangle$. If correlation determines predominantly the energy of each channel, then the curves that have the same $K$, $T$ and $A$ are expected to have nearly identical potential curves. This is indeed the case as one can see from Fig. 4.9.

The assignment of $K$, $T$ and $A$ quantum numbers for the potential curves calculated proceeds as the following:

(1) The range of $K$ and $T$ for a given $N$, $L$ and $\pi$ can be obtained from Eq. (4.4).

(2) Order the asymptotic potential curves from the bottom starting with the largest $K$ value and then in order of decreasing $K$. If there is more than one $T$ for a given $K$, order from below starting with the smallest $T$.

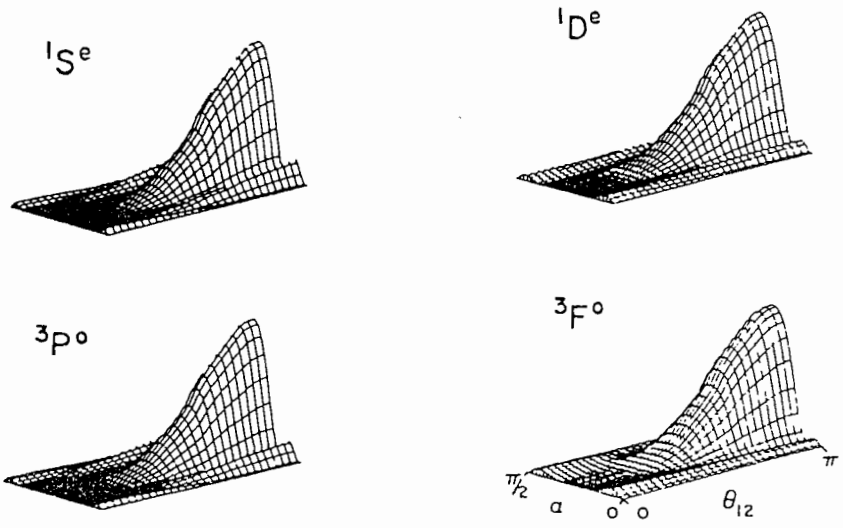


Fig. 4.10. Surface charge density plots for the $(2,0)_3^+$ channels of $^1S^e$, $^3P^o$, $^1D^e$ and $^3F^o$ of He at $R = 20$. From Lin [51].

(3) At small $R$, the lower or the more attractive curves belong to $A = +$ channels. Among the $+$ channels, the larger $K$ goes with the lower curve and for a given $K$, the lower $T$ with the lower curve. The same procedure then applies to the $A = -1$ curves and then to the $A = 0$ curves.

(4) Connect the curves which have identical $K$ and $T$ in the two regions. Only the $+$ and $-$ curves are allowed to cross.

The rule for assigning the $K$, $T$ and $A$ quantum numbers can be understood qualitatively once the nature of the correlation pattern associated with these quantum numbers is understood.

*4.2.5. Correlation pattern and surface charge density plots*

For two-electron systems, the correlation pattern can be "visualized" on the $(\alpha, \theta_{12})$ plane for each hyperspherical surface $R$ = constant if one averages over the rotational motion of the atom. From the calculated channel function in the laboratory frame, the surface charge density can be calculated (see appendix 1 of Lin [51] for the explicit expression). The results are shown in Fig. 4.10 for the $(2,0)^+$ channel for $N = 3$ at $R = 10$, for $^1S^e$, $^3P^o$, $^1D^e$ and $^3F^o$ symmetries. It is clear that the major features of the densities are essentially the same: in each channel the electron density has a peak at $\alpha = \pi/4$ and $\theta_{12} = \pi$. Thus the two electrons tend to stay on opposite sides of the nucleus and at about the same distance from it. This resembles the configuration of a linear triatomic ABA molecule or the bonding orbitals of $H_2^+$. In this respect, one may view the $^3P^o$, $^1D^e$ and $^3F^o$ states shown in Fig. 4.10 as the rotationally excited states, with $^1S^e$ being the ground state.

As another example, we show in Fig. 4.11 the surface charge density plots for the $(1,1)^+$ $^1P^o$, $^3D^e$ and $(1,1)^-$ $^3P^o$, $^1D^e$ channels for $N = 3$ at the values of R shown. The major difference between the $+$ and - is that the former has a maximum at $\alpha = \pi/4$ and the latter has a nodal line at $\alpha = \pi/4$. Note that in these examples, the $K$ and $T$ are identical and thus they have nearly identical $\theta_{12}$ dependence in the surface charge density distribution.

These examples clearly show the validity of the classification scheme. The quantum numbers are

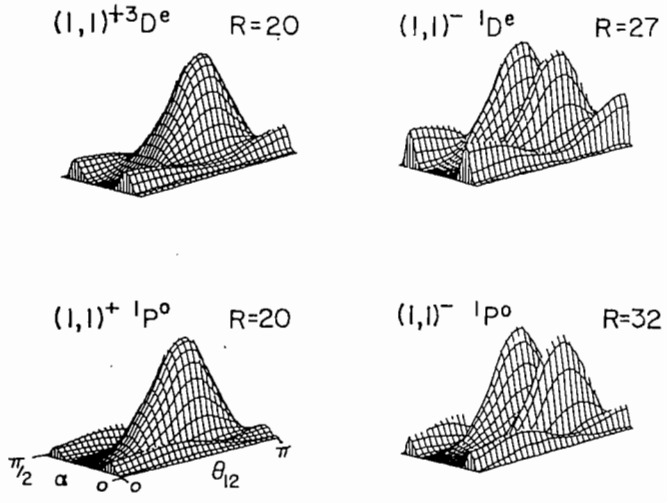


Fig. 4.11. Surface charge density plots for the $(1,1)_3^+$ channels of $^3D^e$ and $^1P^o$ and the $(1,1)_3^-$ channels of $^1D^e$ and $^1P^o$ of He at the values of $R$ shown. From Lin [51].

related directly to the way the two electrons are correlated. For more examples, the reader is referred to Lin [51].

*4.2.6. Supermultiplet structure in energy levels*

According to the adiabatic approximation, the energy levels within a given channel $\mu$ can be obtained by solving the hyperradial equation

$$\left(-\frac{d^2}{dR^2} + U_\mu(R) + W_{\mu\mu}(R) - 2E\right) F_\mu(R) = 0\,. \tag{4.9}$$

Because of the near-degeneracy for potential curves which have the same correlation quantum numbers, one expects that the energy levels calculated from (4.9) be nearly degenerate as well. An example was given earlier for $H^-$ in Fig. 1.1. As another illustration, in Fig. 4.12 we show the energy levels for the $(3,n)$ doubly excited states of He. The effective principal quantum numbers are plotted in the figure. There are a number of features that should be pointed out:

(a) Along each column the states have identical $(K,T)^A$ quantum numbers, and each group (for example, the group of states $^1S^e$, $^3P^o$, $^1D^e$, $^3F^o$) is ordered with increasing values of $L$. Thus, they resemble the rotor states of a molecule. This rotor series, in the case of He, repeats along the Rydberg series. For each fixed $\mu = |(K,T)^A, N, L, S, \pi\rangle$, successive levels follow the simple Rydberg series formula.

(b) For $T \neq 0$, there are two rotor series which are nearly degenerate. This is similar to the $\Lambda$-doubling in molecular spectroscopy.

(c) The rotor series is truncated. Unlike molecules where the number of rotor states is quite large, the number of rotor states for each $(K,T)^A$ is limited, which is a consequence of the shell structure of atoms. The deviations of properties of doubly excited states from those in molecules have been

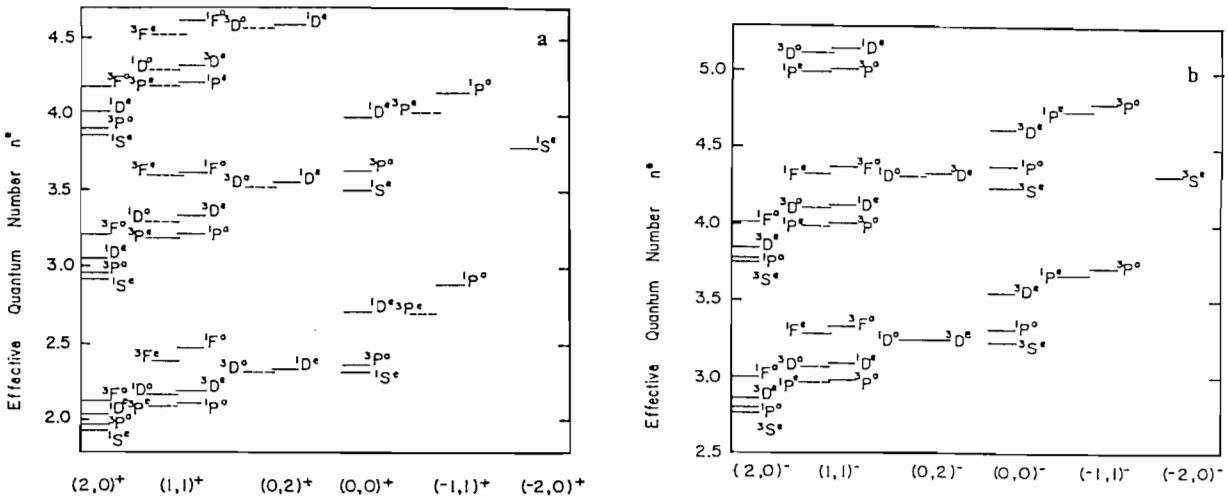


Fig. 4.12. Effective principal quantum number $n^*$ grouped according to the $(K,T)$ quantum numbers for doubly excited states of helium below the $He^+(N=3)$ limit for (a) $A=+1$ states, (b) $A=-1$ states. From Lin [51].

addressed in a number of articles and will not be elaborated here, see Watanabe and Lin [66] and Chen et al. [67].

(d) The energy level structure, as shown in the upper frame of Fig. 4.12 for $A=+1$, repeats for the $A=-1$ group. In fact, by arranging the energy levels as shown in Fig. 4.12, the pattern of supermultiplet structure repeats itself for $A=-1$ states.

It should be pointed out that not all the doubly excited states show this type of supermultiplet structure. For $A=0$ states, as shown, e.g., in Fig. 14 in Lin [51], that these states are similar to the singly excited states of He. They are not described by the molecular picture. On the other hand, the hyperspherical approach does incorporate these types of states as well since it is a direct numerical solution of the Schrödinger equation for the two-electron atom.

### *4.3. Application to $H^-$ in an external electric field*

In Section 4.1 we showed the application of the hyperspherical method in interpreting low-lying doubly excited states of $H^-$ and He. In Section 4.2 the hyperspherical method was used to illustrate the nature of electron correlation and the classification of doubly excited states. The energy eigenvalues of high-lying doubly excited states of helium and $H^-$ have been calculated by Matsuzawa and coworkers [82,83] using hyperspherical coordinates within the adiabatic approximation.

In this section, we show the application of hyperspherical method in interpreting experimental results of $H^-$ ions in a strong external electric field. We consider only the most recent experiment of Halka et al., [112] where the photodetachment of $H^-$ in an electric field with field strength from $F=0$ to $F=87$ kV/cm was carried out. The experimentalists measured the photodetachment cross section where the remaining H atom is simultaneously excited to the $N=4$ state. In Fig. 4.13 the cross sections at $F=0$ (the lower curve) and at $F=87$ kV/cm (the upper curve) are shown. At $F=0$, there is a clear threshold at 13.50 eV, and beyond which the photodetachment cross section increases quickly. At $F=87$ kV/cm, the spectra show two "surprising" distinct features:

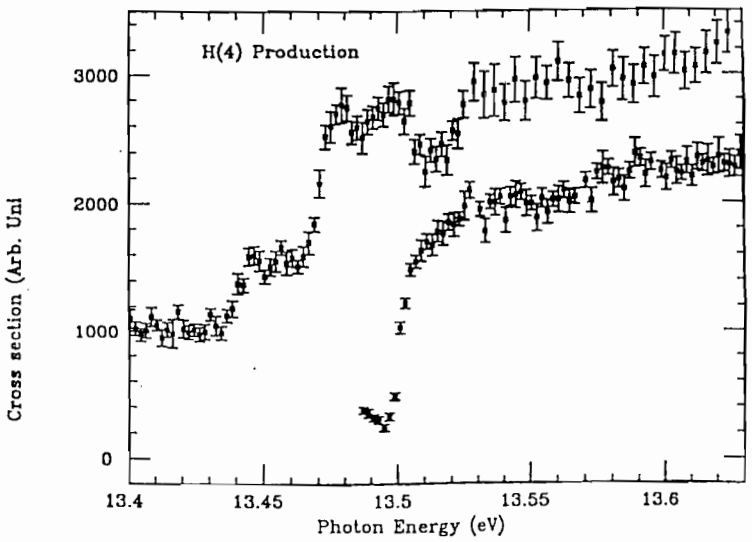


Fig. 4.13. Relative partial cross section of H($N = 4$) production versus photon energy near the $N = 4$ threshold for electric field strength $F = 0$ (lower curve) and $F = 87$ kV/cm (upper curve), measured by Halka et al. [112] Note that the curve for $F = 87$ kV/cm has been shifted upward for clarity. From Zhou and Lin [113].

(1) The threshold for photodetachment has been shifted downward to about 13.435 eV.

(2) There are two "dips" in the cross section, one at 13.465 eV which is below the zero-field detachment threshold and one at 13.513 eV which is above the zero-field detachment threshold.

The nature of these features of $H^-$ in an electric field is most surprising. However, it can be interpreted using the hyperspherical approach, as demonstrated recently by Zhou and Lin [113].

The Hamiltonian for an $H^-$ ion in an electric field can be written as

$$H = -\frac{1}{2}(\nabla_1^2 + \nabla_2^2) - \frac{1}{r_1} - \frac{1}{r_2} + \frac{1}{r_{12}} + F(z_1 + z_2) \tag{4.10}$$

where $z_i$ is the position of electron i, and z is the direction of the external electric field. The Hamiltonian (4.9) can be solved in hyperspherical coordinates in the adiabatic approximation.

When there is no external electric field, experimental evidence shows that only the $(2,1)_4^+$ $^1P^o$ states are populated in the photodetachment of $H^-$ below the $N = 4$ threshold. In an external electric field, the spherical symmetry of the ion is broken; therefore $L$ and $\pi$ are no longer good quantum numbers, but $S$ and the projection $M$ of $L$ along the $z$-axis still are. In solving (4.9), one first solves the Hamiltonian without the electric field term for each $L$, $S$ and $\pi$. The channel functions which are expected to interact strongly with the $(2,1)^+$ and $(3,0)^-$ $^1P^o$ states in an electric field are retained. The corresponding channel functions are then used as the new basis functions to diagonalize $F(z_1 + z_2)$, from which new field-dependent adiabatic potential curves are obtained.

In Fig. 4.14a we show a number of potential curves for $F = 0$. The $(2,1)^+$ and $(3,0)^-$ $^1P^o$ curves are shown as solid lines. Other curves are the $(3,0)^+$ for $^1S^e$, $^1D^e$, $^1G^e$, the $(2,1)^+$ for $^1F^o$ and $^1H^o$ and the $(3,0)^-$ $^1F^o$. The pairs of + and − curves are shown as diabatic states. In an external electric field, the "rediagonalization" gives a set of new potential curves, as shown in Fig. 4.14b. At small $R$, the effect of the electric field is small and the potentials are essentially the same as the $F = 0$ case.

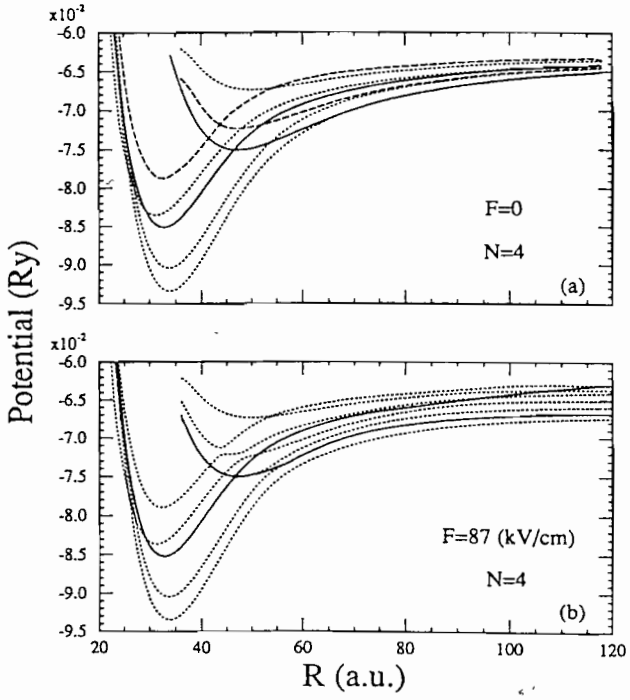


Fig. 4.14. Hyperspherical potential $U_\mu$ of $H^-$ as function of hyperradius, for the $N = 4$ manifold: (a) for $F = 0$; (b) for $F = 87$ kV/cm. The two darker curves correspond to the dominant + and − $^1P^o$ curves in the zero-field limit. From Zhou and Lin [113].

At large $R$, the electric field modifies the potential curves. In Fig. 4.15 we show the two + and − curves for $^1P^o$ for $F = 0$ (solid curves) and for $F = 87$ kV/cm (dashed curves). The new potential curves in the electric field serve to explain the experimental results shown in Fig. 4.13.

One of the main features of the curves at $F = 87$ kV/cm is that the lower curve (the − curve) is pushed downward at large $R$ and there is a maximum which is below the zero-field H($N = 4$) threshold. The top of the potential barrier becomes the new threshold for photodetachment and thus the threshold shift is the energy difference between the top of the potential from the zero-field H($N = 4$) threshold. The calculated shift is 57 meV which is in good agreement with the experimental value of $60 \pm 5$ meV. Similar agreement has been found at different electric field strengths[113].

Another interesting feature in Fig. 4.15 is that the + curve is shifted upward at small $R$, reaching a maximum at $R \cong 125$ before it decreases monotonically with increasing $R$. This + potential curve predicts the existence of several window resonances, the second one is at 13.465 eV which is below the zero-field threshold and the third one is at 13.511 eV which is above the zero-field threshold. These two energies obtained from the adiabatic potential curve are to be compared to the experimental results of 13.44 and $13.513 \pm 0.001$ eV, respectively.

The interpretation of the two new resonances is the following. In the field-free limit these two resonances belong to the $(2,1)^+$ $^1P^o$ channel. Since they lie below the H($N = 4$) threshold, they can decay only to the H($N = 3$) or lower thresholds. In the presence of an electric field, the + curve is shifted upward, thus their resonance energy positions are shifted slightly upward. The same

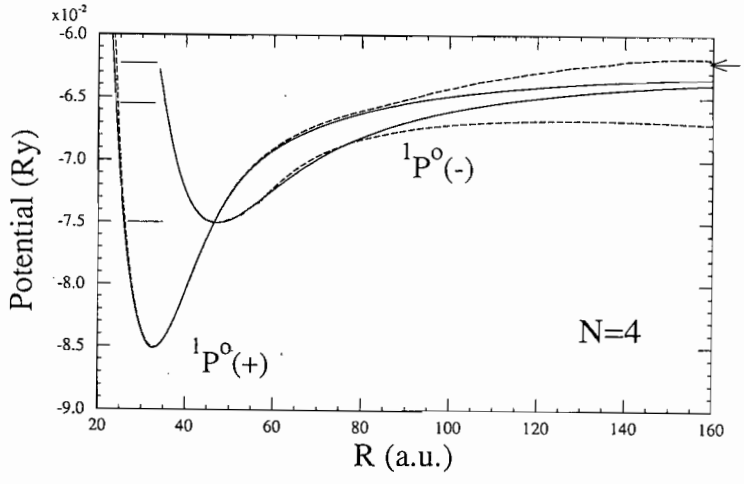


Fig. 4.15. Comparison between the $^1P^o$ diabatic potentials of $H^-$ in $F = 0$ (solid lines) and $F = 87$ kV/cm (dashed lines), for the $N = 4$ manifold. The arrow on the right indicates the position of the zero-field threshold. The energy positions of the three lowest resonance states in the + potential at $F = 87$ kV/cm are shown by horizontal bars. From Zhou and Lin [113].

electric field shifts the − curve downward. However, the residual weak coupling between the + and − channels, especially near the crossing region, allows the resonances in the + channel to decay through the − channel. Since the new threshold for the − channel is shifted to a value below the zero-field $H(N = 4)$ threshold by the electric field, this allows the + resonances to be observed in the $H(N = 4)$ channel as seen in the experiment.

This example serves to illustrate that hyperspherical potential curves, even in the presence of an electric field, can be used to explain, at least semiquantitatively, experimental results which are rather intriguing at first sight. In fact, the hyperspherical approach as discussed above provides the only interpretation of the experiment of Halka et al. The interplay of the electric field on the motion of individual electrons and the correlated motion between them can result in spectral features which are difficult to entangle. The hyperspherical potential curves are very useful in unraveling the nature of these features.

## 5. Applications of hyperspherical methods to Coulomb three-body systems in the adiabatic approximation

In this section, results for Coulomb three-body systems calculated using mass-weighted hyperspherical methods within the adiabatic approximation are illustrated. The qualitative properties and their dependence on the masses of the system are examined. In 5.1 systems where two of the particles are identical are first addressed, and in 5.2 systems where all three particles are different are addressed.

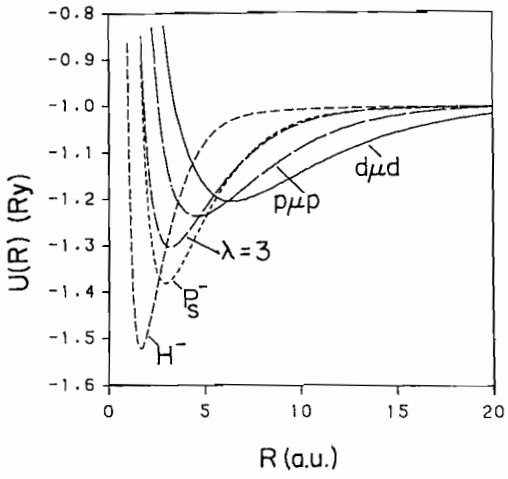


Fig. 5.1. Hyperspherical potential curves versus the mass ratio $\lambda$ for the Coulombic three-body systems ABA consisting of two identical particles. The curves shown are for $^1S^e$ symmetry which converge to the $N = 1$ hydrogenic dissociation limit. From Chen and Lin [48].

## 5.1. The ABA systems

### 5.1.1. The ground state and low-lying states

For a three-body system, ABA, where two of the particles are identical, it is known that there exists at least one stable bound state[46]. Define $\lambda = m_A/m_B$ and set the mass of the lighter particle to be unity. In the dissociation limit the asymptotic energies of the systems are given by $-\mu_{AB}/2N^2$ where $\mu_{AB}$ is the reduced mass of particles A and B, and N is the hydrogenic principal quantum number. Consider $L = 0$ and $S = 0$, where $L$ is the total orbital angular momentum quantum number and $S$ is the total spin of the two identical particles. In this designation, the spin of particle B is not included in the same convention as in atoms. The adiabatic potential curves for such ABA systems have been studied by Chen and Lin [48] and the properties of the channel functions have been studied by Liu et al. [114].

In Fig. 5.1 the lowest adiabatic potential curves calculated for $L = 0$, $S = 0$ and even parity are shown for a number of ABA systems. Because the hyperspherical radius is mass-weighted, the range of the hyperradius is more extended for large $\lambda$. The potential curves have been normalized such that each curve approaches $-1.0$ Ry in the asymptotic limit. It is clear that each curve has an attractive well which can support at least one bound state. The ground state energy for each system can be calculated by solving the one-dimensional hyperradial equation (the result should be the upper bound for each system). As $\lambda$ increases, the potential well becomes broader and more than one bound states can exist. It is known that there is only one bound state for $H^-$, $Ps^-$ and $p\mu p$ , and that there are two bound states for $d\mu d$. For even larger $\lambda$, such as $H_2^+$, calculation within the Born–Oppenheimer(BO) approximation for this potential curve (called the $1s\sigma$ curve) shows that there are 18 vibrational states for the $L = 0$ curve.

We next consider states that have nonzero $L$. In Fig. 5.2 the lowest adiabatic potential curves for the same systems but for $^3P^o$ symmetry are displayed. These curves have the asymptotic form

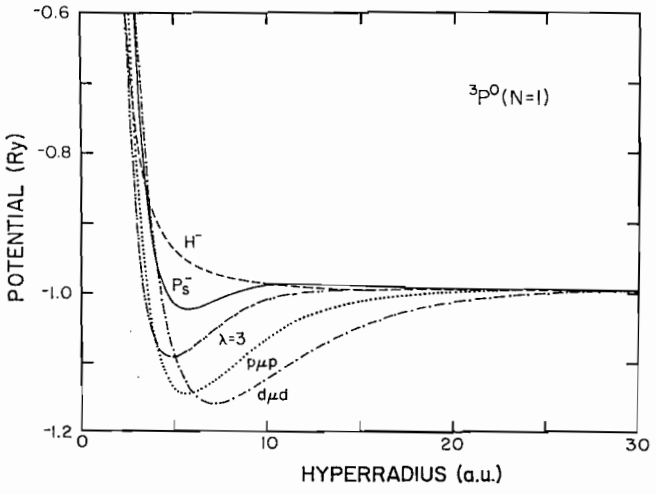


Fig. 5.2. Hyperspherical potential curves versus the mass ratio $\lambda$ for the Coulombic three-body systems ABA consisting of two identical particles. The curves shown are for $^3P^o$ symmetry which converge to the $N = 1$ hydrogenic dissociation limit. From Chen and Lin [48].

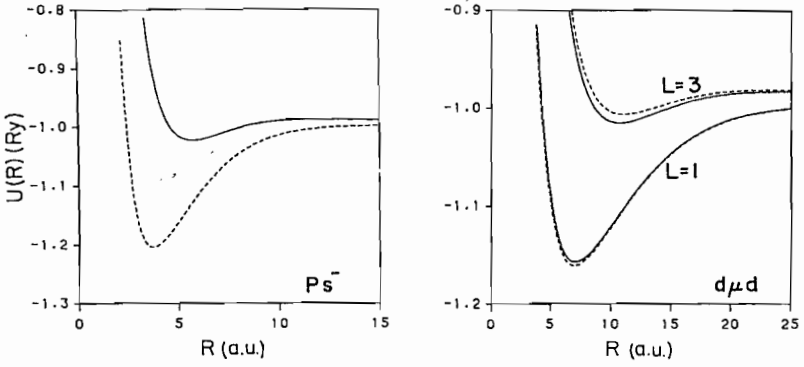


Fig. 5.3. Validity of the rotor structure for states below the $N = 1$ hydrogenic threshold in the dissociation limit. The solid curves are obtained from actually solving the adiabatic equation, and the dashed curves are obtained by adding the rotational kinetic energy to those calculated for $L = 0$. If the rotor structure is valid, the pair of curves should coincide. For $Ps^-$, the two curves shown are for $L = 1$. From Chen and Lin [48].

$-1.0 + 2/R^2$ (in Ry) at large $R$. The curve is fully repulsive for the whole range of $R$ in $H^-$, but becomes increasingly attractive with increasing $\lambda$. For p$\mu$p and d$\mu$d, the curve is attractive enough to support one and two bound states, respectively (see Table 6.6). For $H_2^+$, it is estimated that there are 18 bound states within the BO approximation. Both Figs. 5.1 and 5.2 illustrate that the potential curves become more attractive as $\lambda$ increases. In fact, within the BO approximation, the potential curves in Fig. 5.2 are simply obtained by adding the centrifugal potential energy $2/R^2$ to the corresponding ones in Fig. 5.1. In other words, a good measure of the validity of the BO approximation is to see how well the potential curves calculated within the adiabatic hyperspherical approximation is reproduced by adding $L(L+1)/R^2$ to the corresponding curves in Fig. 5.1. Such a comparison is shown in Fig. 5.3. On the left, the calculated $L = 1$ curve for $Ps^-$ (solid line) is

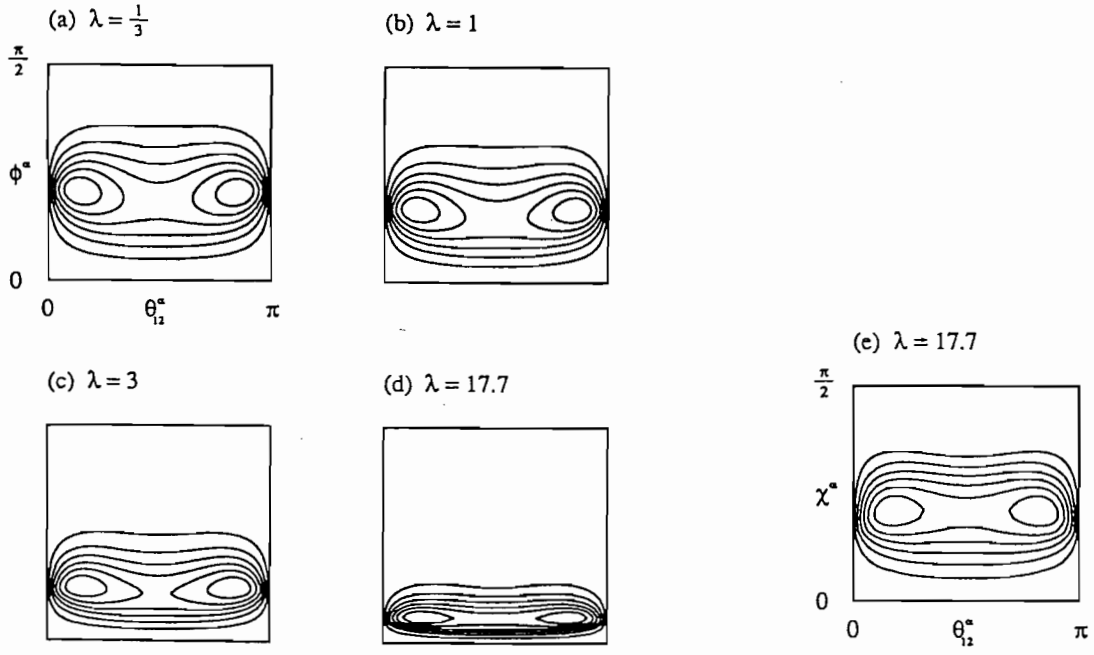


Fig. 5.4. Density distribution for the lowest $^1S^e$ states for various $\lambda$'s as plotted in the $\alpha$-set coordinates. All the plots show no nodal lines. The frame in (e) is shown for the $(\chi, \theta_{12})$ plane. From Liu et al. [114].

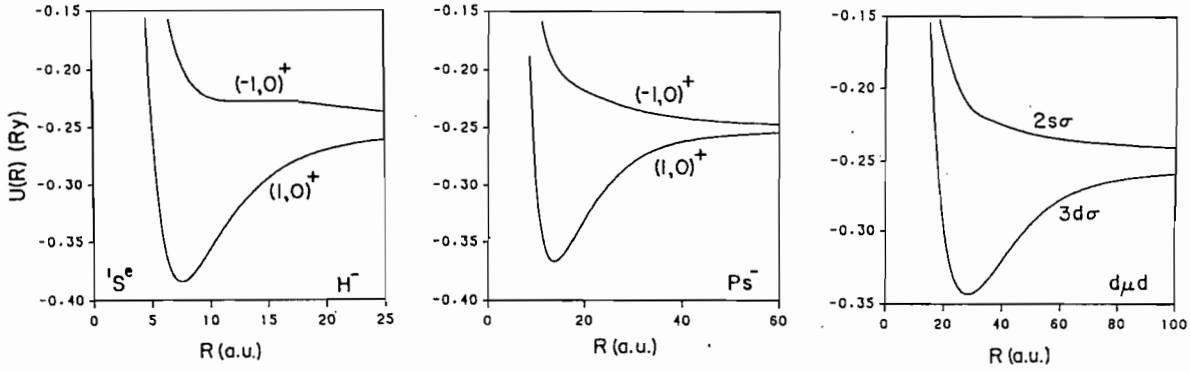


Fig. 5.5. $^1S^e$ potential curves that converge to the $N = 2$ threshold of the hydrogenic limit for the three systems shown. The curves are labeled using $(K, T, A)$ quantum numbers for $H^-$ and $Ps^-$ and molecular quantum numbers for $H_2^+$. The labelling also establishes the relation between these quantum numbers. From Chen and Lin [48].

shown to be poorly represented by such a "rotational" excitation model (the dashed lines). On the other hand, for the d$\mu$d system the curves in Fig. 5.3 show that the hyperspherical potential curve up to $L = 3$ is still fairly well represented as the rotational excitation of the $L = 0$ curve. This is simply an illustration that the system becomes more "molecular" as $\lambda$ increases.

The smooth evolution of potential curves as $\lambda$ is increased is not surprising. An alternative way of illustrating the similarity among the ABA systems with different $\lambda$ is to show the adiabatic channel functions. As an example, in Fig. 5.4 the density distributions for the lowest $^1S^e$ channels at values

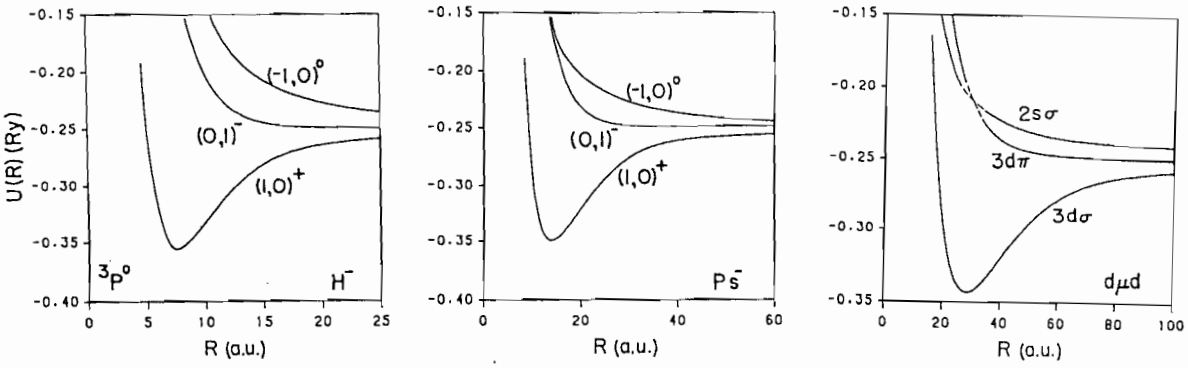


Fig. 5.6. $^3P^o$ potential curves that converge to the $N = 2$ thresold of the hydrogenic limit for the three systems shown. The curves are labeled using $(K, T, A)$ quantum numbers for $H^-$ and $Ps^-$ and molecular quantum numbers for $H_2^+$. The labeling also establishes the relation between these quantum numbers. From Chen and Lin [48].

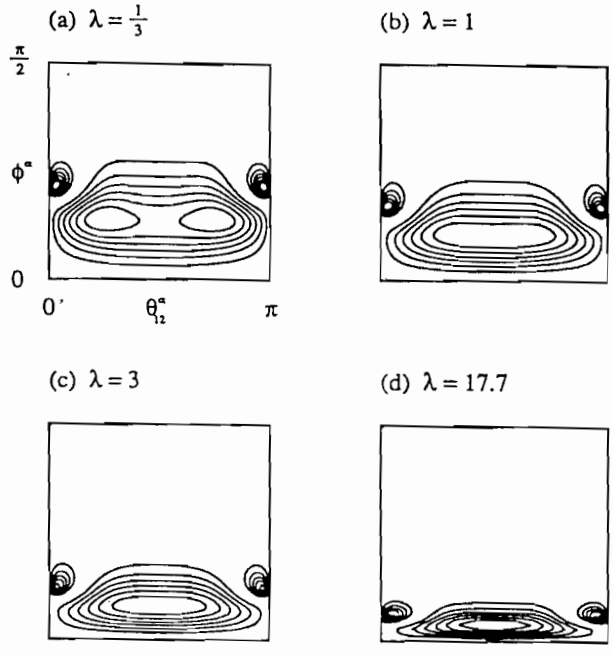


Fig. 5.7. The density plots for the second $^1S^e$ channel for various $\lambda$'s. The distributions correspond to particle B staying near the midpoint connecting the two identical particles. From Liu et al. [114].

of $R$ where the potential curve is near its minimum are shown. The density plots are displayed in the $\alpha$-set coordinates where the potential surfaces have been shown to be rather similar (see Fig. 3.5) except that the singularity points are shifted toward smaller $\phi$ as $\lambda$ is increased. In Fig. 5.4 we note that the density functions are essentially identical except that the plots are "squeezed" as $\lambda$ increases. This "squeezing" is a consequence of using mass-weighted hyperspherical coordinates. If we define an angle $\chi$ where $\tan\chi = \rho_2/\rho_1$ ($\rho_1$ and $\rho_2$ are the two vectors in the $\alpha$-set coordinates) and plot the density function in $(\chi, \theta)$ coordinates, the resulting density functions for $\lambda = 17.7$, as shown in the

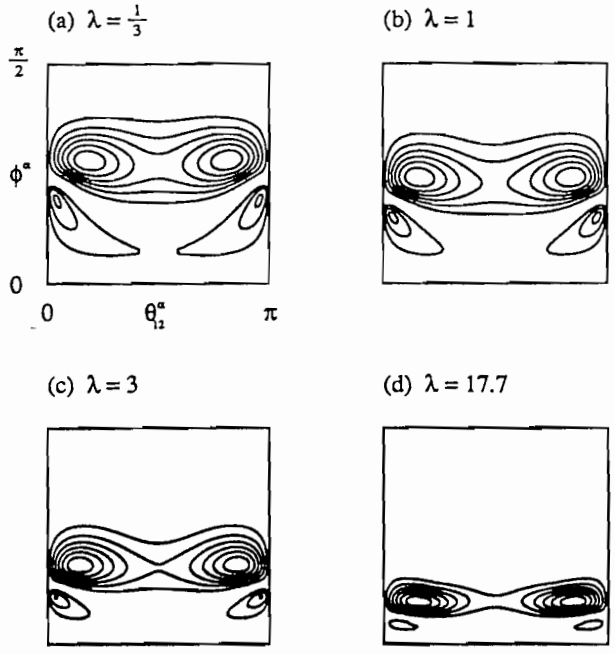


Fig. 5.8. The density plots for the third $^1S^e$ channel for various $\lambda$'s. The distributions correspond to particle B staying close to one of the two identical particles. From Liu et al. [114].

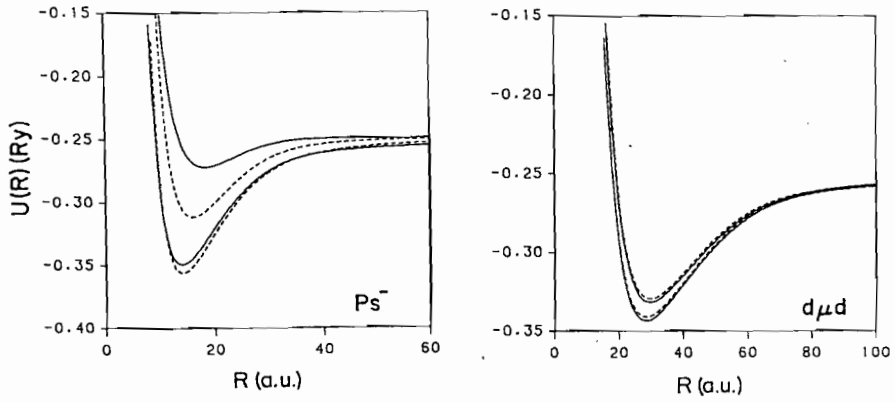


Fig. 5.9. Validity of the rotor structure for states below the $N = 2$ hydrogenic threshold in the dissociation limit. The solid curves are obtained from actually solving the hyperradial equation, and the dashed curves are obtained by adding the rotational kinetic energy to those calculated for $L = 0$. If the rotor structure is valid, the pair of curves should coincide. The lower pair is for $L = 1$.and the upper pair is for $L = 3$. From Chen and Lin [48].

lower part of Fig. 5.4, are very similar to those for $\lambda = 1/3$ or 1. This similarity in internal structure permits one to assign a single set of internal quantum numbers to describe all ABA systems.

We mention that the density plots for all the $^3P^o$ curves shown in Fig. 5.2 are expected to be similar to those shown in Fig. 5.4. Thus the same set of internal quantum numbers can be used to describe these states except that they are rotationally excited. In fact, a whole sequence of rotational excited

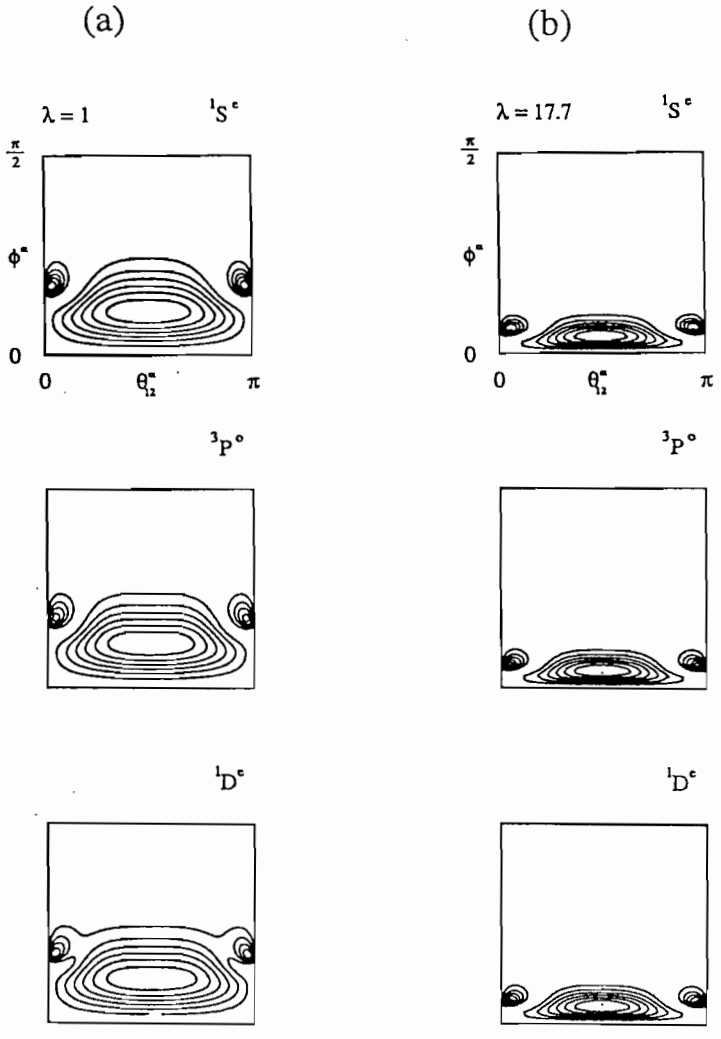


Fig. 5.10. Density plots for the second channel for the $^1S^e$, $^3P^o$ and $^1D^e$ symmetries for the $e^-e^+e^-$ (left) and the $d^+\mu^-d^+$ (right) systems. From Liu et al. [114].

states can be expected; they are $^1S^e$, $^3P^o$, $^1D^e$, $^3F^o$, $^1G^e$, ... As $L$ increases the distortion of the density distributions becomes large and the states cannot be approximated simply as the rotationally excited states. We mention that the sequence discussed here is similar to the rotor series associated with the $1s\sigma$ state of $H_2^+$.

The density plots shown in Fig. 5.4 are symmetric with respect to $\theta = \pi/2$, or with respect to the interchange of the two identical particles. For states which are antisymmetric with respect to $\theta = \pi/2$, we have the corresponding sequence $^3S^e$, $^1P^o$, $^3D^e$, $^1F^o$, $^3G^e$, ... This sequence is identified with the rotor series of the $2p\sigma$ state in $H_2^+$.

These two examples show that there is a one-to-one correspondence between the states in $H_2^+$ with

Table 5.1
The singularities of the potential surface for different masses of the Coulombic three-body systems as viewed in the $\alpha$-set coordinates. The singularities of the potential valleys are located at $(\phi^\alpha, \theta^\alpha) = (\phi_1, \pi)$ and $(\phi_2, 0)$. In the table, $m_C = 1$. The angles $\chi^\alpha$ for the singularities are also shown.

| System(ABC) | $m_A$ | $m_B$ | $\phi_1$ | $\phi_2$ | $\chi_1$ | $\chi_2$ |
|---|---|---|---|---|---|---|
| tt$\mu$ | 26.58 | 26.58 | 7.74° | 7.74° | 26.57° | 26.57° |
| dt$\mu$ | 26.58 | 17.75 | 6.80° | 10.71° | 21.14° | 31.52° |
| pt$\mu$ | 26.58 | 8.88 | 5.47° | 15.99° | 14.06° | 36.86° |
| $x$t$\mu$ | 26.58 | 3.00 | 3.48° | 28.29° | 5.79° | 41.94° |
| t$\mu^+\mu^-$ | 26.58 | 1.00 | 2.08° | 43.96° | 2.08° | 43.94° |

any states in the Coulombic ABA systems, at least qualitatively. The internal nodal structures for all these systems are all very similar, and this is the underlying reason why a single set of approximate quantum numbers can be used to describe these systems.

### *5.1.2. Doubly excited states*

We next consider states of ABA Coulomb three-body systems which lie below the excited states of AB, i.e., those states which correspond to doubly excited states in $H^-$ or those states associated with the excited electronic states in $H_2^+$. In Fig. 5.5 we show the two $^1S^e$ potential curves that converge to the $N = 2$ "hydrogenic" limit of each system for $H^-$, $Ps^-$ and d$\mu$d. The curves are labelled using $(K,T)^A$ for the first two systems and molecular orbital (MO) quantum numbers for d$\mu$d. The similarity in the curves for these systems are obvious and the labeling also indicates the one-to-one correspondence between the two sets of quantum numbers.

Similarly, the three $^3P^o$ potential curves that converge to the $N = 2$ limit for $H^-$, $Ps^-$ and d$\mu$d are shown in Fig. 5.6. The potential curves are again similar except for the last where the 3d$\pi$ and 2s$\sigma$ curves are allowed to cross as in $H_2^+$, but not in the other two systems. This difference originates from the fact that in the MO approach the projection of the orbital angular momentum quantum number along the internuclear axis is treated as a good quantum number, but such a restriction is not important for the other two systems.

The density plots associated with the lower potential curves of Fig. 5.5 but for $\lambda = 1/3, 1, 3$ and 17.7 are displayed in Fig. 5.7 using the $\alpha$-set coordinates. The density plots are symmetric with respect to $\theta = \pi/2$, but with a nodal line running around the singular points of the potential surface. In comparison with Fig. 5.4 the density plots in Fig. 5.7 exhibit one nodal line, thus they are "vibrationally" excited. It is not a pure excitation in either $\phi$ or $\theta$ since the nodal lines are not straight lines.

The density plots associated with the upper potential curves of Fig. 5.5 are displayed in Fig. 5.8. Note that the nodal line lies on the small-$\phi$ side. In comparison with Fig. 5.7, this implies that states associated with the lower curves of Fig. 5.5 have more density for small $\rho_1$, i.e., particle B is closer to the midpoint of the two identical particles – a bonding geometry. On the other hand, states associated with the upper curves of Fig. 5.5 have a node for small $\rho_1$ and particle B is not "shared" by the two identical particles, but is close to one or the other.

The hyperspherical approach calculates the potential curves and channel functions (or density distributions) directly by solving the Schrödinger equation. From the potential curves, one can

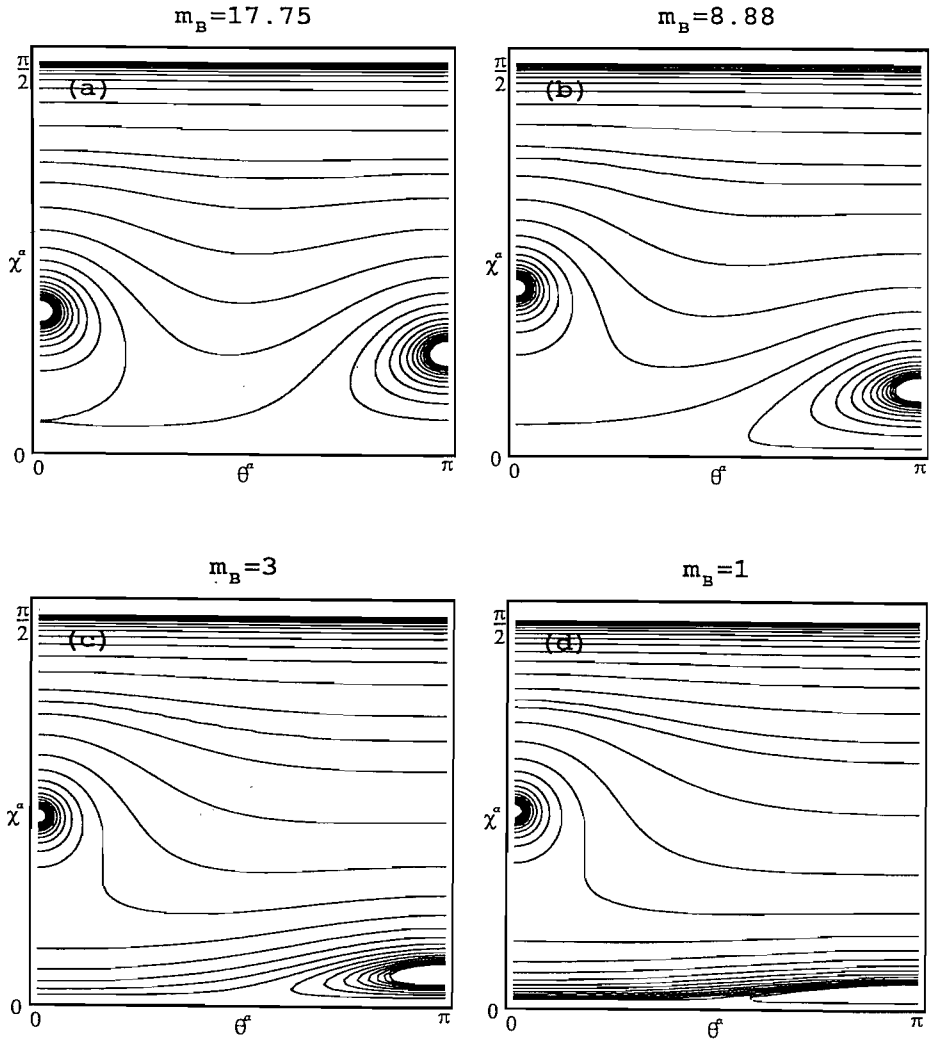


Fig. 5.11. Contour plots of the potential surface for $A^+B^+C^-$ systems on the $\alpha$-set coordinates. The values of $m_A = 26.58$, $m_C = 1$ and $m_B$ is as shown. The singularities of the potential valleys at the $\chi$ angles are shown in Table 5.1. From Zhou et al. [115].

examine the validity of the MO model for describing ABA three-body systems. If the MO picture is applicable, the potential curves for the higher L's can be obtained by adding $L(L+1)/R^2$ to the corresponding $L = 0$ curve. According to the shell model, it is known that the rotor series is truncated. For example, for $(K,T)^A = (1,0)^+$, the rotor series is limited to $L = 0, 1, 2$. In Fig. 5.9 we show the potential curves actually calculated and compare them with those obtained by adding $L(L+1)/R^2$ to the corresponding $L = 0$ curve. For $Ps^-$, the two sets of curves are very close for $L = 1$, but not for $L = 3$, thus indicating that the rotational truncation for $Ps^-$ is similar to that for $H^-$. For $d\mu d$, which is more like a $H_2^+$ molecule, there is no rotational truncation and the two sets of curves agree

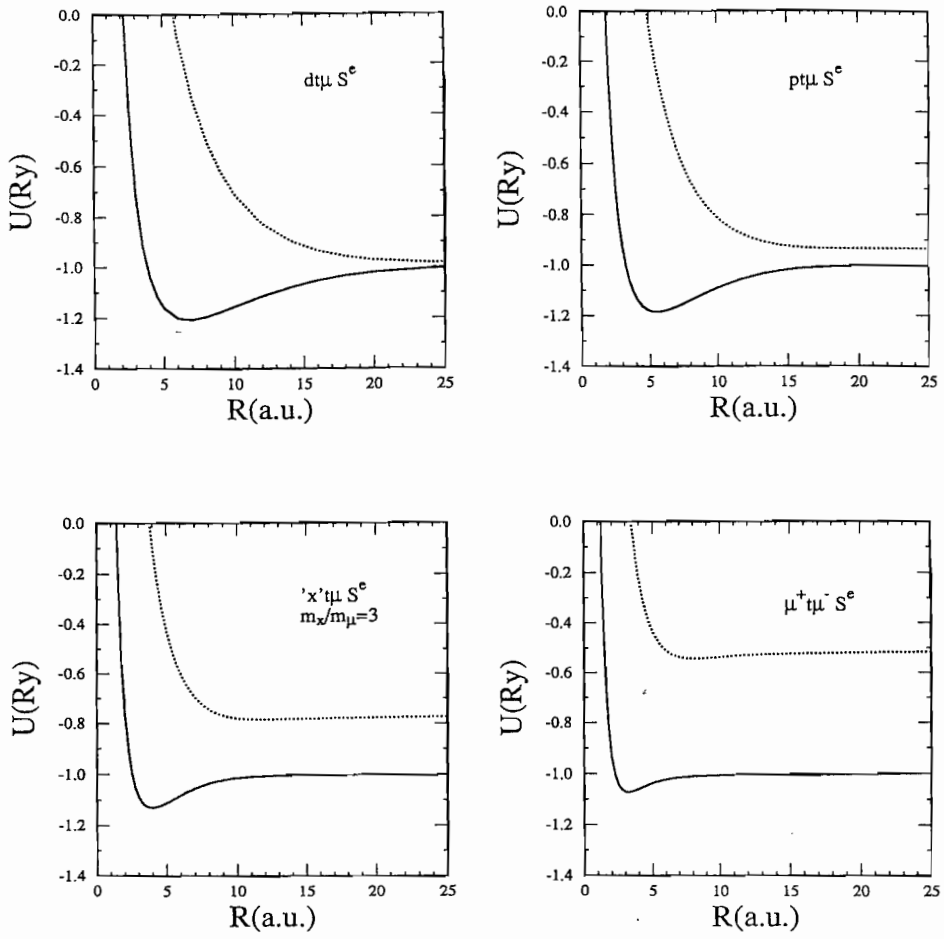


Fig. 5.12. The adiabatic potential curves for the four systems shown for $L = 0$. The energy levels have been normalized so that the lowest curve approaches $-1.0$ Ry in the asymptotic limit. From Zhou et al. [115].

quite well for both $L = 1$ and $L = 3$.

Another method of "observing" the effect of rotational motion is to compare the density plots for different $L$'s for the same set of $(K, T)$ quantum numbers. In Fig. 5.10 we show the contour plots of the densities for $^1S^e$, $^3P^o$ and $^1D^e$ symmetries for $Ps^-$ and d$\mu$d. For $Ps^-$ we begin to see small deviations for $L = 2$ from those shown for $L = 0$, and 1, while for d$\mu$d there is no discernible difference in the three frames.

We summarize this section by emphasizing that the hyperspherical method allows for a unified treatment of the general Coulombic ABA systems where two of the particles are identical. There is a one-to-one correspondence between the molecular quantum numbers for large $\lambda$ and the $(K, T)^A$ quantum numbers for labeling states for small $\lambda$. On the other hand, the $(K, T)^A$ quantum numbers do provide additional constraints [see Eqs. (4.4) and (4.8)] which reflect the consequence of the effect of the shell model for atoms. The latter does not come out from the molecular model.

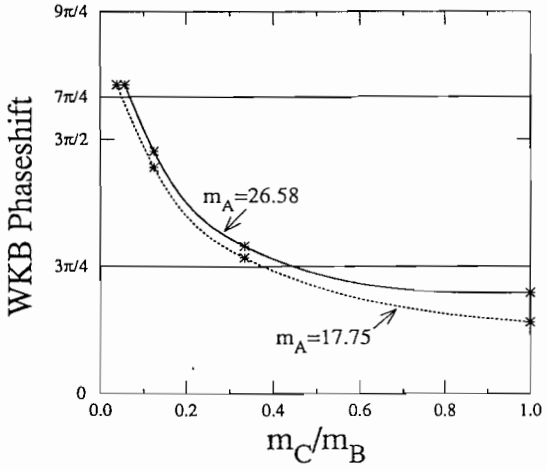


Fig. 5.13. The WKB phase shift as calculated from Eq. (5.1). The two horizontal lines separate the three regions where: (a) no bound states (the lowest region), (b) one bound state and (c) two bound states. The mass of particle A is shown and that of particle C is one. From Zhou et al. [115].

### 5.2. *The ABC systems*

Consider three-body systems where all three particles are different and each carries one unit of charge [115]. We choose the convention that particles A and B have the same sign of charge and that $m_A \geq m_B$. In the dissociation limit, particles B and C can form "hydrogenic" bound states, with energies given by $-\mu_{BC}/2n^2$ in atomic units, where $\mu_{BC}$ is the reduced mass of particles B and C and $n$ is the principal quantum number. Similar bound states can be formed by particles A and C. Assuming only Coulomb interactions between pair of particles, the $A^+B^+C^-$ and $A^-B^-C^+$ systems are equivalent. Without loss of generality, one can assume also that $m_C = 1$.

In mass-weighted hyperspherical coordinates, the potential surface is no longer symmetric for the ABC systems. In Fig. 5.11 the contour plots for the potential surfaces in the $\alpha$-set coordinates for $m_A = 26.58$, $m_C = 1$ and four different values of $m_B$ are shown. The choice of $m_B$ is such that $m_B = 17.75$ corresponds to a td$\mu$ system, $m_B = 8.88$ to a tp$\mu$ system and $m_B = 1$ to a $t^+\mu^+\mu^-$ system. Table 5.1 shows the $\chi$ angles where the potential surface exhibits singularities. As mass $m_B$ becomes smaller, one of the two $\chi$ angles increases, while the other decreases.

The adiabatic potential curves in the asymptotic region depend on the relative reduced masses $\mu_{BC}$ and $\mu_{AC}$. In Fig. 5.12 we show the two lowest potential curves for $L = 0$ for the four systems considered in Fig. 5.11. It is clear that if $\mu_{BC}$ and $\mu_{AC}$ are nearly equal, the lowest potential curve shows a rather deep potential well, while the upper curve is rather repulsive. As the mass $m_B$ deviates further from $m_A$, the separation between the two curves in the asymptotic region increases and each curve shows a weak potential well. The shallow potential well becomes insufficient to bound a stable state when $m_B$ becomes smaller than a critical value. To estimate the critical mass $m_B$ where at least one bound state exists, we use the WKB approximation. By evaluating the classical action

$$I = 2\int_{R_1}^{R_2} [E - U_1(R)]^{1/2}\, dR \tag{5.1}$$

at the threshold energy ($E = -1.0$), where $R_1$ is the inner turning point and $R_2$ is taken at infinity, the existence of $(n+1)$ bound states requires that the action integral be greater than $(n+3/4)\pi$. This is illustrated in Fig. 5.13 where the action $I$ is plotted against the mass ratio $m_C/m_B$ for fixed $m_A = 26.58$ and another for $m_A = 17.75$. Two horizontal lines are drawn to show the regions of zero, one and two bound states. According to this figure, there is no bound state for the $t^+\mu^+\mu^-$ system, two bound states for the $dt\mu$ and one bound state for the other two systems. According to this estimate, the mass of particle B has to be greater than 2.22 for a bound state to exist if $m_A = 26.58$. The critical mass for particle B is 2.63 if $m_B = 17.75$. Recall the mass of particle C is $m_C = 1$.

Other properties of Coulomb ABC systems were examined by Zhou et al. [115].

## 6. Applications of the hyperspherical close-coupling (HSCC) method

In Sections 4 and 5, we discussed the application of hyperspherical coordinates to atomic systems and to general Coulomb three-body systems within the adiabatic approximation. To achieve the accuracy normally required of atomic and molecular physics, it is necessary to go beyond the adiabatic approximation by including the coupling terms. If the hyperspherical approach is to become viable, it is essential to prove that the method is (i) capable of obtaining accurate numerical results more economically (in terms of computing time) for calculations which can be obtained by other approaches; and (ii) capable of doing calculations in regions where other approaches are not applicable or difficult to implement.

In order to go beyond the adiabatic approximation, as explained in Section 3, one can either solve the coupled hyperradial equations numerically or using the diabatic-by-sector method. The former is usually convenient if only a small number of coupled equations are included in the calculation, the latter is more convenient for high precision calculations where a large number of channels are included. We will give examples mostly for two-electron atomic systems where the numerical results obtained have been tested by experiments and by other elaborate calculations. The applications to atomic systems are summarized in Section 6.1 and to nonatomic systems are given in Sections 6.2 and 6.3.

### *6.1. Applications of HSCC to two-electron atomic systems*

The two-electron atoms such as He and $H^-$ have been subjected to numerous theoretical investigations over the years. We will focus on the application of the hyperspherical close coupling method to helium atoms only, starting with the ground state and singly excited states and then move up to the high energy part of the spectrum. The choice of the helium atom is appropriate since there are accurate variational results to compare with in the low energy part and experimental data for helium atom is most complete. For the ground state and the singly excited states, the results of the HSCC method are compared to those obtained by variational methods in 6.1.1. For low-lying doubly excited states the HSCC results are used to explain all the details of the most recent high-resolution spectra, as shown in 6.1.2.1. Most of the photoabsorption studies of helium atom start with its ground state. Theoretical calculations and experiments indicate that there are narrow resonances which are not easily populated by single photon absorption from the ground state. Recent calculations indicate that

Table 6.1
The convergence of the hyperspherical close coupling method versus the convergence of the configuration interaction method for calculating the total binding energy of the ground state of He [84].

| CI method | | HSCC | |
|---|---|---|---|
| Configurations | Energy (a.u.) | Number of basis functions | Energy (a.u.) |
| s limit | −2.879 00 | 10 | −2.903 3225 |
| s and p limit | −2.900 49 | 15 | −2.903 5055 |
| s, p and d limit | −2.902 77 | 21 | −2.903 5944 |
| s, p, d, and f limit | −2.903 32 | 23 | −2.903 5944 |
| experimental value: −2.90369 a.u. | | | |

these states are more easily populated by single photon processes from the metastable states. This subject is addressed in Section 6.1.2.2.

One of the major developments in the photoionization studies of helium atom in the last decade is in the energy region where the inner electron is also excited to a high-$N$ excited state. In this region, doubly excited states converging to different $N$ thresholds can interfere to produce modulations in the spectra. This portion of the helium spectra is examined in Section 6.1.3.

### *6.1.1. The ground state and singly excited states of helium*

In Section 4.1.2 we discussed the ground-state energy of $H^-$ calculated within the adiabatic approximation. The result, while in reasonable agreement with experiment, is far from what one can obtain from variational calculations. It is interesting to see what accuracy the HSCC method can achieve for such well-studied states.

In Table 6.1 the convergence of the HSCC method for the ground state energy of helium with respect to the number of channels included is shown [84]. It is also compared to the rate of convergence of the configuration interaction (CI) method. The HSCC method includes the channels systematically from the lowest ones up. The CI method approaches convergence from the smaller partial wave components up. From Table 6.1 it is clear that the HSCC method achieves faster convergence with respect to the number of basis functions used.

The HSCC method also can obtain accurate energy levels for the low-lying singly excited states. In Table 6.2, the results from the HSCC method are compared to the variational results using Hylleraas type basis functions [116] and with experimental results [117].

The HSCC method has also been used to calculate the phase shifts. In Fig. 6.1 the calculated phase shifts for different partial waves are compared to those obtained by the most elaborate close-coupling method obtained by Oza [118]. The agreement is quite excellent. In the accompanying figure at the bottom of Fig. 6.1 the dependence of the convergence of the phase shift with respect to the number of channels used in the HSCC method is illustrated. Notice that the number of channels needed at lower energies is larger. This may appear to be contradictory at first glance. However, recall that the channels used in the diabatic-by-sector method are not adiabatic channels. The diagonal nonadiabatic coupling term $\langle d^2\Phi/dR^2\rangle$ [Eq. (3.10)] which is included in the adiabatic potential, is not included in the potential obtained in the diabatic-by-sector basis functions. At lower energies the adiabatic basis is expected to be more accurate and the phase shift is more sensitive to the potential curve. This in turn implies that a larger number of diabatic-by-sector basis functions is required in order

Table 6.2
The total energy ($-E$) for singly excited states of helium (in a.u.). From Tang et al. [84].

| State | Variational | HSCC | Experiment |
|---|---|---|---|
| 1s1s $^1S^e$ | 2.90372 | 2.90353 | 2.90369 |
| 1s2s | 2.14597 | 2.14593 | 2.14597 |
| 1s3s | 2.06127 | 2.06126 | 2.06127 |
| 1s2s $^3S^e$ | 2.17523 | 2.17528 | 2.17524 |
| 1s3s | 2.06869 | 2.06870 | 2.06869 |
| 1s2p $^1P^o$ | 2.12384 | 2.12389 | 2.12387 |
| 1s3p | 2.05515 | 2.05521 | 2.05517 |
| 1s2p $^3P^o$ | 2.13316 | 2.13319 | 2.13317 |
| 1s3p | 2.05808 | 2.05813 | 2.05808 |

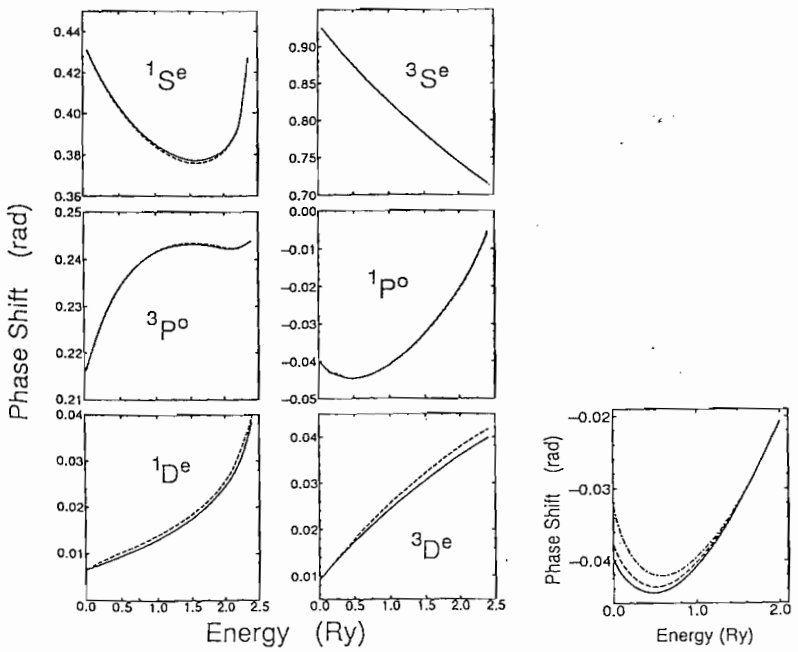


Fig. 6.1. The $^{1,3}S^e$, $^{1,3}P^o$, and $^{1,3}D^e$ phase shifts as a function of incident electron energy for $e^- + He^+$ collisions. The solid curves are from the hyperspherical close coupling calculation of Tang et al. [84], and the dashed curves are from the close coupling calculations of Oza [118]. The bottom graph shows the convergence test of the HSCC method with respect to the number of channels included. The number of channels used are 26, 32 and 36 counting from the top of this graph. Note that the convergence is slower at energies near the threshold. From Tang et al. [84].

to reproduce the $\langle d^2\Phi/dR^2\rangle$ term neglected. Notice that the convergence of the diabatic-by-sector method depends on the sector size chosen.

*6.1.2. The low-lying doubly excited states of helium*

*6.1.2.1. Photoabsorption from the ground state of He.* Photoabsorption spectra of helium in the energy region below the $He^+(N = 2)$ threshold were initially studied by Madden and Codling in 1963 [95] where they observed striking resonances which were attributed to doubly excited states of helium. Since then, there have been many more experimental studies as well as numerous theoretical calculations. The best spectra obtained recently are those from Domke et al. [102] which are shown in Fig. 6.2. These spectra display striking resonances belonging to the $^1P^o$ symmetry. According to the classification scheme discussed in Section 4. there are three Rydberg series expected, with the quantum numbers $(K,T)^A = (0,1)^+$, $(1,0)^-$ and $(-1,0)^0$. In Fig. 6.2 each resonance is simply designated as $n+$ or $n-$, where $n$ is the principal quantum number of the outer excited electron and $+, -$ or 0 refers to the quantum number $A$.

The overview of the spectra, as shown in (a), indicates that only the + series is prominently populated. Higher members near the series limit are shown in (b) and (c). In (a) and (b), several very weak resonances designated as n- can be seen. The $n$-spectra, when expanded further, as shown in Fig. 6.3, display additional features [119]. By a careful fitting, one can see that the nth member of the $(-1,0)^0$ series, designated as 2p$n$d series in the figure, overlap strongly with the $(n+1)$th member of the $(1,0)^-$ series. The spectra in Fig. 6.3 were taken with an energy resolution of 4.5 meV.

For the doubly excited states of He below the $He^+(N = 2)$ threshold, there are large numbers of calculations which are in good agreement with the experiment. The hyperspherical close-coupling calculations are also capable of producing results which are in good agreement with these calculations and with experiments. In Fig. 6.4 the global spectra calculated using the HSCC method [120] which has been convoluted with experimental resolution are compared to the experimental data. The HSCC calculation can also reproduce the spectra of the weak resonances. In Fig. 6.5 the photoabsorption cross section near the $(1,0)^-$ and $(-1,0)^0$ resonances, which are designated as $(n,-)$ and $(n,0)$ in the figure, are shown [119]. The spectra obtained from the HSCC method and convoluted with the experimental energy resolution [121], are shown to be in good agreement with experimental data.

The positions and widths of the first few doubly excited states of Fig. 6.2 have been analyzed. They are listed in Table 6.3 [84] and are shown to be in good agreement with experimental data [95,122].

The HSCC method can be easily extended to study resonances below the higher excitation thresholds of $He^+$. In Table 6.4 the positions and widths of the first few resonances below the $He^+(N = 3)$ threshold for the $^1P^0$ symmetry calculated using the HSCC method are compared to results obtained by other theoretical approaches [123,124], and to experiments [125,126]. The energy positions and the widths of the + states are seen to be in good agreement among the theoretical calculations and the experiments. For the width of the − series, the disagreement among calculations is still quite large.

*6.1.2.2. Photoabsorption from the metastable $1s2s^{1,3}S^e$ states of He.* The experimental and theoretical results in the previous section indicate that the narrow resonances $(A = -, 0)$ are not prominently

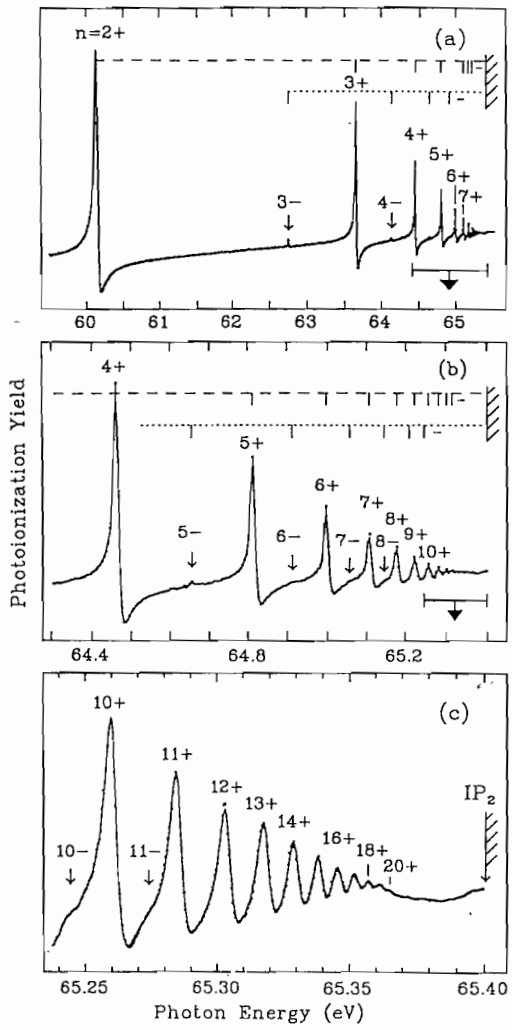


Fig. 6.2. Photoabsorption spectra near the $N = 2$ threshold of $He^+$ obtained by Domke et al. [102]. The labeling of the states, see text.

populated by photoabsorption from the ground state of He. This quasi-selectivity in the population of doubly excited states has been formulated in terms of a set of quasi-selection rules for the quantum numbers in photoabsorptions: $\Delta v = 0$, $\Delta T = 1$ and $\Delta A = 0$ (recall that $v = N - K - 1$, see Section 4.2.3). Since the ground state is designated as $v = 0$, $A = +1$ and $T = 0$, the dominant doubly excited states populated for $N = 2$ are those belonging to the $(K,T)^A = (0,1)^+$ series, consistent with the spectra in Fig. 6.2. It is evident that this quasi-selection rule states that the $-$ and 0 resonances are not easily observed by photoabsorption from the ground state.

To populate the $A = -1$ and $A = 0$ doubly excited states, it is easier to perform single photoabsorption from the metastable states of helium. Unlike the ground state, the metastable $1s2s^{1,3}S^e$ states are not very accurately represented by the $(K,T)^A$ designation. In other words, photoabsorption from

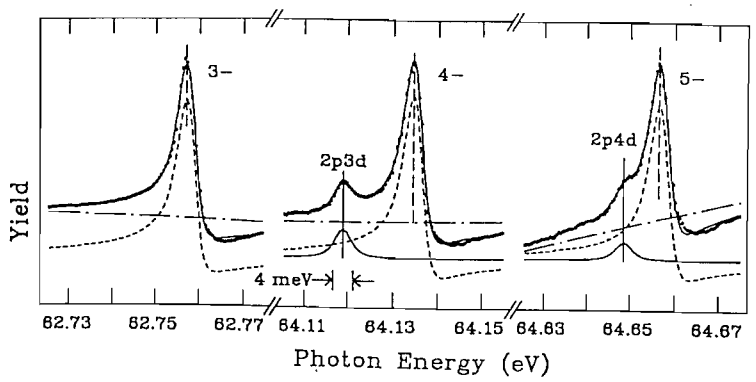


Fig. 6.3. Detailed structures near the first three $A = -$ resonances of Fig. 6.2. The 2p$n$d series is located close to the $A = -$ resonances. Data from Domke et al. [119].

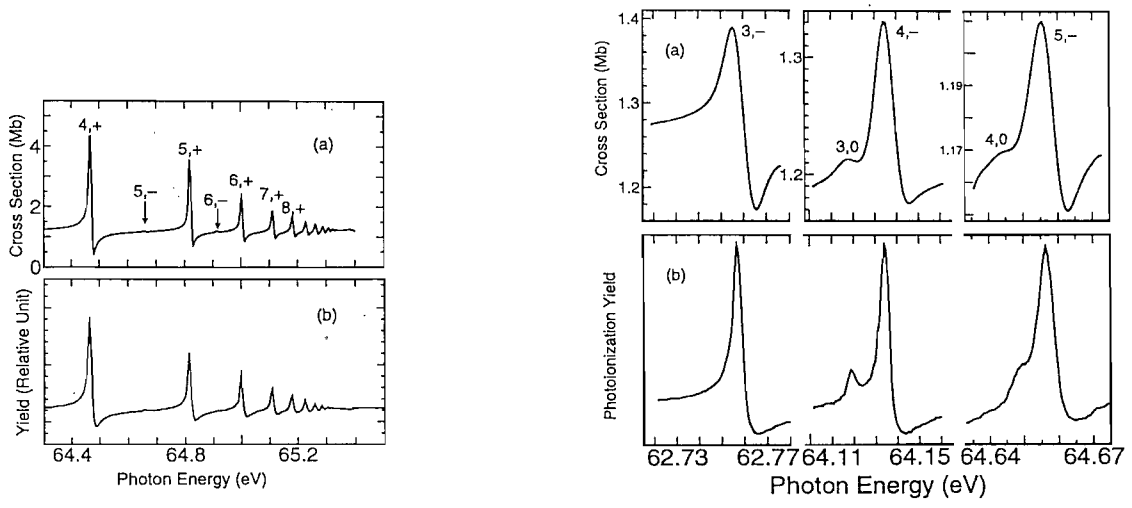


Fig. 6.4. Comparison of the photoabsorption spectra of He below the $N = 2$ threshold obtained by (a) the HSCC method and (b) the experimental data of Domke et al. [102]. From Tang et al. [121]. The theoretical spectra has been convolved with experimental resolution.

Fig. 6.5. Comparison of the photoabsorption spectra of He below the $N = 2$ threshold for the weak $A = -$ and $A = 0$ series. The upper figure is from the HSCC method convoluted with the experimental resolution [121]. The labeling of the states are $(n, A)$ where $n$ is the principal quantum number of the outer electron.

the metastable states is not likely to follow the same quasi-selection rule as from the ground state. To illustrate this point, we compare in Fig. 6.6 the calculated photoabsorption spectra in the energy region below the $He^+(N = 2)$ threshold, starting initially from the ground state or from the $1s2s\,^1S^e$ state [127]. Each resonance is labeled using the simplified $K_n^A$ designation in the figure. Because of the narrowness of the $A = -$ and $A = 0$ resonances, it is more appropriate to compare the two spectra after they have been convoluted with a "reasonable" resolution of 5.4 meV. (This is roughly the resolution of the experiment of Domke et al. [102].) Such a comparison is done in the lower two frames of Fig. 6.6. It is clear that photoabsorption spectra from the $1s2s\,^1S^e$ metastable state are

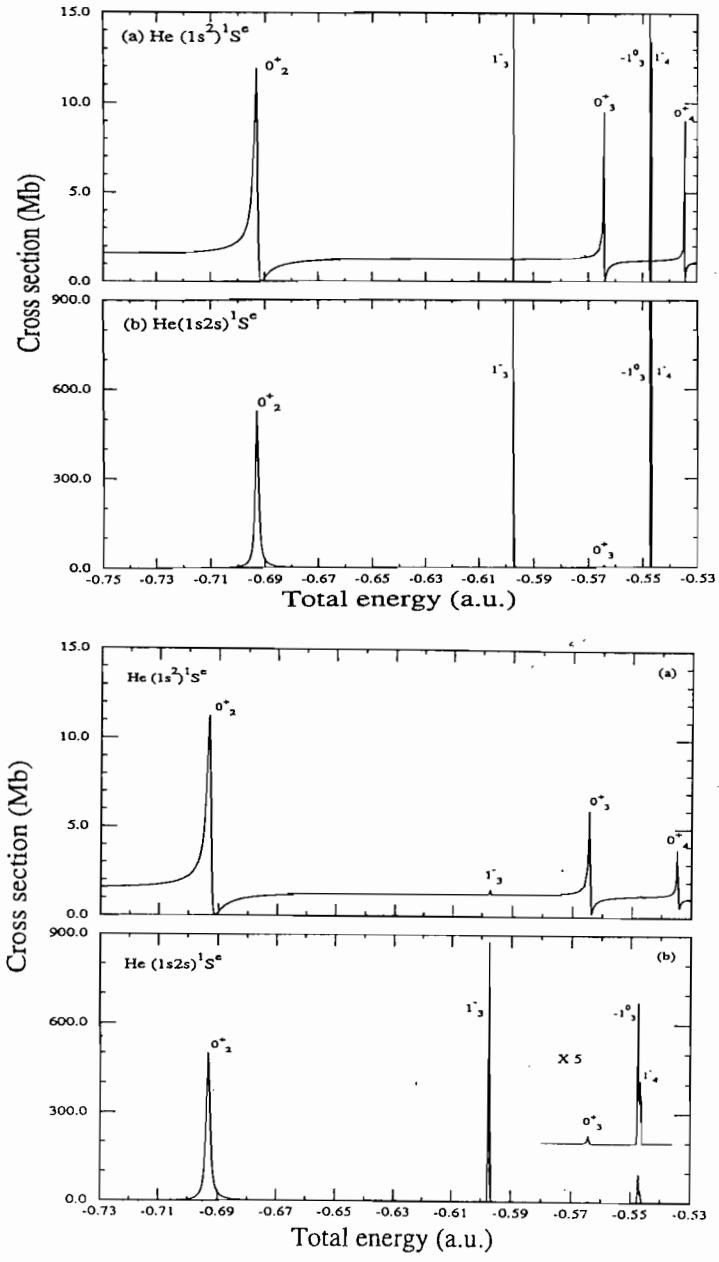


Fig. 6.6. Upper two frames: Comparison of the photoabsorption spectra of He from the ground state and from the metastable $1s2s^1S^e$ state versus the total energy of He. The autoionizing states below the $N = 2$ threshold are labeled as $K_n^A$. Lower two frames: The same spectra obtained by convoluting with an energy resolution of 5.4 meV. From Zhou et al. [127].

Table 6.3
Comparison of the position and width for $^1P^o$ states of He with results from photoabsoprtion experiments. Resonance positions are given with respect to the ground state of helium (at −79.0037eV). From Tang et al. The experimental data are from MC [95], and from ME [122]. The HSCC is from the hyperspherical close coupling calculation [84].

| $N(K,T)^A n$ | MC | ME | HSCC |
|---|---|---|---|
| $E_r$ (eV) | | | |
| $2(0,1)^+2$ | 60.133±0.015 | 60.151±0.010 | 60.156 |
| $2(0,1)^+3$ | 63.655±0.007 | 63.655±0.010 | 63.658 |
| $2(0,1)^+4$ | 64.466±0.007 | | 64.463 |
| $2(1,0)^-3$ | 62.758±0.010 | | 62.760 |
| $2(1,0)^-4$ | 64.141±0.016 | | 64.134 |
| $\Gamma$ (eV) | | | |
| $2(0,1)^+2$ | 0.038±0.004 | 0.038±0.004 | 0.0372 |
| $2(0,1)^+3$ | 0.008±0.004 | 0.0083±0.002 | 0.00808 |

Table 6.4
Comparison of theoretical and experimental results for the energy and width of $^1P^o$ doubly excited states of He below the $N = 3$ threshold of $He^+$. Resonance positions are with respect to the ground state (−79.0037 eV). Other theoretical results: MS [123], HC [124]; experimental results: WS [125], ZKRR [126]. From Tang et al. [84].

| | Theoretical | | | Experimental | |
|---|---|---|---|---|---|
| $N(K,T)^A n$ | MS | HC | HSCC | WS | ZKRR |
| $E_r$ (eV) | | | | | |
| $3(1,1)^+3$ | 69.8793 | 69.8721 | 69.8742 | 69.917(12) | 69.880(22) |
| $3(1,1)^+4$ | 71.6372 | 71.6242 | 71.6127 | 71.601(18) | 71.625(30) |
| $3(-1,1)^+3$ | 71.3204 | 71.3086 | 71.3026 | 71.30(4) | 71.261(30) |
| $3(2,0)^-4$ | 71.2264 | 71.2236 | 71.2223 | | |
| $\Gamma$ (eV) | | | | | |
| $3(1,1)^+3$ | 0.189 | 0.190 | 0.190 | 0.178(12) | 0.180(15) |
| $3(1,1)^+4$ | $8.18\times10^{-2}$ | $8.2\times10^{-2}$ | $8.13\times10^{-2}$ | 0.096(15) | |
| $3(-1,1)^+3$ | $3.74\times10^{-2}$ | $3.9\times10^{-2}$ | $3.35\times10^{-2}$ | 0.07 | 0.073(15) |
| $3(2,0)^-4$ | $8.75\times10^{-4}$ | $7.6\times10^{-3}$ | $1.90\times10^{-3}$ | | |

quite different from those from the ground state. The spectra do not show strong asymmetry, since the background continuum is weak in this energy region, as it corresponds to the single photoabsorption from the weakly bounded 2s orbital. Thus all the doubly excited states appear to have Lorentzian shapes. Another striking feature is that the $A = -$ and $A = 0$ resonances are more prominently populated.

The calculated photoabsorption spectra from the metastable $1s2s^1S^e$ state in the energy region below the $He^+(N = 3)$ threshold are also distinctly different from those from the ground state. In Fig. 6.7 we compare the two spectra which have been folded with 5.4 meV resolution. It is most striking that the $A = -$ and $A = 0$ resonances are prominently populated if the photoabsorption is carried out from the metastable state.

The metastable $1s2s^3S^e$ state has a longer lifetime. It is more likely that photoabsorption measure-

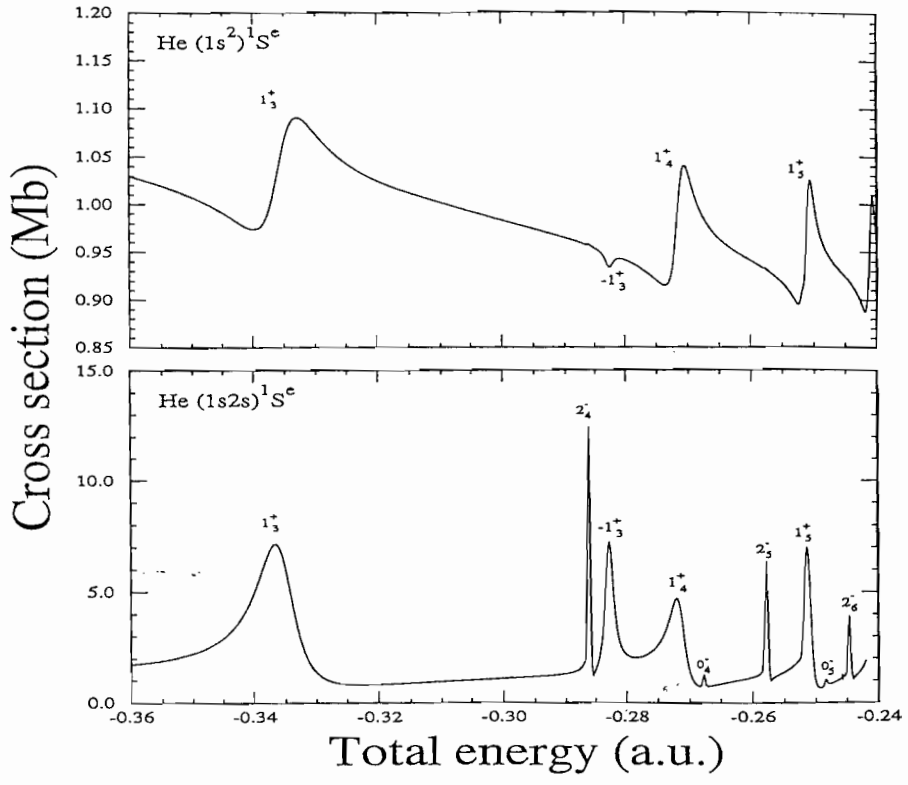


Fig. 6.7. Comparison of the photoabsorption spectra of He from the ground state and from the metastable $1s2s^1S^e$ state versus the total energy of He in the resonance energy region below the $N = 3$ threshold. The spectra shown are obtained assuming an energy resolution of 5.4 meV. The autoionizing states below the $N = 3$ threshold are labeled as $K_n^A$. From Zhou et al. [127].

ment from metastable helium will be carried out from this state. The predicted spectra calculated using the HSCC method and convoluted with an energy resolution of 5.4 meV are shown in Fig. 6.8. In the upper frame, it is seen that all the three series $(1,0)^+$, $(0,1)^-$ and $(-1,0)^0$ which lie below the $N = 2$ threshold of $He^+$ are populated. In the lower frame, the resonances below the $N = 3$ threshold of $He^+$ are displayed. The five series expected are $(K,T)^A = (2,0)^+$, $(1,1)^-$, $(0,0)^+$, $(-1,1)^-$, $(-2,0)^0$. There is no clear indication of quasi-selectivity and both the + and − resonances are populated. In the figure, each resonance is designated as $K_n^A$. Note that the resonances in the upper frame are almost Lorentzian, while those in the lower frame show significant interference.

### *6.1.3. The high-lying doubly excited states*

The autoionizing states associated with the higher thresholds of $He^+$ are shown in Fig. 6.9 which are taken from Domke et al. [102]. For resonances below the $N = 3$ and $N = 4$ thresholds, the dominant doubly excited states are those which follow the quasi-selection rule, i.e., the $(K,T)^A = (N-2,1)^+$ series for each $N$ and they appear as window-like resonances. However, the spectra below the $N = 5$ and $N = 6$ thresholds indicate that additional new features appear: The higher members of the Rydberg series show strong modulations. This modulation is the result of "spectral interaction" between the

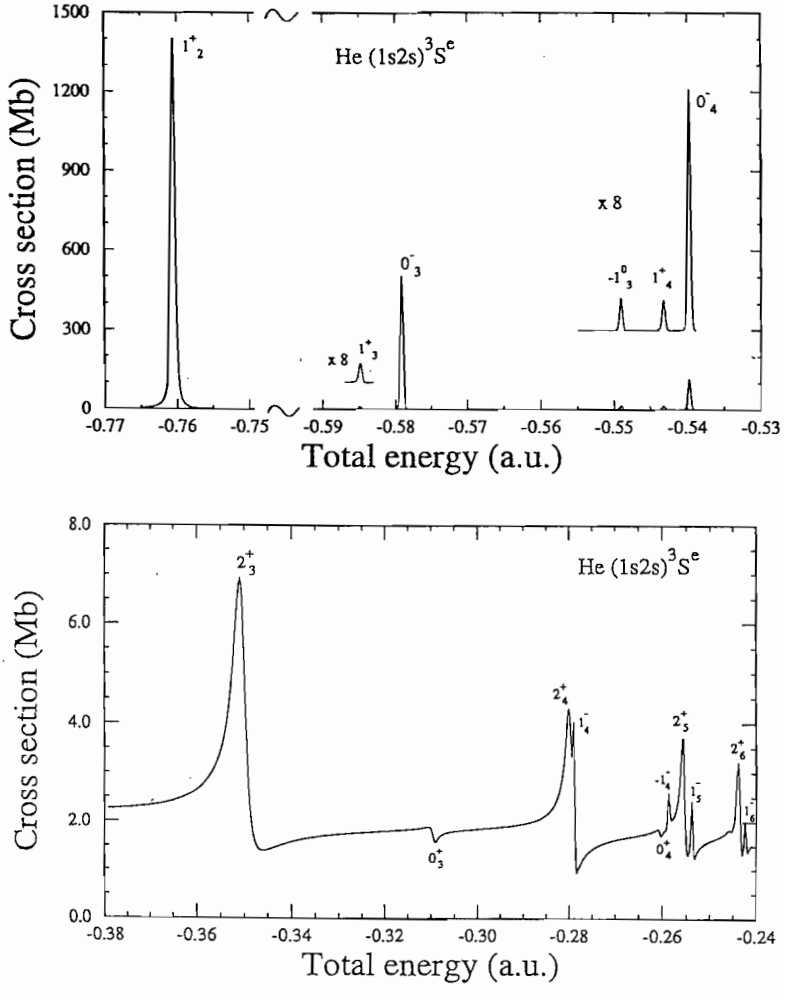


Fig. 6.8. Photoionization spectra from the metastable $1s2s^3S^e$ state of He in the energy region (a) below the $N = 2$ and (b) below the $N = 3$ thresholds. The spectra shown are obtained assuming an energy resolution of 5.4 meV. The autoionizing states are labeled as $K^A_n$. From Zhou et al. [127].

lowest intrashell state belonging to the higher threshold with the Rydberg series associated with the lower threshold. For example, the lowest intrashell state that converges to the $N = 6$ of $He^+$ lies below the $N = 5$ threshold, thus it overlaps with the Rydberg series of doubly excited states that converge to the $N = 5$ threshold. This overlap has the effect that the spectra interact and results in the modulation in the spectra. In Fig. 6.9 the spectra are labeled by $N$, $K_n$ (only the $A = +$ states are observed) quantum numbers. It appears that the $n = 9$–14 states of the $5, 3_n$ series is perturbed by the intrashell state $n = 6$ of the $6, 4_n$ series and resulting in the modulation of the Rydberg series.

The basic feature of interference can be understood in terms of the multichannel quantum defect theory (MQDT). The result from a three-channel MQDT fit is shown in Fig. 6.10 where the experimental data are shown as dots and the fitted result is shown in a solid curve. Since the intrashell

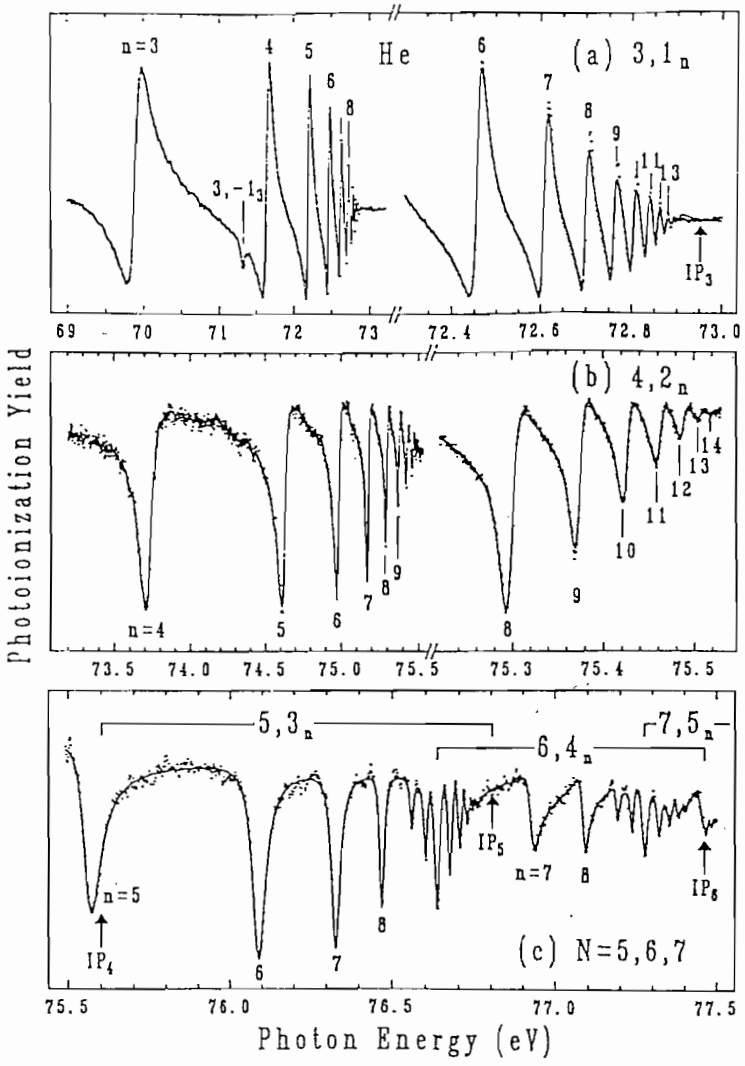


Fig. 6.9. Autoionizing states of He below the (a) $N = 3$, (b) $N = 4$ and (c) $N = 5, 6, 7$ thresholds [102]. The window resonances are labeled as $N$, $K_n$ in the figures. All of these states have $T = 1$ and $A = +$. Overlapping resonances are observed below the $N = 5$ and $N = 6$ thresholds.

state is far away from the series limit, the energy independent MQDT fitting is not accurate and thus the fitted spectra in Fig. 6.10 can only reproduce the experimental data fairly.

The HSCC method has been used to calculate the photoabsorption spectra in this energy region [128]. In Fig. 6.11 the calculated spectra [120] near the $N = 5$ and $N = 6$ thresholds of $He^+$ (covering an energy of about 1.2 eV) are compared to the experimental data of Domke et al. [102]. The details of the spectra and the modulations are all well reproduced from the HSCC method. In fact, it has been pointed out that other + series are populated weakly also [128]: they appear as minor depressions in the spectra, see Fig. 6.12. For example, the dominant series below the $N = 5$ threshold is the $(3, 1)^+$ series, and is being designated as $5, 3_n$ in the figure. The weaker $(1, 1)^+$

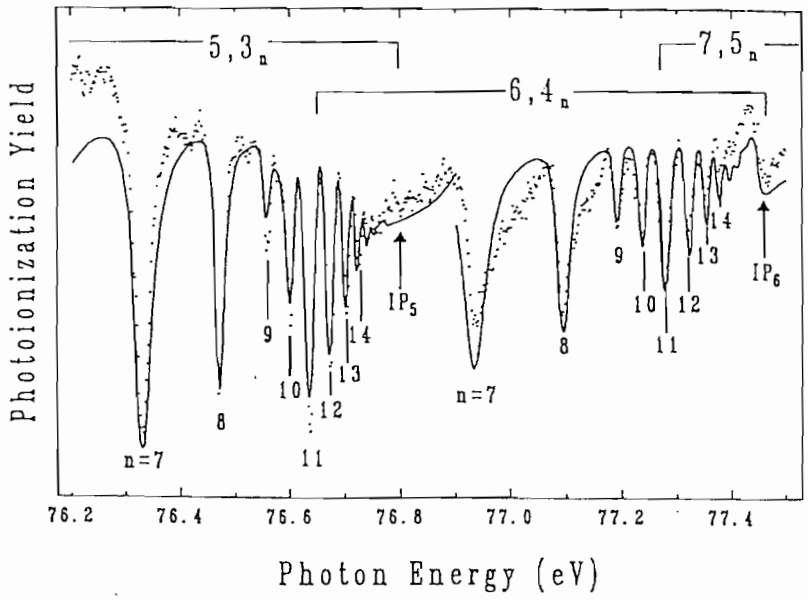


Fig. 6.10. Three-channel MQDT fit of the spectra in the overlapping resonance energy region (from [102]). The dots are the experimental data and the solid line is the fitted result.

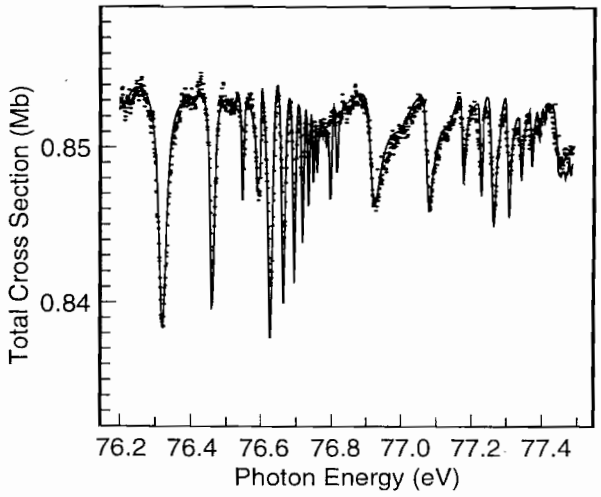


Fig. 6.11. The theoretical spectra calculated in the overlapping resonance region using the hyperspherical close coupling method as compared to the experimental data. From Tang [120].

series, designated as $5, 1_n$ in the figure, appear as weak structures, and are shown more clearly in the lower frame.

To summarize this section on the application of the HSCC method to the photoabsorption spectra of He, we comment that the diabatic-by-sector method was used to obtain the accurate ground state (or metastable states) energy and wave function, and in a separate calculation, the wave functions of the final states as a function of photoelectron energy were calculated. In a typical calculation,

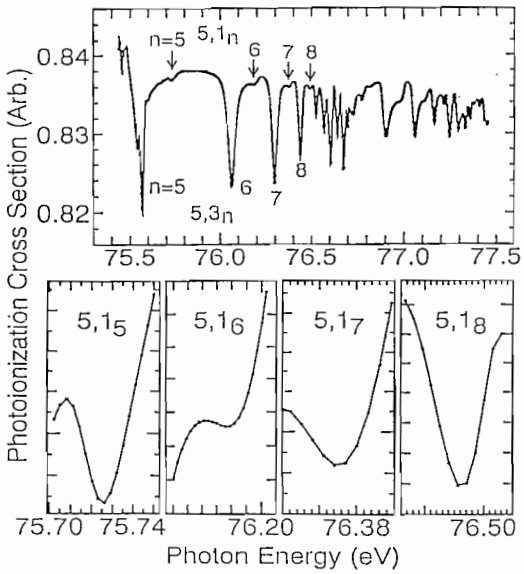


Fig. 6.12. Detailed view of the photoionization spectrum of He convoluted with experimental resolution of 6 meV below the $N = 5$ and $N = 6$ thresholds. The resonances are labeled as $N$, $K_n$. The dominant series is the $5, 3_n$ series, but the weaker $5, 1_n$ series can be seen also. The latter series also has $T = 1$, but with one additional degree of excitation in the angle $\theta_{12}$. The detailed structures of the weaker series are shown in the bottom frames (from Tang et al. [128]).

30–40 channels are easily included to achieve higher precision. The method can be applied to many energy points easily since it amounts only to solving the coupled hyperradial equations repeatedly. Thus in actual calculations, one can "trace" the narrow resonances to obtain the positions and widths precisely in a relatively short computer time. The HSCC has been shown to be an efficient method for calculating photoabsorption spectra over a broad energy region. It is especially useful for treating the higher energy region where other approaches become impractical. The other "workhorses" like the close-coupling method and the $R$-matrix method, since they are variational in nature with "ad hoc" choices of basis functions, in general amount to much larger calculations, and they are less useful for treating energy regions where many channels are open. Applications of HSCC to the photoabsorption of $H^-$ ions from the ground state have been carried out by Tang et al. [103]. The method has also been applied to obtain photoabsorption from the metastable $2p^2\,{}^3P^e$ state, and a number of narrow shape resonances near the $N = 3$ excitation threshold of H have been located [129].

### 6.2. *Positron scattering with atomic hydrogen and positronium formation*

The scattering of positrons by atomic hydrogen or other simple atoms has been studied extensively by a number of theoretical approaches. Typically, all the methods used for electron–atom collisions have been generalized to positron–atom scattering. For example, the Kohn variational method has been used by Humberston and coworkers [130,131], and the $R$-matrix method has been used by Higgins and Burke [132,133]. The close-coupling method, where the wave function is expanded in terms of atomic orbitals of atomic hydrogen and of positronium, has been applied by many groups, see [134,135,137,136]. Most of the calculations have used a small basis set so far.

The hyperspherical close coupling method, as outlined in Section 3 has been applied to study positronium formation cross sections in the collision between positions with atomic hydrogen recently by Igarashi and Toshima [87] and by Zhou and Lin [93]. This is a more recent development and thus few calculations have been obtained so far. On the other hand, the preliminary results appear to be very promising. In this section, we address the application of the hyperspherical close coupling method to the positronium formation cross section in the Ore gap energy region, i.e., between the positronium formation threshold and the $n = 2$ excited states of atomic hydrogen. Within this energy range, there are only two channels open; one is the elastic scattering of H by positron, and the other is the formation of positronium in the ground state. An earlier calculation was reported by Archer et al. [138] for the $J = 0$ partial wave.

The major task in applying the hyperspherical close coupling method is the accurate solution of the eigenvalues and eigenfunctions of the Schrödinger equation at fixed hyperradii. The numerical schemes that have been used were described in Section 3. In the work of Igarashi and Toshima, the Schrödinger equation at a fixed $R$ in the laboratory-fixed frame is solved using Slater orbitals constructed using $\beta$-set and $\gamma$-set Jacobi coordinates (see Fig. 2.2). In the approach of Zhou and Lin [93], the wave functions are expressed in the body-fixed frame with the $z$-axis chosen to be along the direction of the line connecting the positron and the proton. By separating out the rotational matrices, the resulting two-dimensional coupled differential equations are solved using the fifth-order finite element method [92]. The finite-element method was also used by Archer et al. [138]. They used lower-order polynomials to expand the wave functions within each element and the results are less accurate. The hyperspherical coordinates they used are also different. They used coordinates where the three particles are treated "democratically", a procedure more suitable for atom–diatom reactive scattering.

In the following the results from the HSCC method are compared to results obtained using the variational approach which is considered to be most accurate one in the low energy region.

*The s-wave.* In Fig. 6.13 the lowest ten potential curves for the positron–hydrogen system for $J = 0$ are plotted. To get a more clear picture of these curves, the effective principal quantum number $n^*(R)$ versus $R$ is plotted, where $n^*$ is related to the potential by $E(R) = -1/n^{*2}$ where the energy is given in Ry. In this way, potential curves that go to the hydrogenic limit will have integral values, while for the positronium limit the curves will approach nonintegral values in general.

The potential curves shown in Fig. 6.13 are actual diabatic potentials calculated. In the HSCC calculation of Zhou and Lin [93], twenty channels were coupled and the resulting elastic and positronium formation cross sections were calculated within the Ore gap energy region. The comparison with other calculations is made in Fig. 6.14 where the HSCC results [93] are shown as open triangles connected by a solid line. The variational results from Brown and Humberston [139], shown as open circles, are considered to be the most accurate. It is clear that the HSCC results are in good agreement with the variational results. The results from the other two hyperspherical approaches, from Igarashi and Toshima (shown as crosses) and from Archer et al. (shown as asterisks), are slightly off compared to the variational results. These differences most likely are due to the numerical accuracies. For the present system, there are many calculations based on the close-coupling expansion and only the results from the most recent one by Mitroy [137] are shown (in diamonds). The other results shown in the figure are from Winick and Reinhadrt [140] who used the so-called $T$-matrix method to calculate the elastic and total cross section. In the Ore gap region the difference between the two cross sections is the positronium formation cross section, shown as filled squares.

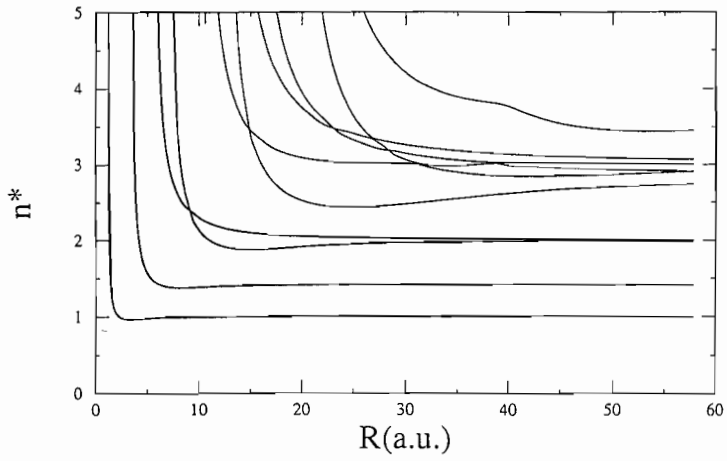


Fig. 6.13. The ten lowest $J = 0$ potential curves for the $e^+ + H$ system. The effective principal quantum number $n^*(R)$ is plotted versus $R$.

It is interesting to point out that a number of resonances have been predicted for the positron-hydrogen atom collisions. Sarkar et al. [136] predicted the existence of two very narrow resonances for s-wave scattering near the positronium formation threshold using close-coupling calculation by including 1s, 2s and 2p orbitals of atomic hydrogen and of the positronium, despite that the earlier calculations of Bhatia and Drahman [141] indicated that such resonances do not exist in an extensive calculation based on the complex coordinate rotation method. A newer and more extensive close-coupling calculation also shows that these resonances do not exist [142]. Based on the potential curves in Fig. 6.13, it is inconceivable that such narrow "shape" resonances can exist at energies slightly above the positronium formation threshold, especially since the second potential curve does not show any evidence of a potential barrier at large $R$.

Another much broader resonance has been predicted in the $R$-matrix [133] calculation and in the close-coupling calculation [135,134] in the elastic scattering cross section for each of the s-, p- and d-wave at energies around 2.5 Ry. The existence of a resonance at such high energies is most surprising, and it is not clear how such a resonance emerges based on the potential curves of Fig. 6.13. We mention that such resonances do not appear in the HSCC calculations, as shown by Igarashi and Toshima [87], and the predicted resonance is likely the result of the limited basis set used in the calculations. Note that the HSCC method includes the number of channels from the lowest one up systematically. Unlike the close coupling or the $R$-matrix approaches where the basis functions included in the expansion are based on the wave functions in the asymptotic region, and thus the effect of short-range correlation is included much less effectively.

*The p-wave.* The elastic and positronium formation cross sections for $J = 1$ are shown in Fig. 6.15. Comparison with other calculations are also shown using symbols as in Fig. 6.14. The positronium formation cross section for p-wave is rather large, almost comparable to the elastic cross section, at energies away from the positronium formation threshold. The HSCC results from Zhou and Lin are in good agreement with the variational results of Brown and Humberston, both for the elastic and positronium formation cross sections. Twenty channels were used in the calculation by Zhou and Lin, and the matching was carried out also at $R = 29.93$.

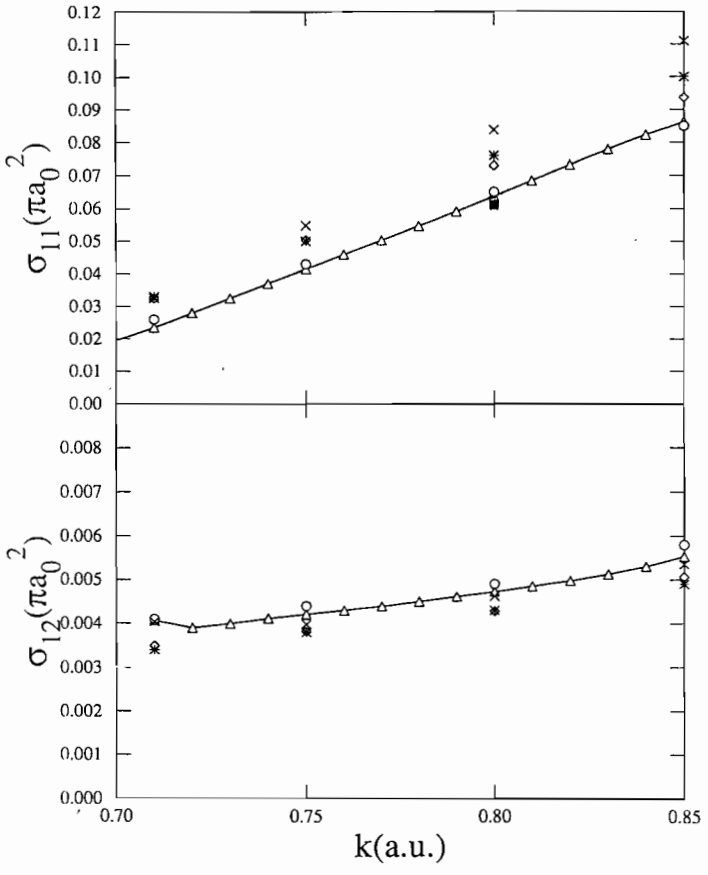


Fig. 6.14. S-wave elastic and positronium formation cross sections with respect to the incident wave number of positron in the Ore gap. Solid line and triangles, from Zhou and Lin[93]; open circles, from Brown and Humberston [139]; diamonds, from Mitroy[137]; crosses, Igarashi and Toshima [87]; asterisks, Archer et al. [138]; solid square, Winick and Reinhardt [140]. From Zhou and Lin [93].

*The d-wave.* The elastic and positronium formation cross sections for $J = 2$ are shown in Fig. 6.16, and the HSCC results of Zhou and Lin, who include 14 channels, six for $I = 0$, four each for $I = 1$ and 2, are in good agreement with the variational results of Brown and Humberston. Other calculations tend to deviate more from the variational results.

In conclusion, the HSCC method as applied to the positronium formation cross sections for positron scattering with atomic hydrogen shows that the HSCC method is capable of achieving accuracy comparable to those obtained using the more elaborate variational method. A key element in the numerical application is that the potential curves and basis functions at each fixed hyperradius be calculated accurately. In the work of Zhou and Lin, the higher order finite element method appears to be capable of achieving the required accuracy. Future application is to include more channels and to extend the calculations to higher energies.

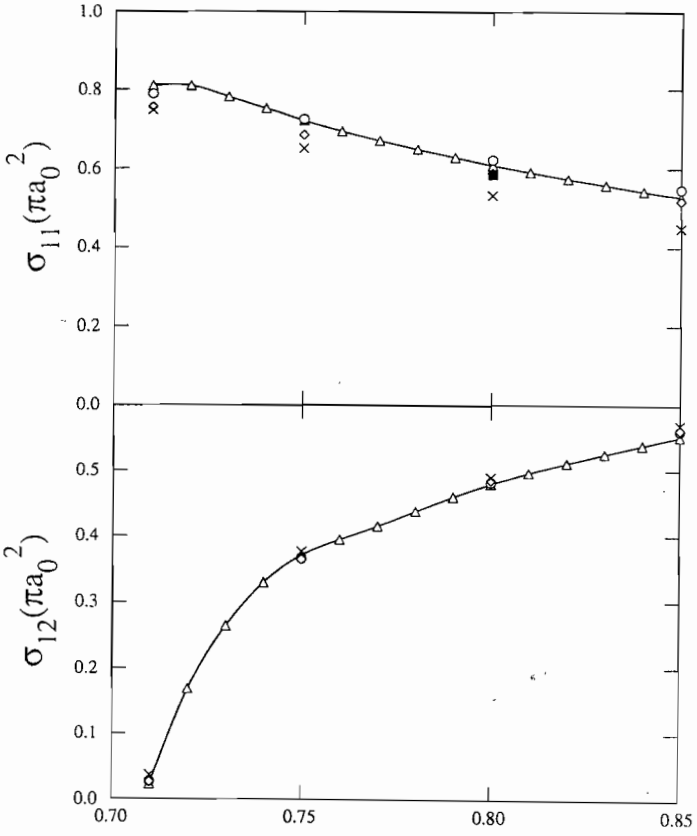


Fig. 6.15. As in Fig. 6.14 but for p-wave. From Zhou and Lin [93].

### 6.3. *Muonic molecules and muon transfer processes*

Muonic molecules $xy\mu$ where $x, y$ = p, d, t are interesting Coulomb three body systems which have attracted special attention in the last decade in connection with study in muon-catalyzed fusion [143–145]. These systems offer an unique opportunity to examine the effect of masses on properties such as binding energies, resonances, as well as muon transfer processes.

The starting theoretical approach for muonic molecules is the Born–Oppenheimer approximation, as in ordinary molecules. However, protons, deuterons, and tritons are only about 8.9, 17.8 and 26.7 times heavier, respectively, than muons. Deviations of the solution of the three-body systems from the prediction of the Born–Oppenheimer approximation become much larger for muonic systems. The limitation of the Born–Oppenheimer approximation appears even more acute since the required accuracy for the energy levels of muonic molecules in the study of muon catalyzed fusion is rather high, in the order of one part per million. In the last decade, many different theoretical approaches have been used to study muonic molecules. This section summarizes these approaches and presents preliminary results from calculations carried out using the hyperspherical close coupling method.

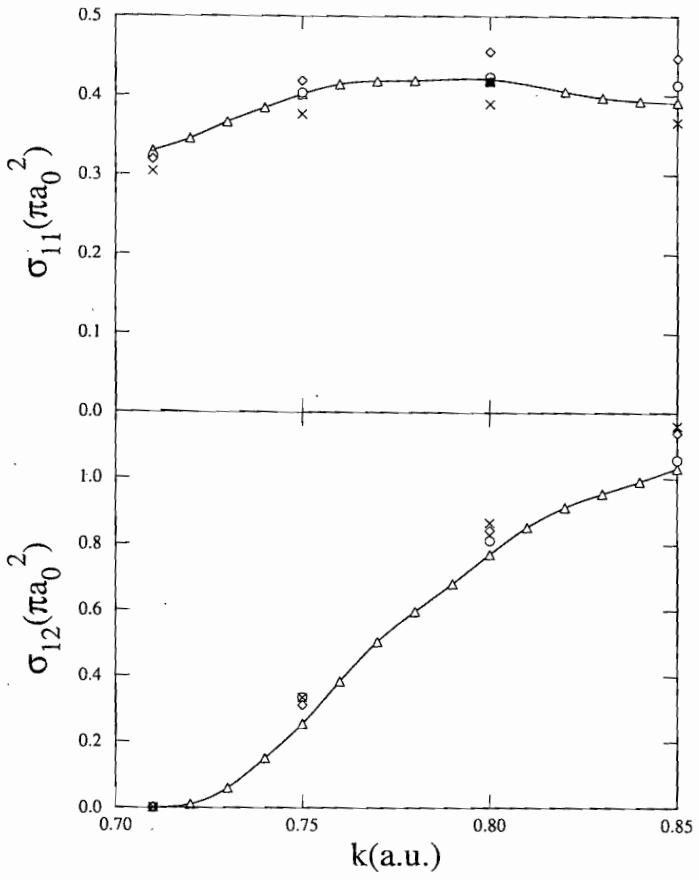


Fig. 6.16. As in Fig. 6.14 but for d-wave. From Zhou and Lin [93].

*6.3.1. Bound states*

The binding energies of the muonic molecules have been calculated by different variational methods. The known bound states are listed in Table 6.5 where the detailed sources of these calculations can be found in Puzynin and Vinitsky [146]. The dependence of the binding energies on the masses in the muonic systems is clear from this table. If the Born–Oppenheimer approximation is used, it is found that the $(j, v) = (1, 1)$ state for $dt\mu$ is bound at $-7.7$ eV instead of at $-0.660$ eV, and the same state for $dd\mu$ is not bound instead of at $-1.975$ eV.

The hyperspherical approach has been used to study the muonic molecules by a number of groups so far. Using the basis functions described in Section 3.3.2, Liu [147] calculated the two lowest adiabatic potential curves and the coupling term for $J = 0$ for the $dt\mu$ system. The lowest two potential curves are shown in Fig. 6.17 and the binding energies of the two bound states thus obtained are 318.95 eV and 40.133 eV. Comparing these with the results of Table 6.5, the energy for the first state is reasonable, but the second state is not accurate at all. The error is most likely due to the inaccuracy in the hyperspherical potential curves at at large $R$. To achieve higher precision, it is essential that the potential curves and the coupling terms in the large-$R$ region be calculated

Table 6.5
The binding energies of muonic molecules. From Cohen [143]. (For detailed sources and discussion, see Ref. [162].

| $J, v$ | $E_b$ (eV) | | | | | |
|---|---|---|---|---|---|---|
| | pp$\mu$ | pd$\mu$ | pt$\mu$ | dd$\mu$ | dt$\mu$ | tt$\mu$ |
| 0,0 | 253.15 | 221.55 | 213.84 | 325.07 | 319.14 | 362.91 |
| 0,1 | – | – | – | 35.84 | 34.83 | 83.77 |
| 1,0 | 107.27 | 97.50 | 99.13 | 226.68 | 232.47 | 289.14 |
| 1,1 | – | – | – | 1.97 | 0.66 | 45.21 |
| 2,0 | – | – | – | 86.45 | 102.65 | 172.65 |
| 3,0 | – | – | – | – | – | 48.70 |

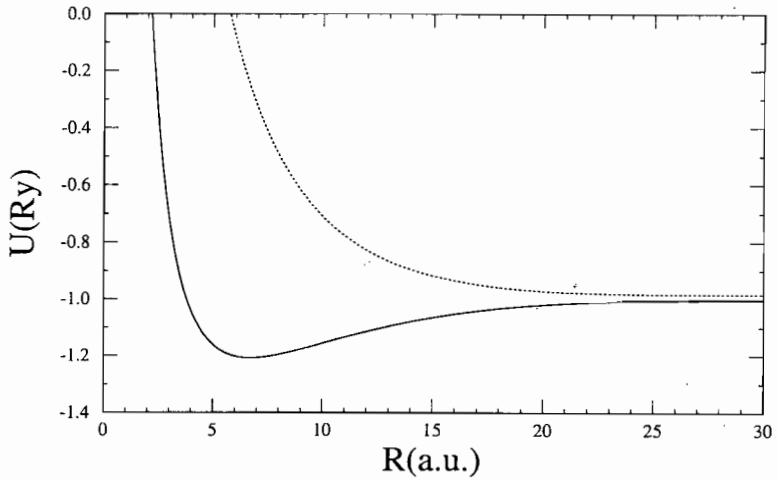


Fig. 6.17. The two lowest $J = 0$ potential curves for the dt$\mu$ system.

more accurately. A more careful calculation for the muonic molecules has been reported by Gusev et al. [148]. They introduced hydrogen-like basis functions of the two dissociation channels in the basis set in addition to the typical polynomials used in the finite-element approach. These added basis functions insure that wave functions and potential curves at large hyperradii are also adequately represented. They solved the standard adiabatic coupled equations of the form of Eq. (3.10) and examined the convergence with respect to the number of channels included in the calculation. For example, their two-channel results are 317.686 eV and 33.539 eV, respectively. If the calculations are of the same precision, the two results from Liu [147] and from Gusev et al. [148] are expected to be identical. By including six channels in the calculation, Gusev et al. [148] obtained 318.903 eV, and 34.759 eV, respectively, in much better agreement with the variational results. Thus the indication is that the major obstacle for achieving high precision calculations on the binding energies is associated with the numerical problem.

Using spheroidal coordinates and variational wave functions, Hara et al. [149] obtained the adiabatic hyperspherical potential curves and nonadiabatic coupling terms for the three lowest $J = 0$ curves for dt$\mu$. The binding energies they obtained for one channel are $-317.75$ and $-31.99$ eV. By including the couplings among the three channels, they obtained $-318.72$ and $-34.36$ eV. The latter

Table 6.6
Elastic and muon-transfer cross section for $d\mu+$ t collisions. The cross sections are given in units of 10–20 $cm^2$. The results from the first two calculations are carried out by solving the two adiabatic hyperspherical potential curves, from Liu [147] and from Fukuda et al. [153]. The column under ZL is from solving ten channel hyperspherical close coupling equations, from Zhou and Lin [152]. The variational results are from Kamimura [154].

| $E_{in}$ (eV) | Liu | FIS | ZL | Variational |
|---|---|---|---|---|
| $10^{-3}$ | elastic | 2.0 | 1.7 | |
| | transfer | 15.0 | 9.1 | |
| $10^{-2}$ | elastic | 2.5 | 2.3 | |
| | transfer | 5.0 | 2.9 | 5.06 |
| $10^{-1}$ | elastic | 4.0 | 1.7 | ... |
| | transfer | 1.8 | 1.9 | |

are to be compared to the variational results of −319.14 and −34.83 eV (see Table 6.5).

The binding energies of the above two states have also been calculated using the hyperspherical close coupling method using diabatic basis functions. By including ten coupled channels, the energies obtained are −321.19 and −36.36 eV by Zhou and Lin [152] where the potential curves and channel functions are obtained using the finite-element method. In fact, the same program used for doing positron-hydrogen atom collisions described above was used, except that the masses of the particles were changed accordingly. The discrepancies between the energies obtained so far are most likely due to the lack of high precision in the potential curves at large $R$.

### 6.3.2. *Muon transfer cross sections*

Muon transfer is an essential step in a muon catalyzed fusion cycle if the muon is initially captured on the deuteron. The initial capture occurs in highly excited states of $(d\mu)$ but the time for it to cascade down to the 1s state is negligible. The transfer of muon from d to t is irreversible since the binding energy of $t\mu$ is 48.042 eV lower than that for $d\mu$.

The hyperspherical method has been applied to calculate muon transfer cross sections by coupling the two lowest adiabatic channels. In applications to muon-catalyzed fusion, the transfer cross sections or rates at thermal energies are of interest. In Table 6.6 the results for $J = 0$ from different hyperspherical approaches are compared. The difference between Liu [147] and Fukuda et al. [153] is mostly due to the difference in numerical accuracy. The calculation of Zhou and Lin [152] employed ten diabatic basis functions in the inner region using HSCC method and matched to the asymptotic solutions at $R = 60$. The results from all of these three calculations may still need to be considered preliminary for collisions at such low energies. The asymptotic wave functions in the outer region used in these calculations are just spherical Bessel and Neumann functions. At low energy collisions, the effect of induced dipole polarization potential may become significant. On the other hand, the results from all three calculations are in reasonable agreement with the variational calculation of Kamimura [154].

The $J = 0$ muon transfer cross section for $d\mu + t \rightarrow d + t\mu$ is shown in Fig. 6.18 [155] over an extended energy range. The open symbols are the results of considering electron screening for $d\mu + T \rightarrow D + t\mu$ where $T = (t^+e^-)$ and $D = (d^+e^-)$. The results shown are from the two-state

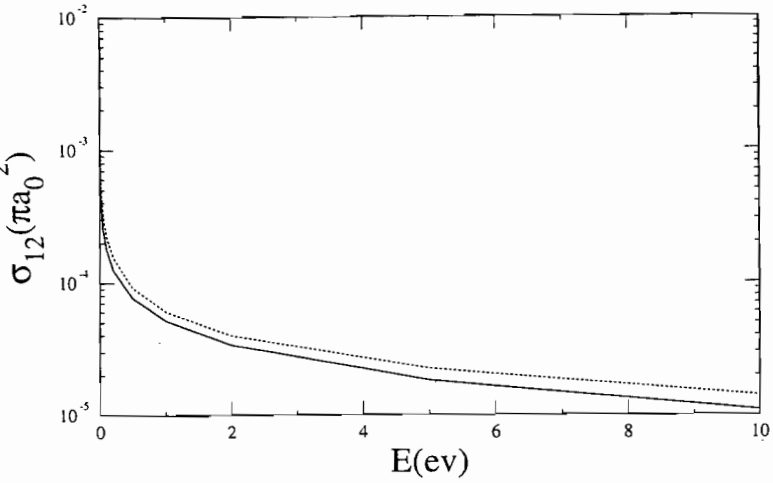


Fig. 6.18. Comparison of muon transfer cross sections for the $J = 0$ partial wave in the energy region from threshold to about 80 eV. The results from the HSCC [160] are compared to those from the improved adiabatic approximation [155].

model based on the "improved adiabatic approximation". The results from the ten-channel HSCC calculation [160] are also shown. The differences between the two results are small.

Muon transfer involving excited states of $d\mu$ and $t\mu$ are important processes in muon catalyzed fusion. So far no good theoretical calculations have been carried out. The variational method of Kamimura is not easily generalized to higher states, but the hyperspherical close coupling method can be extended to include these channels. On the other hand, the high numerical accuracy needed for such studies may still pose complications.

### 6.3.3. *Resonances below the $N = 2$ thresholds of $t\mu$ and $d\mu$*

The resonances of $xy\mu$ systems below the $N = 2$ thresholds of $x\mu$ or $y\mu$ ($x, y = \mathrm{p, d, t}$) are similar to the resonances of $H^-$ below the $N = 2$ threshold of H where the degenerate hydrogenic states are coupled to form a dipole potential that can support an infinite number of resonances. In view of the success of the hyperspherical close coupling method for applying to helium and $H^-$ ions (Section 6.1), it is expected that these resonances can be accurately determined for these ions using the HSCC method. Other theoretical studies have been carried out already in this spectral region for a number of muonic ions [149,151,150].

### 6.3.4. *Other muonic molecular ions*

There are other muonic molecular ions $x\mathrm{He}\mu$ consisting of a hydrogen isotope ($x = \mathrm{p, d, t}$) and a He isotope ($^3$He or $^4$He). Among these ions, $\mathrm{d}^3\mathrm{He}\mu$ and $\mathrm{d}^4\mathrm{He}\mu$ below the $(\mathrm{d}\mu)^{3,4}_{1s}$He threshold are of interest because they can participate in the reaction

$$(\mathrm{d}\mu)_{1s} + \mathrm{He} \rightarrow (\mathrm{dHe}\mu)_{J=1} \rightarrow (\mathrm{He}\mu)_{1s} + \mathrm{d} + h\nu(6.7\,\mathrm{keV}). \tag{6.1}$$

The lowest potential curve for the $x\mathrm{He}\mu$ ion is repulsive which dissociates into $x^+$ and $(\mathrm{He}\mu)^+$ and the upper curve has a shallow attractive potential well which can support quasi-bound states. These states can decay by bound-to-free X-rays, as observed in $\mathrm{d}^4\mathrm{He}\mu$ by Matsuzaki et al. , [156]

and confirmed by the calculation of Hara and Ishihara [157]. These states can also decay by breaking up into $(He\mu)_{1s} + d + 8.2$ keV, and the rates have been calculated by Kino and Kamimura [158]. No studies using hyperspherical coordinate methods have been carried out yet. We mention that such muonic ions are similar to $HeH^{2+}$ ions where the lifetime has been examined recently by Ben-Itzhak et al. [159].

## 7. Conclusions and perspective

In this review we summarized the progress made in the application of hyperspherical coordinates to Coulomb three-body systems. In particular, we addressed problems associated with higher excited states. By treating the hyperradius as an adiabatic parameter, we showed that the adiabatic potentials and the associated wave functions at each fixed hyperradius offer a convenient basis for labeling the states and a set of approximate quantum numbers can be deduced in terms of the nodal structure of the wave functions. The hyperspherical coordinates offer a unified viewpoint for describing all three-body systems.

We had also shown that accurate numerical results can be obtained using the recently developed hyperspherical close coupling method. In applying the hyperspherical close coupling method to problems in two-electron atoms, we had shown that the results are not only as good as those obtained by variational methods for the low-lying excited states, but also the method has been applied to high-lying doubly excited states where the number of open channels is rather large. The latter states are not easily obtained using the standard $R$-matrix or the close-coupling method. Another important feature of the hyperspherical approach is that it can be generalized to study rearrangement collisions. In Sections 6.2 and 6.3 we showed some of the recent results. The number of applications in rearrangement collisions is only in beginning stages, and we expect much more to come in the near future.

In this review we focussed on the application of hyperspherical approaches to three-body systems where the interaction potential was limited to the Coulomb interaction only. The method is quite general, however, and can be applied to problems if other interaction potentials are used. Some applications of the hyperspherical approach to two- valence electron atoms have already been done, either using the adiabatic approximation or using the hyperspherical close coupling method [160].

Generalization of hyperspherical approach to problems of more than three particles is possible, although the task will be formidable. The addition of another particle introduces three more degrees of freedom to the problem. The nature of hyperspherical harmonics for the few-body systems has been discussed in the literature, and some limited applications to atomic three-electron systems have been done. However, unless accurate numerical approaches can be developed, practical applications will be limited. For three-electron systems, the channel functions have been reduced to a set of coupled partial differential equations [70] which can be solved numerically. Preliminary results from solving the coupled two-dimensional eigenvalue problems using the B-spline technique appear to be quite promising [161]. Once accurate hyperspherical potential curves and eigenfunctions are obtained, it is straightforward to apply the hyperspherical close coupling method to solve the bound and scattering problems.

The straightforward generalization of the hyperspherical approach to $N$-body problems is most likely not practical, nor necessary, for most applications if there are only a limited number of particles

excited in the system. For such systems, it would be desirable to develop methods that distinguish the core from the other "active" particles. As an example, to describe the doubly excited states of $He^-$ or Li, it would be useful to think of the system as consisting of a 1s core and two excited electrons. The relaxation of the core is minimum and can be represented by a small number of basis functions. The two excited electrons can be treated using hyperspherical coordinates as described in the present review. For problems involving triply excited states where the degrees of freedom for all the three electrons are all open, hyperspherical approach including all three electrons as described in the previous paragraph would still be necessary.

## Acknowledgment

Over the past two decades, we have witnessed the development of methods based on hyperspherical coordinates for few-body systems. The hyperspherical approach has emerged from the conceptual and qualitative tools to one of the main streams in theoretical physics, in areas ranging from atomic, nuclear and particle physics to chemical physics. The author would like to express his gratitude to Professor Ugo Fano who introduced him to this problem many years ago. The development in the last decade owed much to contributions from collaborators: S. Watanabe, C.G. Bao, X.H. Liu, J.Z. Tang, M. Matsuzawa and J. Shertzer and from graduate students and research associates: Z. Chen, B. Zhou, and Y. Zhou. The support from the US Department of Energy, Office of Energy Research, Office of Basic Energy Sciences, Division of Chemical Sciences over the years provides all the hardware and the software needed for making the progress reported here.

## References

[1] J. Avery, Hyperspherical Harmonics, Application in Quantum Theory (Dordrecht; Kluwer), 1989.
[2] U. Fano, Rept. Prog. Phys. **46**, 97 (1983).
[3] U. Fano and A. R.P. Rau, Atomic Collisions and Spectra, Academic Press, New York, 1986.
[4] C. D. Lin, Adv. At. and Mol. Phys. **22**, 77 (1986).
[5] T. H. Gronwall, Phys. Rev. **51**, 655 (1937).
[6] J. H. Bartlett, Phys. Rev. **51**, 661 (1937).
[7] V. A. Fock, Izv. Akad. Nauk. USSR, Ser. Fiz. **18**, 161 (1954).
[8] E. A. Hylleraas, Z. Physik, **54**, 151 (1929).
[9] K. Frankowski and C. L. Pekeris, Phys. Rev. A**46**, 146 (1966).
[10] D.L. Knirk, J. Chem. Phys. **60**, 66 (1974); **60**, 760 (1974).
[11] H. Klar, J.Phys. A**18**, 1561 (1985).
[12] J. Macek J. Phys. B**1**, 831 (1968).
[13] F. T. Smith, Phys. Rev. **120**, 1058 (1960).
[14] A. Kuppermann, Chem. Phys. Lett. **32**, 374 (1975).
[15] P. G. Hipe and A. Kuppermannan, Chem. Phys. Lett. **133**, 1 (1987).
[16] J. M. Launay and B. Lepetit, Chem. Phys. Lett. **144**, 346 (1988).
[17] J. Linderberg, S. Padjkaer, Y. Ohrn and B. Vessal, J. Chem. Phys. **90**, 6254 (1989).
[18] R. T. Pack and G. A. Parker, J. Chem. Phys. **87**, 3888 (1987).
[19] G.A. Parker and R.T. Pack, J. Chem. Phys. **98**, 6883 (1993).
[20] L. Wolniewicz, J. Hinze and A.Alijah, J. Chem. Phys. **99**, 2695 (1993).
[21] J. M. Launay and M. Le Dourneuf, Chem. Phys. Lett. **163**, 178 (1989).
[22] J. Z. H. Zhang and W.H. Miller, Chem. Phys. Lett. **153**, 465 (1988).

[23] J. C. Nieh and J. J. Valentini, Phys. Rev. Lett. **60**, 519 (1988).
[24] D. M. Neumark, A. M. Wodtke, G.N. Robinson, C. C. Hayden and Y.T. Lee, Phys. Rev. Lett. **53**, 226 (1984).
[25] J. M. Launay and S. Padjkaer, Chem. Phys. Lett. **181**, 95 (1991).
[26] B. Lepetit and J. M. Launay, J. Chem. Phys. **95**, 5159 (1991).
[27] J.D. Kress, R.B. Walker and E.F. Hayes, J. Chem. Phys. **93**, 8085 (1990).
[28] J. M. Launay, in Dynamical Processes in Moleculer Physics, edited by G. Delgado Barrio Institute of Physics Publishing (1993) p. 97-120
[29] A. Ohsaki and H. Nakamura, Phys. Rept. **187**, 1 (1990).
[30] A. Bastida, A. Requena and J. Zuniga, J. Phys. Chem. **97**, 5831 (1992).
[31] A.R. Cooper, S. Jain, and J. M. Hutson, J. Chem. Phys. **98**, 2160 (1992).
[32] J. J. Soares Neto, and J. Linderberg, J. Chem. Phys. **95**, 8022 (1991).
[33] F. Le Quere and C. Leforestier, J. Chem. Phys. **94**, 1118 (1991).
[34] L. M. Delves, Nucl. Phys. **9**, 391 (1959); ibid., **20**, 268 (1962).
[35] M. Danville and P. D. Kung, Can. J. Phys. **44**, 2095 (1966).
[36] R. H. Dalitz and G. Rajasekaran, Nucl. Phys. **50**, 450 (1964).
[37] A.A. Korsheninnikov, B.V. Danilin and M.V. Zhukov, Nucl. Phys. A**559**, 208 (1993).
[38] M.V. Zhukov, B.V. Danilin, D.V. Fedorov, J.M. Bang, I.J. Thompson, and J.S. Vaagen, Phys. Rept. **231**, 151 (1993).
[39] J. L. Ballot and M. Fabre de la Ripelle, Ann. Phys. **127**, 62 (1980).
[40] R. A. Adam and H. Fiedeldey, J. Phys. G**19**, 703 (1994)
[41] R. B. Clare and J. Levinger, Phys. Rev. C**31**, 2303 (1985).
[42] J. M. Richard, Phys. Rept. **212**, 1 (1992).
[43] M.I. Haysak, V.I. Lengyel, S. Chapupka and M. Salak, Czech. J. Phys. **41**, 799 (1991).
[44] A. Raspini, Inter. J. Theoret. Phys. **31**, 1407 (1992).
[45] H. Leeb, H. Fiedeldey, E.J.O. Gavin, S.A. Sofianos and R. Lipperheide, Few-body Systems, **12**, 55 (1992).
[46] R.N. Hill, J. Math. Phys. **18**, 2316 (1977).
[47] A. M. Frolov, Zh. Eksp. Teor. Fiz **92**, 1959 (1987) [Sov. Phys. -JETP **65**, 1100 (1987)].
[48] Z. Chen and C.D. Lin, Phys. Rev. **A42**, 18 (1990).
[49] D. R. Herrick, M. E. Kellman and R. D. Poliak, Phys. Rev. **A22**, 1517 (1980).
[50] M. E. Kellman and D. R. Herrick, Phys. Rev. **A22**, 1536 (1980).
[51] C. D. Lin, Phys. Rev. A**29**, 1019 (1984).
[52] Y.K. Ho and J. Callaway, Phys. Rev. A**27**, 1887 (1983).
[53] R.S. Berry and J.L. Krause, Adv. Chem. Phys. **70**, 35 (1988).
[54] R.D. Poshusta, J. Phys. **B18**, 1887 (1985).
[55] A. Martin, J.M. Richard and T.T. Wu, Phys. Rev. **A46**, 3697 (1922).
[56] D.M. Bishop and A.M. Frolov, J Phys. **B25**, 3049 (1992).
[57] A.M. Frolov, and A.J. Thakkar, Phys. Rev. **A46**, 4418 (1992).
[58] P. M. Morse and H. Feshbach, Methods of Theoretical Physics, MaGraw-Hill, New York, 1953. p. 1665.
[59] H. T. Coelho, J.J. De Groote, and J. E. Hornos, Phys. Rev. A**46**, 5443 (1992).
[60] A.A. Kvitsinsky, Few-Body Systems **10**, 73 (1991).
[61] J. Botero, Phys. Rev. A**35**, 36 (1987).
[62] J. Botero, Z. Phys. D**8**, 177 (1988).
[63] K. A. Jerjian and J. H. Macek, Phys. Rev. A**36**, 2667 (1987).
[64] C. D. Lin and X. H. Liu, Phys. Rev. A**37**, 2749 (1988).
[65] C. G. Bao, Y. P. Pan and X. H. Liu, Comput. Phys. Comm. **36**, 410 (1985).
[66] S. Watanabe and C. D. Lin, Phys. Rev. A**36**, 511 (1987).
[67] Z. Chen, C.G. Bao and C. D. Lin, J. Phys. B**25**, 61 (1992).
[68] M. Cavagnero, Phys. Rev. A**33**, 2877 (1986).
[69] C. W. Clark and C.H. Greene, Phys. Rev. A**21**, 1786 (1980).
[70] C. G. Bao and C. D. Lin, Few-body Systems, **16**, 47 (1994).
[71] C. Deng, R. Zhang and D. Feng, Int. J. Quant. Chem. **45**, 385 (1993).
[72] Ruiqin Zhang and Conghao Deng, Phys. Rev. A**47**, 71 (1993).
[73] G. Frey and B. J. Howard, Chem. Phys. **111**, 33 (1987).

[74] M. I. Haftel and V. B. Mandelzweig, Ann. Phys. (NY) **150**, 48 (1983).
[75] M. I. Haftel and V. B. Mandelzweig, Phys. Lett. A**120**, 232 (1987).
[76] see Bethe and Salpeter, Quantum Mechanics of one and two electron atoms, Springer-Verlag (Berlin), 1957. p. 150.
[77] D. E. Freund, B. D. Huxtable and J. D. Morgan, Phys. Rev. A**29**, 980 (1984).
[78] M. I. Haftel and V. B. Mandelzweig, Phys. Rev. A**38**, 5995 (1988).
[79] J. D. Morgan III and J. Baker, Bull. Am. Phys. Soc. **32**, 1245 (1987).
[80] C. D. Lin, Phys. Rev. A**10**, 1986 (1974).
[81] C. D. Lin, Phy. Rev. A**23**, 1585 (1981).
[82] T. Motoyama, N. Koyama and M. Matsuzawa, Phys. Rev. A**38**, 670 (1988).
[83] H. Fukuda, N. Koyama and M. Matsuzawa, J. Phys. B**20**, 2959 (1987).
[84] J. Z. Tang, S. Watanabe and M. Matsuzawa, Phys. Rev. A**46**, 2437 (1992).
[85] M. J. Seaton, J. Phys. B**7**, 1817 (1974)
[86] X.H. Liu, Z. Chen and C.D. Lin, Phys. Rev. **A44**, 5468 (1991).
[87] Igarashi and N. Toshima, Phys. Rev. A**50**, 232 (1994).
[88] C. H. Greene, Phys. Rev. A**23**, 661 (1981).
[89] H. R. Sadeghpour, J. Phys. B**25**, L29 (1992).
[90] M. Cavagnero, Z. Zhen and J. Macek, Phys. Rev. A**41**, 1225 (1990).
[91] K. Bathe, Finite Element Procedures in Engineering Analysis (Prentice-Hall, Englewood Cliffs, N. J. 1982).
[92] J. Shertzer and F.S. Levin, Phys. Rev. **A43**, 2531 (1991).
[93] Yan Zhou and C. D. Lin, J. Phys. B**27**, 5065 (1994).
[94] M.B. Kadomtsev and S.I. Vinitsky, J. Phys. B**20**, 5723 (1987).
[95] R. P. Madden and K. Codling, Phys. Rev. Lett. **10**, 516 (1963).
[96] C. D. Lin, Phys. Rev. A**12**, 4936 (1975).
[97] C. D. Lin, Phys. Rev. Lett. **35**, 1150 (1975).
[98] H. C. Bryant, et al., Phys. Rev. Lett. **38**, 228 (1977).
[99] D. R. Herrick and Sinanoglu, Phys. Rev. A**11**, 97 (1975).
[100] H.R. Sadeghpour, Phys. Rev. A**43**, 5821 (1991).
[101] P. G. Harris et al., Phys. Rev. A**42**, 6443 (1990).
[102] M. Domke et al., Phys. Rev. Lett. **66**, 1306 (1991).
[103] J. Z. Tang, Y. Wakabayashi, M. Matsuzawa, S. Watanabe and I. Shimamura, Phys. Rev. A49, 1021 (1994).
[104] C. L. Pekeris, Phys. Rev. **126**, 1470 (1962).
[105] C. Schwartz, Phys. Rev. **124**, 1468 (1961).
[106] P. G. Burke and H.M. Schey, Phys. Rev. **126**, 147 (1962).
[107] M. H. Day, Phys. Rev. A**26**, 1260 (1982).
[108] C. R. Liu and A. F. Starace, Phys. Rev. A**40**, 4926 (1989).
[109] J. W. Cooper, U. Fano and F. Prats, Phys. Rev. Lett. **10**, 518 (1963).
[110] C. D. Lin, Phys. Rev. A**14**, 30 (1976)
[111] M. Galiltis and R. Damburg, Proc. Phys. Soc. London **82**, 192 (1963).
[112] M. Halka, P.G. Harris, A.H. Mohagheghi, R.A. Reeder, C.Y. Tang, H.C. Bryant, J.B. Donahue, C.R. Quick, Phys. Rev. A**48**, 419 (1993).
[113] Bin Zhou and C. D. Lin, Phys. Rev. Lett. **69**, 3294 (1992).
[114] X. H. Liu, Z. Chen and C. D. Lin, Phys. Rev. A**44**, 5468 (1991).
[115] Yan Zhou, C. D. Lin and J. Shertzer, J. Phys. B**26**, 3937 (1993).
[116] Y. Accad, C. L. Pekeris and B. Schiff, Phys. Rev. A**11**, 1479 (1975).
[117] C. E. Moore, Atomic Energy Levels, Nat. Bur. Stand. No. 35 (U.S. GPO, Washington D. C. 1971) Vol. I.
[118] D. H. Oza, Phys. Rev. A**33**, 824 (1986).
[119] M. Domke, et al, Phys. Rev. Lett. **69**, 1171 (1991).
[120] J. Z. Tang, Ph.D. Thesis, The University of Electrocommunications, Tokyo, Japan, 1993.
[121] J. Z. Tang, S. Watanabe and M. Matsuzawa, Phys. Rev. A**48**, 841 (1993).
[122] H. D. Morgan and D. L. Ederer, Phys. Rev. A**29**, 1901 (1984).
[123] R. Moccia and P. Spizzo, Phys. Rev. A**43**, 2199 (1991).
[124] Y. K. Ho and J. Callaway, J. Phys. B**18**, 3481 (1985).

[125] P. R. Woodruf and J. Samson, Phys. Rev. A**25**, 848 (1982).
[126] M. Zubek, G. C. King, P. M. Rutter and F. Read, J. Phys. B**22**, 3411 (1989).
[127] B. Zhou, C. D. Lin, J. Z. Tang, S. Watanabe and M. Matsuzawa, J. Phys. B**26**, L337 (1993).
[128] J. Z. Tang, S. Watanabe, M. Matsuzawa and C. D. Lin, Phys. Rev. Lett. **69**, 1633 (1992).
[129] J.Z. Tang, C. D. Lin, Bin Zhou and I. Shimamura, Phys. Rev. A, to be published(1994).
[130] E.A.G. Armour and J.W. Humberston, Phys. Rept. **204**, 165 (1991).
[131] M.S.T. Watts and J.W. Humberston, J. Phys. B**25**, L491 (1992).
[132] K. Higgins and P.G. Burke, J. Phys. B**24**, L343 (1991).
[133] K. Higgins and P.G. Burke, J. Phys. B**26**, 4269 (1993).
[134] R.N. Hewitt, C.J. Noble and B.H.J. Bransden, Phys. B**25**, 2683 (1992).
[135] R.N. Hewitt, C.J. Noble and B.H. Bransden, J. Phys. B**26**, 3661 (1993).
[136] N.K. Sarkar, M. Basu and A.S. Ghosh, J. Phys. B**26**, L799 (1993).
[137] J. Mitroy, J. Phys. B**26**, 4861 (1993).
[138] B. J. Archer, G. A. Parker and R. T. Pack, Phys. Rev. A**41**, 1303 (1990).
[139] C.J. Brown, and J.W. Humberston, J. Phys. B**18**, L401 (1985).
[140] J.R. Winick and W.P. Reinhardt, Phys. Rev. A**18**, 925 (1978).
[141] A. K. Bhatia and R. J. Drahman, Phys. Rev. A**42**, 5117 (1990).
[142] T. T. Gien and G. G. Liu, J. Phys. B**27**, L179 (1994).
[143] J. S. Cohen, in Review of Fundamental Processes and Applications of Atoms and Ions, ed. C. D. Lin, World Scientific (Singapore, 1993).
[144] L.I. Ponomarev, Contemp. Phys. **31**, 219 (1990).
[145] J. D. Jackson, Phys. Rev. A**49**, 132 (1994).
[146] I. V. Puzynin and S. I. Vinitsky, Muon. Catal. Fusion **3**, 307 (1988).
[147] X. H. Liu, Private communication (1994).
[148] V. V. Gusev, V. I. Puzynin, V. V. Kostrykin, A. A. Kvitsinsky, S. P. Merkuriev and L. I. Ponomarev, Few-Body Systems **9**, 137 (1990).
[149] S. Hara and T. Ishihara, Phys. Rev. A**40**, 4232 (1989).
[150] C. Y. Hu and A. K. Bhatia, Phys. Rev. A**43**, 1229 (1991).
[151] I. Shimamura, Phys. Rev. A**40**, 4863 (1989).
[152] Y. Zhou and C. D. Lin (unpublished).
[153] N. Fukuda, T. Ishihara and S. Hara, Phys. Rev. A**41**, 145 (1990).
[154] M. Kimamura, Muon Catal. Fusion **3**, 335 (1988).
[155] J. S. Cohen aand M. C. Struensee, Phys. Rev. A**43**, 3460 (1991).
[156] T. Matsuzaki, Muon Catal. Fusion **2**, 217 (1988).
[157] S. Hara and T. Ishihara, Phys. Rev. A**39**, 5633 (1989).
[158] Y. Kino and M. Kamimura, Hyperfine Interactions, **82** 45, 195 (1993).
[159] I. Ben-Itzhak, Z. Chen, B. D. Esry, I. Gertner, O. Heber, C. D. Lin and B. Rosner, Phys. Rev. A**49**, 1774 (1994).
[160] B. Zhou and C. D. Lin, Phys. Rev. A (submitted, 1994)
[161] J. H. Xi, C. G. Bao and C. D. Lin (unpublished).
[162] I.V. Puzynin and S.I. Vinitsky, Muon Catal. Fusion 3 (1988) 307.